NUMERICAL MODELING OF TWO-PHASE FLOW IN THE SODIUM CHLORIDE-WATER SYSTEM WITH APPLICATIONS TO SEAFLOOR HYDROTHERMAL SYSTEMS

A Thesis
Presented to
The Academic Faculty

By

Kayla C. Lewis

In Partial Fulfillment
Of the Requirements for the Degree
Doctor of Philosophy in Earth and Atmospheric Sciences

Georgia Institute of Technology

December, 2007

NUMERICAL MODELING OF TWO-PHASE FLOW IN THE SODIUM CHLORIDE-WATER SYSTEM WITH APPLICATIONS TO SEAFLOOR HYDROTHERMAL SYSTEMS

Approved by:

Dr. Robert P. Lowell
School of Earth and Atmospheric Sciences
Georgia Institute of Technology

Dr. Andrew V. Newman
School of Earth and Atmospheric Sciences
Georgia Institute of Technology

Dr. Leonid Germanovich
School of Civil Engineering
Georgia Institute of Technology

Dr. Bruce A. Buffet
Department of the Geophysical Sciences
University of Chicago

Dr. Martial Taillefert
School of Earth and Atmospheric Sciences
Georgia Institute of Technology

Date Approved: November 7, 2007

DEDICATION

This work is dedicated to my parents, Lynda and Bill, and to Iggy.

ACKNOWLEDGEMENTS

Funding for this work was provided by the National Science Foundation, grant OCE-0351942 (to Robert P. Lowell). I would like to thank my thesis advisor, Bob Lowell, for his support and insights throughout this project; additionally, the equations of state for FISHES could not have been assembled without the help of Thomas Driesner, Andre Anderko, and Donald Archer.

TABLE OF CONTENTS

LIST OF FIGURES

LIST OF SYMBOLS

T	Temperature
P	Pressure
X	Salinity
ρ	Density
g	Gravitational Acceleration
a	Thermal Diffusivity
A	Dike Half Width
k	Rock Permeability
k_r	Relative Permeability
S	Volumetric Saturation
μ	Dynamic Viscosity
ϕ	Porosity
v	Velocity
h	Specific Enthalpy
c	Specific Heat
λ	Thermal Conductivity
D	Salt Chemical Diffusivity
R	Relaxation Factor

SUMMARY

In order to explain the observed time-dependent salinity variations in seafloor hydrothermal vent fluids, quasi-numerical and fully numerical fluid flow models of the NaCl-H_2O system are constructed. For the quasi-numerical model, a simplified treatment of phase separation of seawater near an igneous dike is employed to obtain rough estimates of the thickness and duration of the two-phase zone, the amount of brine formed, and its distribution in the subsurface. Under the assumption that heat transfer occurs mainly by thermal conduction it is shown that, for a two-meter wide dike, the maximum width of the two phase zone is approximately 20 cm and that a zone of halite is deposited near the dike wall. The two-phase zone is mainly filled with vapor. After 13 days, the two-phase zone begins to disappear at the base of the system, and disappears completely by 16 days. The results of this simplified model agree reasonably well with transient numerical solutions for the analogous two-phase flow in a pure water system. The seafloor values of vapor salinity given by the model are compared with vapor salinity data from the "A" vent at 9-10°N on the East Pacific Rise and it is argued that either non-equilibrium thermodynamic behavior or near-surface mixing of brine with vapor in the two-phase region may explain the discrepancies between model predictions and data. For the fully numerical model, the equations governing fluid flow, the thermodynamic relations between various quantities employed, and the coupling of these elements together in a time marching scheme is discussed. The thermodynamic relations are expressed in terms of equations of state, and the latter are shown to vary both smoothly and physically in *P-T-X* space. In particular, vapor salinity values near the vapor-liquid-

halite coexistence surface are shown to be in strong agreement with recently measured values. The fully numerical model is benchmarked against previously published heat pipe and Elder problem simulation results, and is shown to be largely in agreement with those results. Additionally, code output from an approximately one-dimensional scenario is compared to the analytic solution of the classical one-dimensional thermal advection-diffusion equation, and it is found that the numerical output and analytic solution are in strong agreement. A number of simulation results are presented in the context of two-phase flow and phase separation within the framework of the single pass model, a model that has been shown to be useful in the study of seafloor hydrothermal systems. It is found that a quasi-stable two-phase (liquid + vapor) zone at depth below the hydrothermal discharge outlet gives rise to vent fluid with lower than normal seawater salinity. Additionally, it is shown that increasing the spatial extent of the two-phase zone can lower vent fluid salinity, even with the average temperature of the two-phase zone held constant. As the two-phase zone evolves, brine of high salinity and density collects at the bottom of the system and is held there primarily via the effect of vapor on the liquid phase's relative permeability; however, it is found that lowering the temperature of the heat source until the two-phase zone vanishes and allowing the system to evolve for some time results in the flushing of this brine from the system. The resulting pattern of vent fluid salinities resembles that described in a widely held conceptual model of vent fluid salinity variation in seafloor hydrothermal systems, where low salinity fluids emerge from venting systems during early stages, and high salinity fluids emerge at later stages as brine is flushed from the system. The effect of varying the permeability is investigated, and it is found that peaks in vent fluid salinities occur later in time for lower

permeabilities than one might expect for a simple linear relationship. Finally, it is argued that the numerical approach used in this thesis may be able to explain the vent fluid salinities and temperatures found at the Main Endeavour Vent Field on the Juan de Fuca Ridge, as this approach is able to produce simulated vent fluid salinities that match observed values from the Endeavour Field vents Dante and Hulk.

CHAPTER 1: INTRODUCTION

Seafloor hydrothermal systems are vital components of a vast heat engine, delivering thermal energy from the Earth's upper mantle to the surface of the oceanic lithosphere. These systems are responsible for 25% of Earth's total heat flux, and about 33% of the total oceanic heat flux, figuring crucially in determinations of the planet's overall heat budget [e.g., Williams and Von Herzen, 1974; Sclater et al., 1980; Pollack et al., 1993; Stein and Stein, 1994]. In addition to transporting heat, these systems play an important role in the exchange of chemical species between seawater and the ocean floor [Wolery and Sleep, 1976; Edmond et al., 1979; Thompson, 1983; Elderfield and Schultz, 1996]. Products of these chemical exchanges serve as the principal energy source for chemoautotrophic bacteria and their attendant invertebrate biological communities [e.g., Jannasch and Wirsen, 1979; Jannasch, 1983; Shank et al., 1998]. The existence of such ecological systems was unexpected, and led to a flurry of biological research [Van Dover, 2000], leading some biologists to explore the possible role of hydrothermal systems in the origin of life on Earth [e.g., Baross and Hoffman, 1985; Miller et al., 1995; Imai et al., 1999]. In addition to being valuable subjects of study in their own right, it is clear that seafloor hydrothermal systems are central to the solutions of important problems in geophysics, geochemistry, and biology.

Modelers of seafloor hydrothermal systems face a number of interpenetrating and challenging problems. First, although it is known that subsurface magma provides the heat source for high temperature venting systems, the detailed linkages between magma chamber structure and hydrothermal heat redistribution processes remain largely

unknown [Sinha and Evans, 2004]. Second, it is known that magmatic and tectonic events can heavily influence the character of hydrothermal venting [Von Damm, 2004], yet again the quantitative linkages between these processes are not well understood. Third, hydrothermal circulation involves strong couplings between fluid flow, geochemical, and biological processes, and modeling approaches have not yet reached levels of sophistication adequate to take these features fully into account. Fourth, high-temperature and diffuse flow venting often occur simultaneously and near one another [Delaney et al., 1992; Schultz et al., 1992; Rona and Trivett, 1992; Von Damm and Lilley, 2004], but how these flows are related remains unclear [Lowell et al., 2003]. Finally, even though sub-seafloor fluid pressures are high enough to dramatically raise the boiling point of water, high temperature venting systems nevertheless reach temperatures in excess of the boiling point, leading to the phenomena of phase separation and two-phase flow; these in turn have profound effects on hydrothermal circulation, overall fluid chemistry, and particularly the salinity of venting fluids. Two-phase flow, phase separation, and their effects on the evolution of hydrothermal circulation and vent fluid salinity are the subjects of this thesis.

1.1 The Evolution of Vent Fluid Salinity

The salinities of hydrothermal vent fluids are generally different from that of ordinary seawater and exhibit wide spatial variability; some vent fluid salinities are temporally stable, but others exhibit wide temporal variability as well. At 21°N EPR and at the TAG and MARK sites on the Mid-Atlantic Ridge (MAR), vent fluid salinities have been stable over the course of several years [Campbell et al., 1988; Edmond et al., 1995]. On the Juan de Fuca Ridge (JDF), the Monolith vent fluids have had high but declining

salinities over a number of years [Butterfield and Massoth, 1994]. At the Main Endeavour field, also on the JDF, vent fluid salinities vary from north to south, and the fluid salinities were disturbed following an earthquake in 1999 [Lilley et al., 2003]. The venting sites at 9-10°N on the EPR underwent dramatic changes following a magmatic eruption in 1991 [Haymon et al., 1993]. For example, the salinity at 'F' vent was well below that of seawater, but within a few years after the eruption, it rose to well above seawater salinity [Von Damm et al., 1997]. Nearby, the salinity at 'A' vent rose significantly from 1991 to 1994, although the salinity remained well below that of seawater (Von Damm et al. 1995). Figure 2 summarizes the current vent salinity data. Although some of the salinity variability may be explained by the precipitation of a Cl-bearing mineral [Seyfried et al., 1986], it is widely acknowledged that the primary cause is the subsurface boiling of seawater [e.g., Berndt and Seyfried, 1990; Von Damm et al., 1997, 2002; Von Damm, 2004]. Before a mechanism relating the boiling of seawater and vent fluid salinity variations can be meaningfully described, it will first be necessary to consider the thermodynamic phase space behavior of seawater.

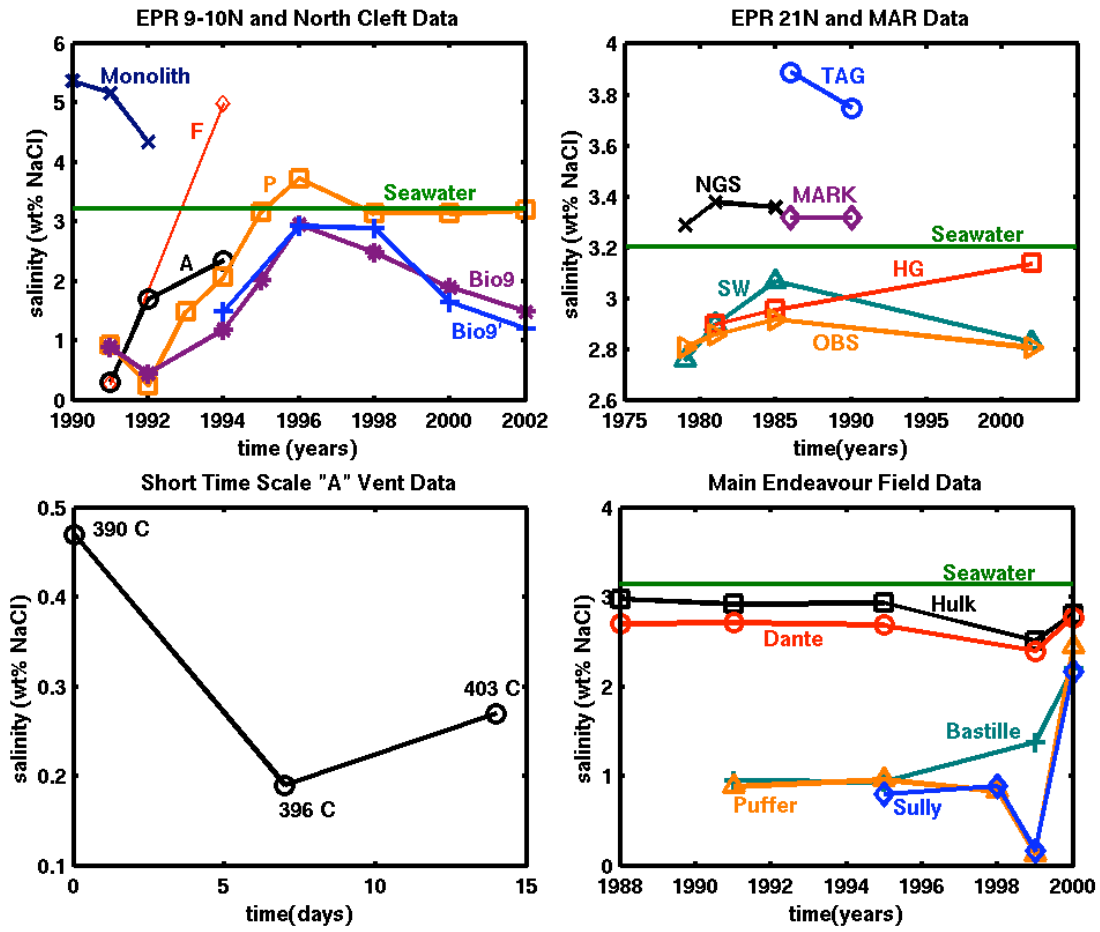

Figure 1 Summary of the current vent fluid salinity data. In the upper left panel, Monolith is a North Cleft site on the JDF; the others are from EPR 9-10°N. In the upper right panel, TAG and MARK refer to MAR sites; the others refer to EPR at 21°N. The lower left panel is a 2-week time series of the vent salinity and temperature at "A" vent at 9°N EPR, taken in 1991 immediately after a magmatic eruption. The lower right panel shows sites from the Main Endeavour Vent Field, JDF. Data prior to 1995 are taken from Von Damm [1995]. More recent data from 9°N are from Von Damm [2004] and those from 21°N EPR are from Von Damm et al. [2002]. More recent data from Main Endeavour are from Lilley et al. [2003].

1.2 The Phase Space Regions of the NaCl-H_2O System

Thermodynamically, seawater can be treated accurately as equivalent to a 3.2 wt% NaCl-H_2O solution [Bischoff and Rosenbauer, 1984][1]. It is for this reason that current equations of state treat seawater as such; also, for the purposes of this thesis, it will be

[1] Hence, seawater with a chlorinity of 540 mmol/kg molal is equivalent to NaCl-H_2O of 3.2 wt% NaCl. In general, seawater chlorinity and equivalent solution salinity may be related via a simple constant of proportionality, i.e., $X = CM$ where $[X]$ is wt% NaCl, $[M]$ is mmol/kg, and $C = 0.0059$.

sufficient to consider the thermodynamic properties of the NaCl-H_2O system. Figure 2 shows the temperature-pressure-salinity (*T*-*P*-*X*) phase diagram, adapted from Bischoff and Pitzer [1989]. The salinity is plotted on a log scale, so $X = -\infty$ represents 0 wt% NaCl. At the zero salt end of the figure is the boiling curve for pure water, terminating at the pure water critical point, labeled CP(H_2O). As salt is added to the system, the critical point of pure water becomes part of a critical curve, so that there is a different critical point for each temperature. Also, the boiling curve for pure water becomes part of a surface, with a two-phase mixture of vapor and liquid beneath it and either pure liquid, pure vapor, or supercritical fluid above it, depending on the bulk salinity *X*. Figure 3 shows a schematic isothermal slice from the *P*-*T*-*X* space. The surface just described bounds the two-phase region from above, and a surface along which liquid, vapor, and halite co-exist bounds the two-phase region from below. This lower surface has a constant pressure for any fixed temperature, and it will be referred to as the 3-phase surface. Below the 3-phase surface there is a surface representing salt-saturated vapor. To the left of this surface is the pure vapor phase while to the right is a mixture of vapor and solid halite. This surface, being a function of both temperature and pressure, will be referred to as the salt-saturated vapor surface. Considering the above phase space relationships, a mechanism relating subsurface boiling of seawater and salinity variation can now be described.

By the Inverse Lever Rule, if fluid of a given bulk salinity is in the two-phase region, then the salinities of the liquid and vapor phases can be obtained by extending a horizontal (constant *P* and *T*) line from the fluid's phase space coordinates to the boundaries of the two-phase region. The salinities at the intersections of this line with the

boundaries give the liquid (high salinity intersection) and vapor (low salinity intersection) phase salinities. Hence, there is a differential partitioning of salt between the liquid and vapor phases in this region, leading to the co-existence of a low salinity vapor and high salinity brine, relative to the bulk salinity. The brine has a density higher than the bulk density, and thus tends to sink relative the surrounding rock matrix; similarly, the vapor is more buoyant and tends to rise. This process is described as phase separation, and the mixing of seawater with the products of this process supply a mechanism relating subsurface boiling to surface vent fluid salinity variations.

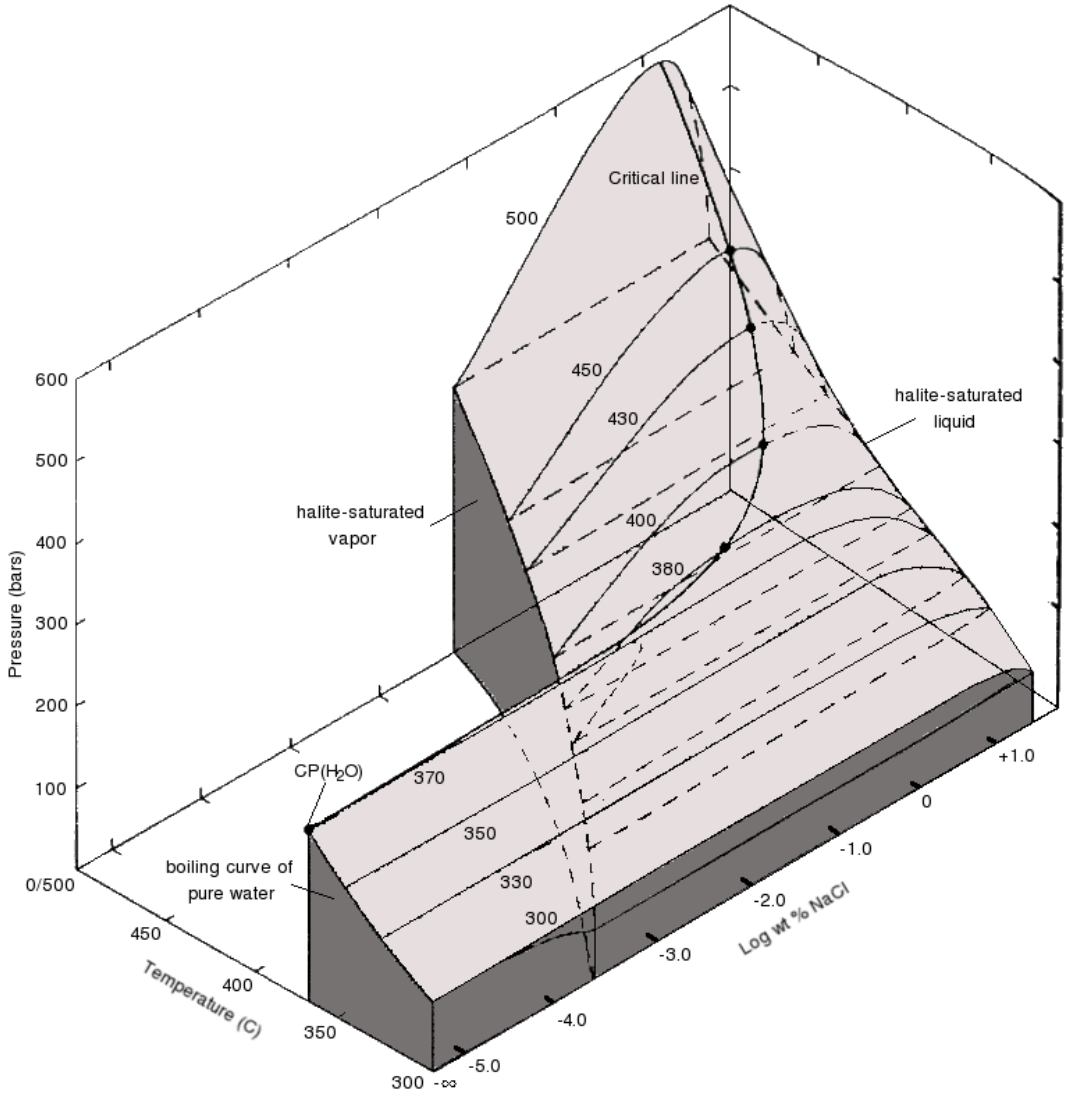

Figure 2 Pressure-temperature-salinity (*P-T-X*) diagram for the NaCl-H_2O system, adapted from Bischoff and Pitzer [1989].

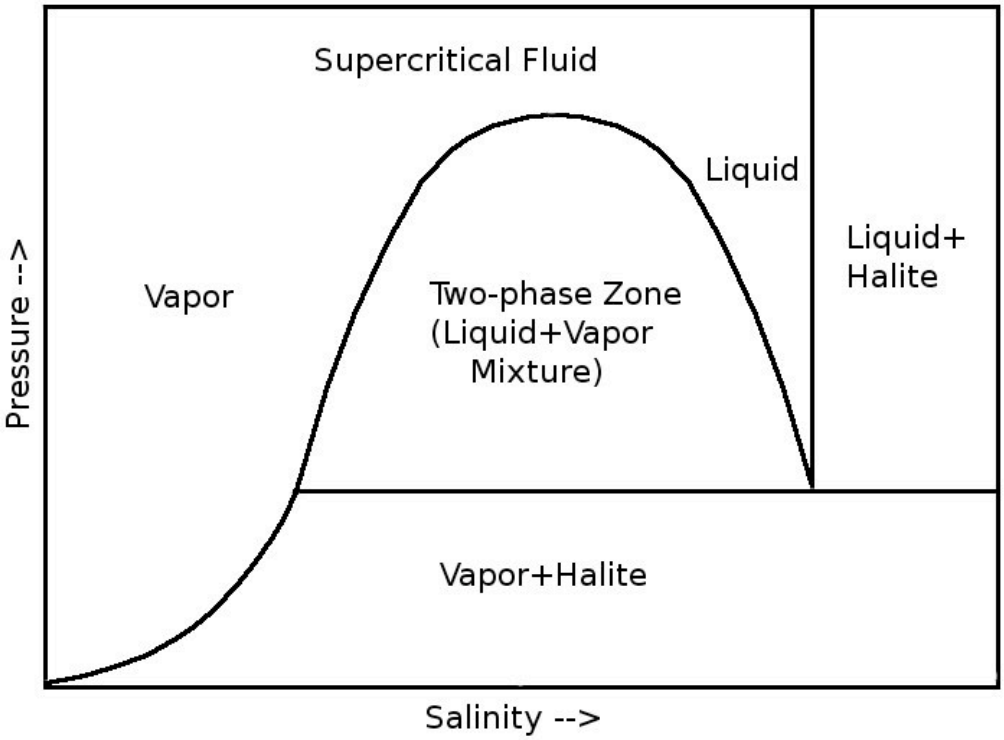

Figure 3 Schematic representation of a constant temperature slice from the *P-T-X* diagram of the NaCl-H_2O system.

1.3 Objectives and Significance of the Thesis

For the specification of the mechanism relating subsurface boiling of seawater to vent fluid salinity variations to be complete, it is necessary to show, firstly, that there exist solutions involving this mechanism and which satisfy the mass, energy, and momentum equations describing seafloor hydrothermal systems, and secondly, that the system geometry, initial, and boundary conditions are at least not unlikely to occur in actual venting systems. In order to complete the specification of a mechanism relating

subsurface boiling to vent fluid salinity variations, and explain the observed time-dependent salinity variations in seafloor hydrothermal vent fluids, quasi-numerical and fully numerical fluid flow models of the NaCl-H_2O system will be constructed. The fully numerical model will be benchmarked, and a number of simulation results will be presented in the context of two-phase flow and phase separation, culminating in simulations that produce temporal variations in vent fluid salinity that are similar to those observed. The model predictions will also be shown to be consistent with a conceptual model of how vent salinity should respond to changing subsurface conditions.

CHAPTER 2: PREVIOUS MODELING APPROACHES

Hydrothermal processes involve mass, heat, and solute transport in a fluid saturated porous medium. Transport occurs by both convective and diffusive processes, and in many cases, multi-phase flow and phase separation take place. If the fluid is considered to be an NaCl-H_2O solution, which is commonly the case, precipitation of halite may occur. Typically, however, only the effect of halite formation on the rock permeability is incorporated into numerical algorithms such as employed from Chapter 4 onward in this thesis. Then only transport by vapor and brine phases need be considered. Only somewhat recently have studies begun to consider fluid flows in which differential partitioning of salt as well as heat between liquid and vapor phases occurs. Many of these studies originated in efforts to understand processes in terrestrial hydrothermal systems, which often contain saline fluids [Helgeson, 1968; Mercado, 1969; Roedder, 1979; Fournier, 1987] and thus, like their oceanic counterparts, involve multiphase flow of a binary mixture. Considerable effort has been directed toward two somewhat simpler problems, however. These include studies of double and cross-diffusive convection in the case of salt transport in a single-phase liquid, and studies involving liquid and vapor phases of single component fluids (pure water) in the case of two-phase flow.

2.1 Salt Transport in Single-Phase Liquid

Studies of salt transport in fluid-saturated porous media can be usefully divided into two categories, both of which involve fluid flow in horizontal or vertical slabs: studies of double-diffusive convection, where imposed solutal and thermal boundary conditions induce fluid flow; and studies of cross-diffusive (also called Soret-induced) convection,

where temperature gradients imposed upon an initially uniform salinity distribution give rise to concentration gradients. Due to the rich literature in the field of diffusive convection in a porous medium, what follows is merely a sampling of available work.

In an early study, Nield [1968] used linear stability analysis to investigate the onset of convective instability in a horizontal slab with initial vertical solutal and temperature gradients and various boundary conditions. He found that a strongly stabilizing solute gradient opposed by a destabilizing thermal gradient can give rise to an oscillatory instability, and that, for generalized boundary conditions, as long as the thermal and solute boundary conditions have equivalent forms, the net destabilizing effect is given by the sum of the thermal and solute Rayleigh numbers. Lombardo et al. [2001] provide an example of non-linear stability analysis applied to this kind of system. Recently, Bahloul et al. [2003] compared double- and cross-diffusive convection by employing linear and non-linear stability analyses and numerical methods to study the stability regime of fluid in a horizontal porous slab, with imposed temperature and salt fluxes on the top and bottom boundaries. It was found, among other things, that when the Lewis number (the ratio of thermal to salt diffusivity) is greater than unity, the results are independent of the type of convection considered. A variety of issues have been studied in relation to double-diffusive convection. For example, Mahidjiba et al. [2000] examined the above horizontal slab scenario except with mixed boundary conditions; whereas Kalla et al. [2001] studied the effect of a weak temperature gradient imposed by side heating on double-diffusive convection in a horizontal slab. As an example of a study involving a vertical slab, Schoofs et al. [2000] studied vertically stacked convective layers formed by imposing a temperature gradient upon a low porosity column filled with fluid assumed to

be initially stably stratified with respect to solute. Sezai and Mohamad [1999] conducted a numerical study on double-diffusive convection in a three-dimensional cube with Dirichlet conditions on two vertical sidewalls. Nield and Bejan [2006] provide a fairly full review of work on double-diffusive convection in a porous medium.

Linear and non-linear stability analysis has also been applied to cross-diffusive convection in a horizontal slab. For example, Patil and Rudraiah [1980] and Brand and Steinberg [1983a] perform linear analyses and Brand and Steinberg [1983b] discuss non-linear aspects of the problem. Bahloul et al. [2007] provide a more thorough review of cross-diffusive convection, as well as considering the effects of cross-heating on the horizontal layer.

Quantities in the NaCl-H_2O system typically vary nonlinearly over orders of magnitude in systems of practical interest. This nonlinear variation precludes the general validity of some commonly employed assumptions in the double- and cross-diffusive convection literature reviewed above, such as that density variations can be represented by the linear form

$$\rho = \rho_0[1 - \alpha(T - T_0) - \alpha'(X - X_0)] \tag{2.1}$$

where the subscripted values ρ_0, T_0, and X_0 represent reference values of density, temperature, and salinity, respectively. In analyses where the temperature and salinity do not vary much, and where the density does not strongly depend on the pressure (which is usually the case), such an assumption is appropriate; thus, the use of (2.1) in the linear stability analyses of double- and cross-diffusive convection is largely appropriate. However, in actual hydrothermal systems, terrestrial or oceanic, this assumption is highly inappropriate, as the temperature and salinity may vary over orders of magnitude.

Another assumption that may not be appropriate for these systems is the Boussinesq approximation, which is that the density may be treated as a constant in the equations describing fluid flow, except in the buoyancy terms (that is, terms containing the gravitational acceleration g). When the density varies widely and is additionally a nonlinear function of the temperature and salinity (which is the case in many scenarios of interest), it is at best unclear whether density variations in the inertial terms can be safely neglected.

2.2 Two-Phase Flow in Pure Water Systems

The field of two-phase flow of a single component fluid as applied to geothermal systems is too large of a field to be comprehensively reviewed here; however, a representative sample of work in the field is presented here. Of considerable importance is the pioneering work of Faust and Mercer [1979a,b,c], who developed the fundamental equations describing transport of heat and mass in a porous medium as well as the first numerical approaches to implement these equations. The numerical scheme presented in Chapter 4 employs the equations of Faust and Mercer [1979a]. Also of considerable importance is the work of K. Pruess, who initiated [Pruess, 1987, 1991] and contributed extensively to the development of [e.g. Pruess et al., 1999; Xu and Pruess, 2001; Pruess and Battistelli, 2002] the widely used TOUGH family of geothermal reservoir simulators. A recent version of TOUGH has been updated to include the effects of NaCl (see below and section 4.1). For a review of the TOUGH codes, see Pruess [2004].

Some of the earliest studies of two-phase flow in a single-component fluid considered the circulation of boiling water adjacent to a vertical heated dike injected into a permeable medium. By assuming that the vapor layer along the dike is thin and that the

vapor phase is much more buoyant than the liquid phase, Parmentier [1978] was able to show that the steady state width of the vapor layer is proportional to $y^{1/2}$, where y is the distance from the bottom of the dike. Cheng and Verma [1981] considered a similar scenario, and studied the effects of changing the relative temperatures of the dike and the surrounding fluid. They found, for instance, that increasing the sub-cooling of the surrounding fluid tends to decrease the steady-state thickness of the vapor layer, and increase the steady-state thermal boundary layer width of the liquid phase. Cheng and Pop [1984] studied the transient aspects of the above problem and found that at early times, heat is transferred as if by one-dimensional heat conduction, while at later times two-dimensional convective heating dominates.

In addition to flow adjacent to a dike, there has been modeling work on one-dimensional heat pipes. Straus and Schubert [1981] modeled vapor-dominated terrestrial hydrothermal systems, such as the northern California geysers or those of Kawah Kamojang in West Java, as one-dimensional heat pipes, and determined the ratios of mass flow rate and permeability to thermal conductivity required to accurately model these systems. Kissling et al. [1992a] consider the one-dimensional flow of liquid and vapor through a horizontal porous slab, and study the affect of changes to the boundary conditions of a system with an initially steady flow pattern. Kissling et al. [1992b] study two-phase flow of a single-component fluid in a vertical slab. It is demonstrated that the sign of the wave speed determines the direction of information flow, and not the flow direction of the liquid or vapor phase. McGuinness et al. [1993] discuss the conditions under which vapor-dominated and liquid-dominated heat pipe solutions will obtain numerically as well as in actual systems depending on the boundary conditions. In

McGuinness [1996], this numerical approach is extended to account for capillarity effects, and heat pipe scenarios dominated by conduction are studied in McGuinness [1997]. Young [1996] delineates the necessary conditions for the existence of a stable phase transition in a geothermal heat pipe, and applies this analysis to several field examples. Xu and Lowell [1998a], employing linear stability analysis and numerical methods, argue that discontinuities in permeability or thermal conductivity may give rise to oscillatory instabilities in heat pipes.

Finally, there are a number of models of two-phase flow in natural hydrothermal systems. For example, Ingebritsen and Sorey [1985] describe and numerically apply a conceptual model of the Lassen Volcanic National Park geothermal system. In this model, a reservoir of high enthalpy two-phase fluid feeds vapor and high salinity liquid flows at high and low altitudes, respectively. Using numerical methods, they were able to determine many necessary conditions for the formation and stability of such a system, such as the existence of low-permeability barriers that prevent movement of cool liquid into the vapor zone. Xu and Lowell [1998b] extend the work of Ingebritsen and Sorey [1985] to include a recharge channel and a recirculation region beneath the liquid discharge channel. Additionally, they explicitly account for the system's magmatic heat source by specifying heat fluxes at the base of the system. Numerical simulations were able to reproduce observed mass and energy discharge rates from the system. They find that the vapor-dominated zone is characterized by an oscillatory instability of the kind discussed in Xu and Lowell [1998a]. Hayba and Ingebritsen [1997] use the code HYDROTHERM [Hayba and Ingebritsen, 1994] to investigate ground water flow near cooling plutons. Among many interesting findings, they showed that system temperatures

and life spans decrease with increasing permeability, and that, in the absence of a low-permeability caprock, topographically driven groundwater flow can significantly alter the character of hydrothermal circulation at depth.

As the above studies are based on pure water models (in the case of the two-phase studies) or on single-phase fluids (in the case of double- and cross-diffusive convection), they may be usefully viewed as analog cases for more complicated scenarios, but they are of little direct relevance to modeling realistic seafloor systems; however, some recent studies have, to varying extents, included the effects of salt on multiphase systems. Lowell and Xu [2000] used the numerical code GTHM to investigate the circulation of hydrothermal seawater adjacent to an igneous dike. Although GTHM was a pure water code, by assuming a seawater critical point, they were able to show that the width and duration of the two-phase zone adjacent to the dike are negatively correlated to the permeability, and positively correlated to the dike width. Furthermore, they were able to show that mean heat flux increases with permeability, but is independent of the dike width. McGuinness et al. [1995] model the Kakkonda geothermal reservoir using the MULKOM simulator extended to include the transport of salt, though not its thermodynamic effects. It was shown that salt transfer occurs primarily through a fissure system, while heat is transferred as if through a homogenous porous medium. Bai et al. [2003] used the code GTHSW to model one-dimensional NaCl-H_2O heat pipes and explored the effects on their behavior of modifying the basal heat flux and permeability. It was found that brine forms at the base of such systems as they evolve; additionally, that unlike their pure water counterparts, salt water heat pipes often do not achieve steady state. Unfortunately, one-dimensional heat pipe simulations are not particularly relevant

to seafloor hydrothermal systems. Actual systems are probably at least two-dimensional and there is usually no adequate reason for supposing that the total mass flux out of such systems is fixed at zero. Salt water heat pipe solutions may be useful for understanding a continental system such as the Salton Sea in California [Bai et al., 2003] and can be used to benchmark numerical algorithms (see section 5.1), however. Lewis and Lowell [2004] studied two-phase flow of seawater adjacent to an igneous dike, and were able to provide rough estimates of the width and duration of the two-phase zone. Chapter 2 describes this work in detail.

Finally, there has been recent work on two-phase flow in a saline fluid based on numerical schemes that simultaneously account for the thermodynamics of salt water and address more geologically realistic scenarios than those found in heat pipe simulations. Kissling [2005a,b] introduces the code NaCl-TOUGH2, which includes thermodynamic equations of state for the NaCl-H_2O system (although see section 4.1), and applies it to a number of examples, such as the counter-flow of two brine phases in a vertical column, and the geologically interesting case of fluid flow in the Taupo Volcanic Zone in New Zealand. Geiger et al. [2005] use a finite element-finite volume numerical solution technique, which is introduced with benchmarking and examples in Geiger et al. [2004; 2006a,b] (again, see section 4.1), to study fluid convection in the Earth's crust. To this end, they run simulations of fluid flow in an open top 4 x 4 km square box at geologically realistic *P-T-X* values, for a range of permeabilities and hydrostatic pressure conditions. Categorizing their results into five different flow patterns, they conclude that quantities such as the Rayleigh number and buoyancy ratio cannot be applied to the system as a whole to characterize the behavior of the convective patterns that ensue.

The work reviewed in this chapter illustrates the fact that numerical methods employing realistic equations of state are essential for the study of a great many systems of geophysical interest. To that end such a method, FISHES, is presented and applied starting in Chapter 4. However, before presenting and applying this method, and partly as a first step toward conceptualizing the issues at stake, a quasi-numerical approach will be presented, applied, and discussed in the following chapter.

CHAPTER 3: A QUASI-NUMERICAL APPROACH TO PHASE SEPARATION[2]

As a first step toward understanding phase separation and the evolution of salinity at hydrothermal vents, a simplified quasi-numerical model will be constructed. In this model it is assumed that heat transfer occurs by thermal conduction across the vertical walls of a cooling dike. This problem was chosen because (a) dike injection is the fundamental mode of formation of new oceanic crust, (b) hydrothermal circulation near a dike is relatively short-lived and thus allows one to understand transient aspects of phase separation flow, and (c) the modeling results can be compared with the limited data available from "A" vent (Figure 1, lower left panel). The thermal conduction solution allows one to estimate the thicknesses of the halite and two-phase zones and the duration of two-phase flow. Moreover, by assuming thermodynamic equilibrium and coupling of these analytical thermal solutions with tabulated properties such as vapor and brine salinity and density as functions of pressure and temperature [Bischoff, 1991], one can construct scenarios for the evolution of vent salinity that result from phase separation near the dike wall.

In the following sections of this chapter, the basic model and its implications will be outlined; then the results of the model will be compared with numerical results for a pure water system, and the limitations of the model that result from the mathematical simplifications made here will be discussed. Then the model is applied to the vent salinity data at "A" vent shown in Figure 1. It will be shown that the salinity data at "A" vent does not correspond to an equilibrium vapor salinity generated by the model, and the conclusion is reached that either non-equilibrium thermodynamic processes or near-

[2] The material from this chapter is essentially the same as from Lewis and Lowell [2004].

surface mixing of brine and vapor in the two-phase zone explain this discrepancy. Finally, there will be a section containing qualitative speculation on the causes of short- and long-term variations in salinity that occurs at seafloor hydrothermal vents as shown in Figure 1.

3.1 The Mathematical Model

The geometry of the model (Figure 4) consists of a fluid-saturated porous slab of height h and infinite width, initially at temperature $T = 0^{\circ}C$, into which an impermeable dike of height h, width $2A$, and temperature $T = T_0$ is instantaneously emplaced. The top boundary $z = 0$ represents the seafloor, which is maintained at constant pressure $P = 250$ bars. Although the seafloor boundary is nominally maintained at $T = 0^{\circ}C$, it is recognized that ascending buoyancy-driven fluid flow near the dike will result in high-temperature fluid venting. For simplicity this venting is approximated by assuming the conductive solution near the dike is maintained at the upper boundary $z = 0$. The implications of this assumption are discussed in section 3.3. It is further assumed that the porosity of the medium is less than 10%, so that most of the thermal energy is in the rock matrix and that local thermal equilibrium exists between the rock and fluid.

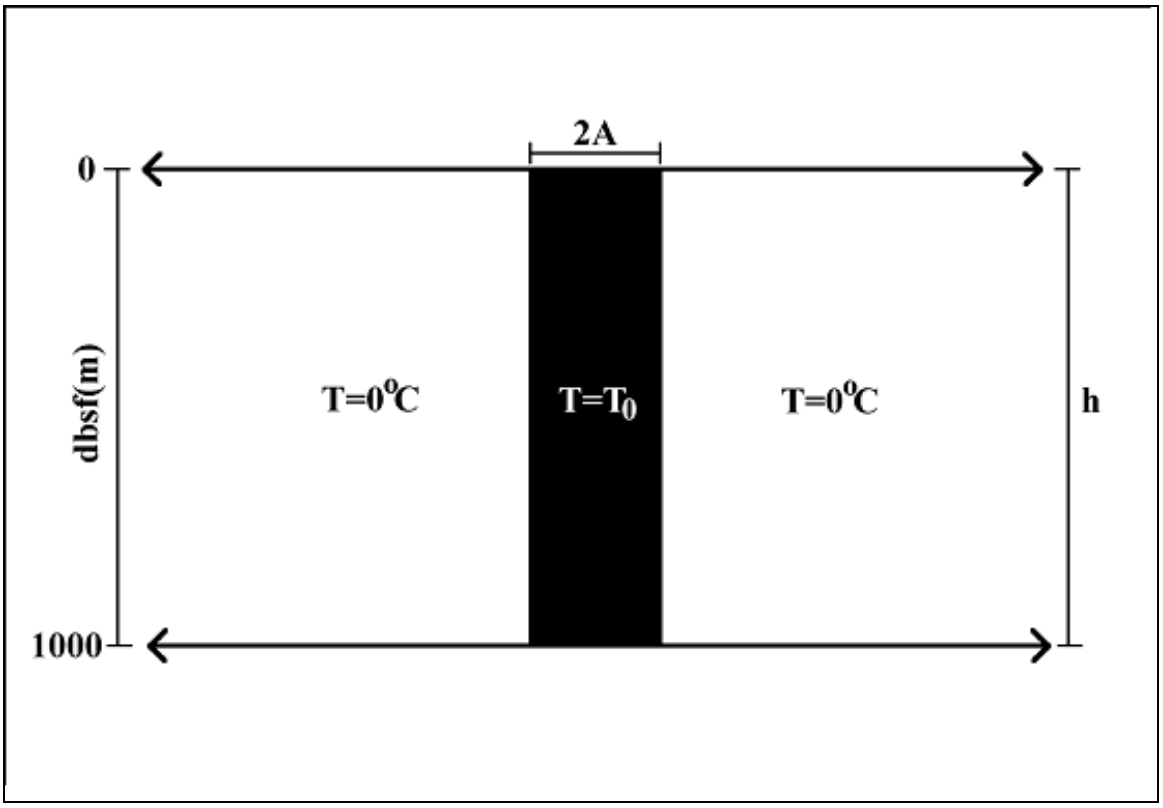

Figure 4 Model geometry showing a dike (black) at temperature T_0 injected into a fluid saturated porous medium at 0°C.

The thermal conduction solution is an obvious simplification because the lateral thermal gradient induced by the cooling dike will drive buoyant circulation near the dike wall, which will change the temperature distribution near the dike. The conduction solution provides a reasonable estimate of the rate of heat transfer from the dike and, as shown below, provides a reasonable estimate of the maximum width of the two-phase region near the dike. Although the solution underestimates the duration of phase separation near the top of the dike, the conduction model provides useful insight into the evolution of vent temperature and salinity at "A" vent. Also, it is important to recognize that there are no known analytical solutions for addressing phase separation in a NaCl-

H_2O solution; consequently, the solutions developed here will provide a simple model that can be used to test later numerical simulations.

After obtaining the conductive solution for the cooling dike at a given time to obtain the temperature field, the equation of state for NaCl-H_2O solution tabulated in Bischoff [1991] is used to determine the width of the two-phase region, the liquid saturation profile, and the density and salinity of liquid and vapor phases below the seafloor. The temperature profile is the same at every depth; consequently, one needs only the saturation and phase densities to calculate the hydrostatic (essentially vapor-static) pressure distribution in the two-phase zone. Then, by examining the conductive solutions at different times, one can determine the evolution and duration of the two-phase region. The tables in Bischoff fall within the region between 300 and 500˚C, and 58 to 580 bars. The temperature increment is 10˚C and pressure increment is 5 bars. Because of the coarse increments in these tables, linear interpolation is used to obtain results with a resolution of 1˚C and 1 bar.

In this model, the equation of state limits the maximum temperature in the region outside the dike to 500˚C. For simplicity, therefore, the dike temperature is taken to be T_0 = 1000 °C and the latent heat of solidification is neglected. Models that included the effect of latent heat, but with lower initial temperatures did not change the results appreciably. As discussed in section 3.3, neglecting the latent heat of vaporization also affects the temperature distribution slightly. This effect is not large because in the low-porosity igneous rocks considered here, thermal diffusivity is largely controlled by the rock. The solution given by the initial value problem for the region for $-\infty < x < \infty$ [Carslaw & Jaeger, 1959] is then:

$$T(x,t) = \frac{1}{2} T_0 \left(erf \frac{A - x}{2\sqrt{at}} + erf \frac{A + x}{2\sqrt{at}} \right) \tag{3.1}$$

where a is the effective thermal diffusivity of the porous medium (I use a commonly accepted value $a = 10^{-6}$ m^2/s) and A is the half-width of the dike.

3.2 Results

Figures 5, 6, 7, and 8 show profiles for the brine and vapor density and salinity, and vapor volume fraction, respectively, at times of 1, 10, and 14 days following emplacement of a 2 m wide dike. The most important results shown in these figures are that the two-phase region is thin (~ 0.2 m) and that the phase separation event near the dike wall is short-lived (~ 16 days). Initially, a thin (~ 0.06 m) zone of halite occurs near the dike margin (Figure 5). Samples of halite taken near the surface of dike-driven hydrothermal vents support the existence of such a region [Butterfield *et. al*., 1997]. Figures 5, 6, and 7 show that the liquid salinity decreases with distance from the dike margin. As a result, the liquid near the dike wall is denser than the cold far-field seawater, and will tend to sink relative to the rock matrix, whereas the liquid near the outer edge of the two-phase zone is less dense than cold seawater and will tend to rise buoyantly despite its elevated salinity. Figure 8 shows that much of the two-phase region is occupied by a low density, low salinity vapor phase that will tend to separate buoyantly from the saline liquid phase and ascend to the seafloor. The results also show that the width of the two-phase zone decreases with depth and that the two-phase region decays from the bottom upward. Both of these results stem from the *P-T-X* phase relations (Figure 2).

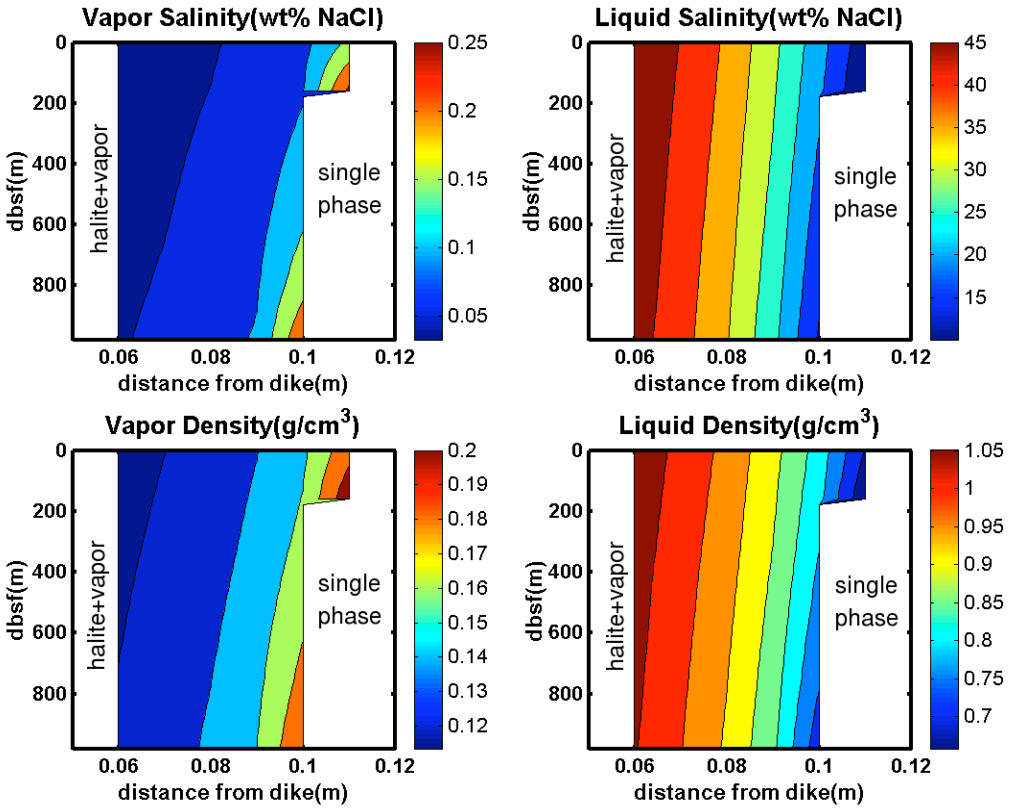

Figure 5 Liquid and vapor densities and salinities for a 2 m wide dike at 1 day.

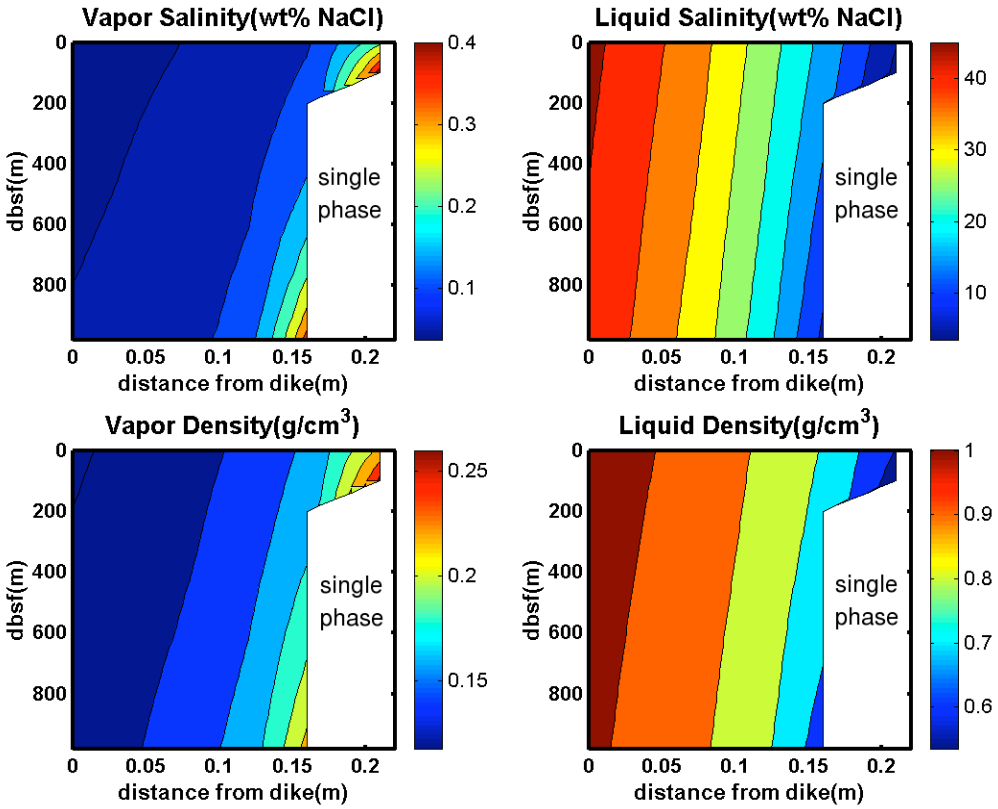

Figure 6 Liquid and vapor densities and salinities for a 2 m wide dike at 10 days.

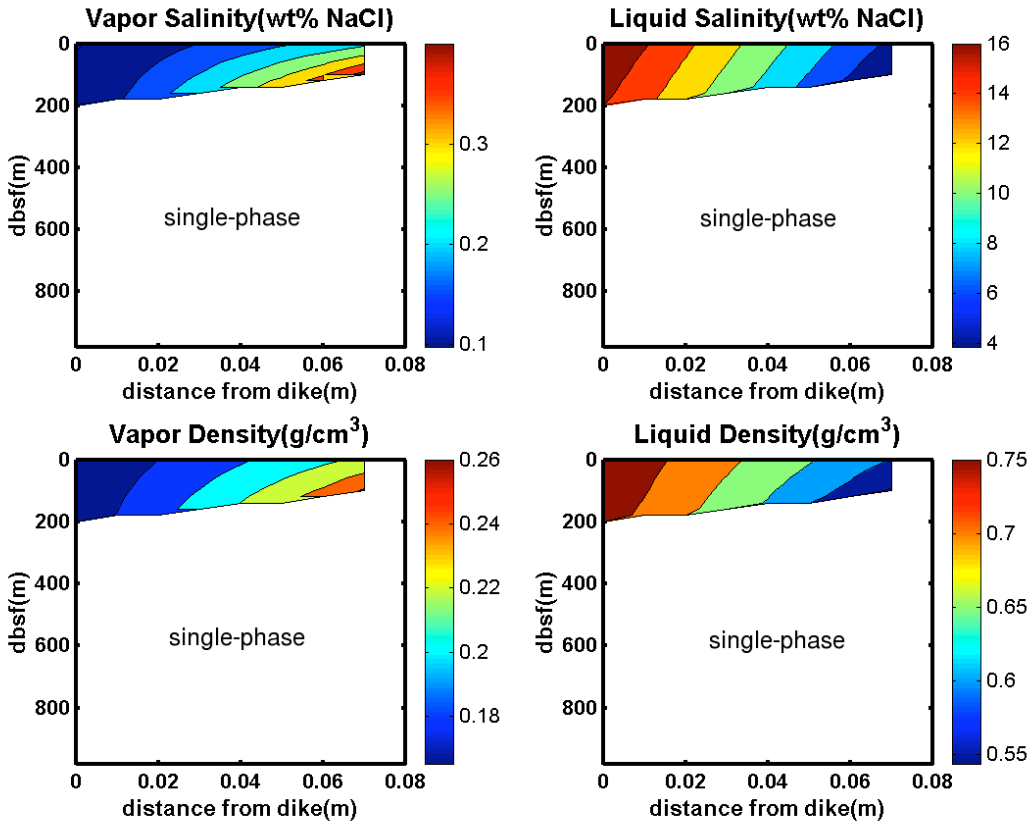

Figure 7 Liquid and vapor densities and salinities for a 2 m wide dike at 14 days.

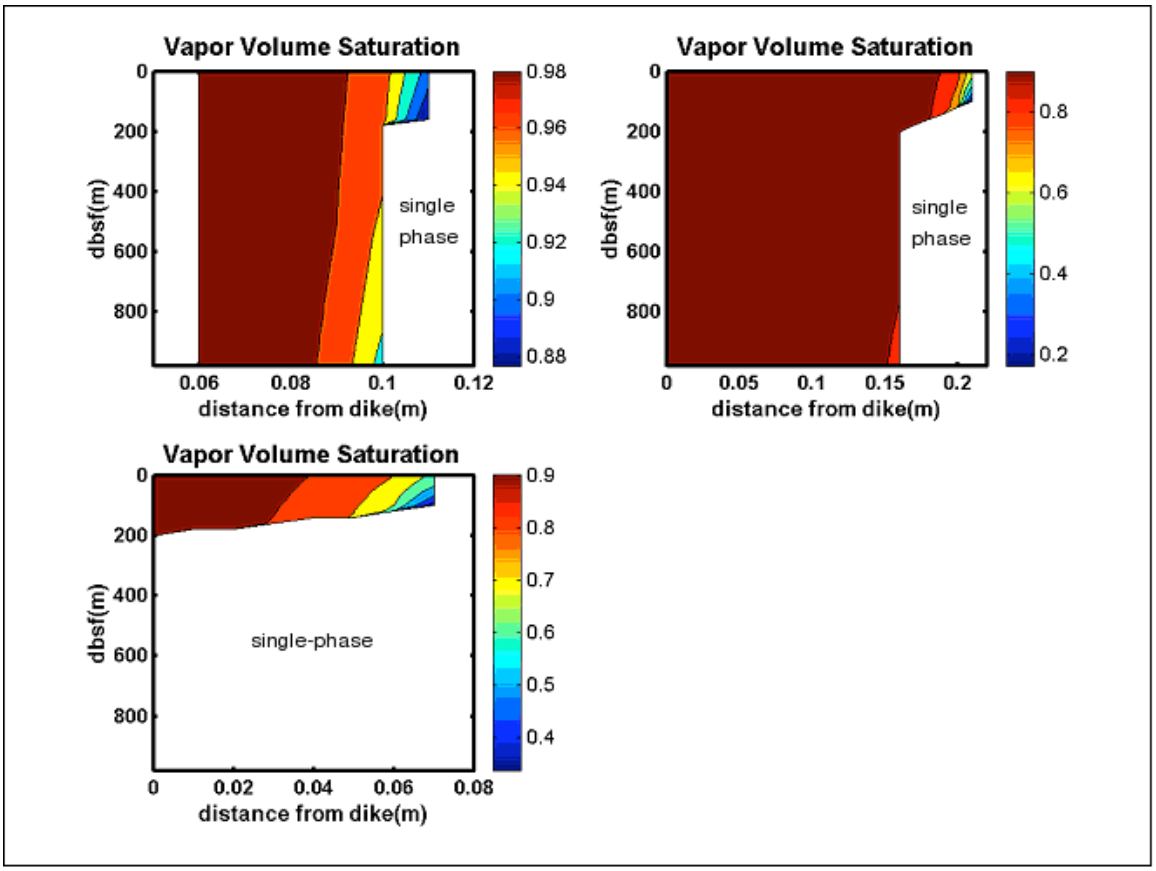

Figure 8 Vapor volume saturation for a 2 m wide dike at 1, 10, and 14 days (from the top left clockwise)

The step in the figures results from the difficulty of interpolating values at the boundary of the two-phase region. At any section of the Bischoff tables representing a constant temperature *P*-*X* slice of the phase diagram for NaCl-H_2O, one can linearly interpolate to obtain a smooth curve separating the two-phase region from the other regions; however, because the data in the tables come from slices that are separated by 10°C, one would have to interpolate again to obtain a smooth three-dimensional surface. This second interpolation is significantly more complicated and would take more time and effort than is justifiable for this simplistic model, considering the increase in precision that one could expect to obtain.

The simple conduction solution provides useful information regarding phase separation processes in NaCl-H_2O fluids near a dike, even though the model is not correct in detail. In the next section this is shown by comparing the results obtained here with those obtained for an analogous problem of transient two-phase flow of seawater near a dike in which the partitioning of salinity between the liquid and vapor phases was neglected [Lowell & Xu, 2000]. The implications of the results obtained from the conduction model in the light of the observations at "A" vent (lower left panel of Figure 1) will then be discussed.

3.3 Discussion

3.3.1 Model Robustness

To address the robustness of the results obtained using the conductive solutions, the results in Figures 5-8 will be compared with those derived from a numerical model of two-phase flow of pure water near a cooling dike that includes the effects of fluid advection and latent heat of vaporization that are neglected here. The numerical simulations are derived using a finite difference code GTHM [Xu, 1996]. In this code, the theory of corresponding states is used to modify the critical point of a saline fluid. For a 3.2 wt% NaCl fluid representing seawater the critical point is $P_c \sim 300$ bars and $T_c \sim$ 407˚C [Bischoff & Rosenbauer, 1988]. In this modified pure water two-phase code, the salt remains in the liquid, and the vapor phase is pure water.

Figure 9 depicts the evolution of two-phase flow in porous medium driven by heat transfer from a 1 km high, 2-m wide cooling dike with an initial enthalpy of 5000 kJ/kg ($T_0 \approx 1100$ ˚C) emplaced in a fluid-saturated medium having a permeability of 10^{-13} m^2. The seafloor pressure of 180 bars is assumed. For the sake of comparison, the vertical

isotherms corresponding to the conduction solution in a medium with an effective diffusivity $a = 10^{-6}$ m^2s^{-1} are also shown. The two-phase region corresponds closely to the 388˚C isotherm. Comparison of the conductive 388˚C isotherm in Figure 9 (similar to the results in Figures 5, 6, and 7) with the advective one shows that the maximum width of the two-phase zone is nearly the same in both cases. The duration of the phase separation event near the top of the dike, however, is much longer in the advective case (more than 28 days instead of 16 days). The greater duration results from the vertical advective transport of heat from the base of the dike to maintain higher temperatures near the dike wall. It is also interesting to note that the two-phase zone initially grows much more rapidly in the conduction solution (left-most panel of Figure 9) than in the advective one. This occurs because the latent heat of vaporization slows the lateral development of the two-phase region. The most important features of Figure 9 are that the two-phase zone is thin (~ 0.2 m), and its duration is relatively short (less than 1 month). If a permeability of 10^{-11} m^2 had been used, the two-phase zone would have been even thinner and been of shorter duration [Lowell & Xu, 2000]. It is also noteworthy that the upward transport of heat by advection does not change the temperature distribution in the two-phase region near the top of the dike appreciably, but only the duration of the two-phase event.

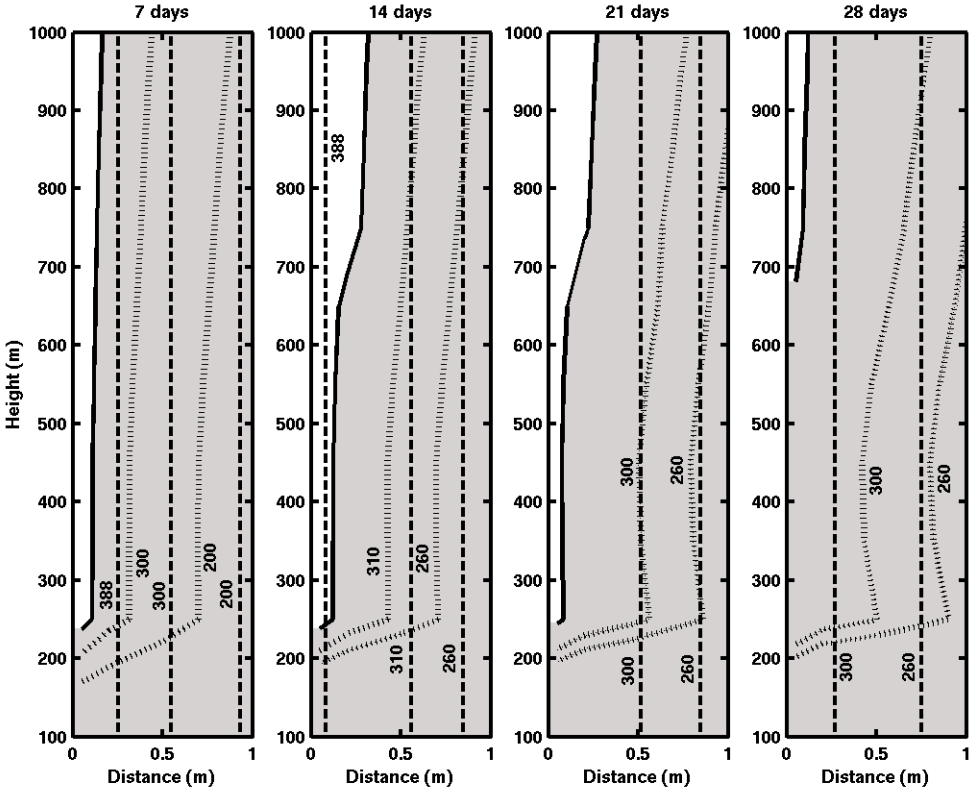

Figure 9 Plot of isotherms in °C near a 2 m wide dike. The vertical dashed lines represent pure conductive isotherms, and the dotted lines represent isotherms from the output of GTHM. The solid line is the 388°C isotherm from GTHM and approximates the single-phase/two-phase boundary.

In the conductive model the latent heat of vaporization could have been accounted for by using an effective thermal diffusivity $a = 3 \times 10^{-7}$ m^2s^{-1} (a factor of 3 smaller). In this case the maximum width of the two-phase zone would not have changed appreciably because this occurs at a distance $x/A \sim 1.25$ [Carslaw & Jaeger, 1959], independent of the value of a. On the other hand, the duration of the two-phase zone $\tau \sim A^2a^{-1}$, so including the affect of latent heat of vaporization would have increased the duration of phase separation by a factor of 3. Figure 10 shows the comparison between the numerical solutions using GTHM and the conductive solution using $a = 3 \times 10^{-7}$ m^2s^{-1}.

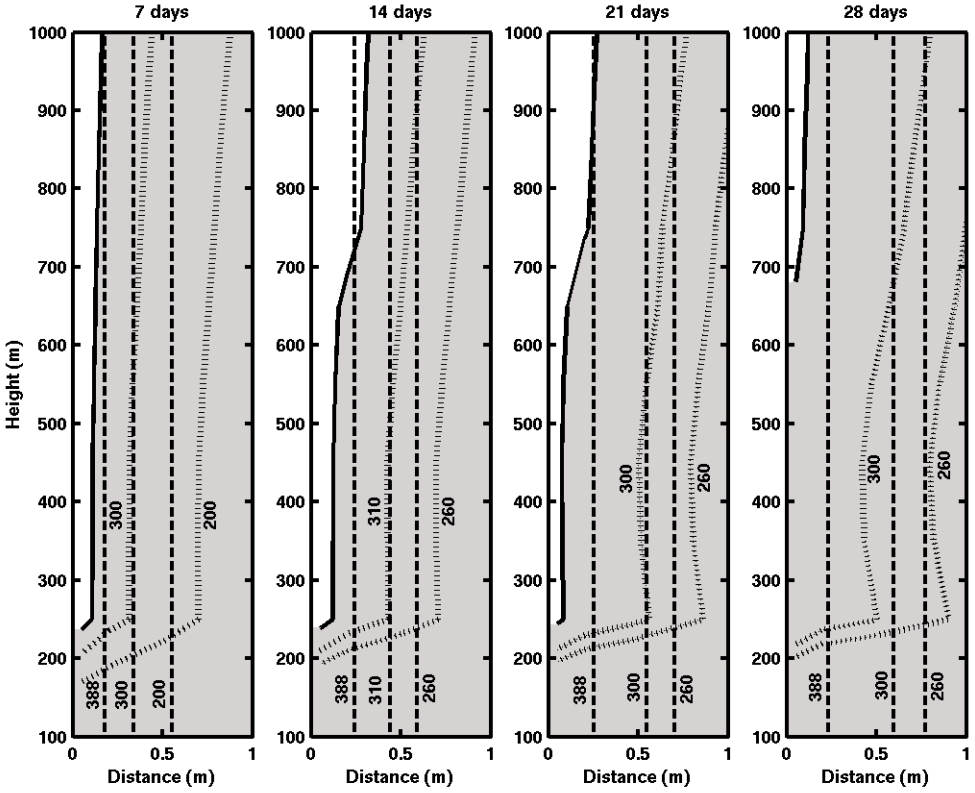

Figure 10 Equivalent to Figure 9, except with conductive isotherms calculated using a thermal diffusivity of $3*10^{-7}$ m^2/s instead of 10^{-6} m^2/s.

The conductive model also neglects the effect of thermal pressurization [Delaney, 1982]. For the deep, high-pressure systems considered here, however, the vapor density is much higher than in shallow sub-aerial systems. Moreover, the relatively high permeabilities that are likely in this setting (see below) suggest that the set up time for advection is much shorter than the duration of two-phase flow [Delaney, 1982]; therefore, neglecting thermal pressurization is most likely not a critical issue.

Finally, it should be pointed out that because advection does not change the magnitude of the temperature near the dike significantly, but only the horizontal temperature gradient and the duration of two-phase flow, the distribution salinity in the

liquid and vapor phases as given by the conductive solutions in Figures 5-8 have the correct horizontal structure, even if not correct in detail. If advection of heat were included in the solutions, similar horizontal salinity distributions would result near the top of the dike, but they would last longer as suggested by Figure 9. In the following section, an attempt is made to compare the salinity distribution derived from the model with observations from "A" vent and consider the advection of salinity resulting from phase separation. Under the assumption of local thermodynamic equilibrium between liquid and vapor phases, advection of salt without changing the lateral thermal structure does not change the salinity distribution between the phases, but only the relative mass fractions (Figure 2).

3.3.2 Salinity vs. time at "A" vent

To compare the results of the model with salinity and temperature at "A" vent (Figure 1, lower left panel), a plot is made of the temperature and vapor salinity averaged across the two-phase region at $z = 0$ for a 2 m wide dike as a function of time (Figure 11). Both the absolute values and general trends of salinity and temperature obtained from the model are inconsistent with "A" vent data. Instead of averaging over the entire two-phase surface, the above analysis was repeated by sampling the salinity values at a variety of single points within the two-phase region at $z = 0$; however, the results were essentially unaltered. More significantly, none of the observed (T, x) values taken at one-week intervals at "A" vent were in equilibrium at the seafloor pressure of 250 bars. Because vapor and brine salinities in the two-phase zone increase and decrease, respectively, with increasing pressure (Figures 5, 6, and 7), it is possible that the observed (T, x) pairs at "A" vent represent fluids that approached equilibrium at pressures greater than 250 bars

and that, during its rapid ascent, the vapor phase may not have maintained thermodynamic equilibrium with its surroundings. Another possibility is that the vent fluid represents a mixture of vapor and brine.

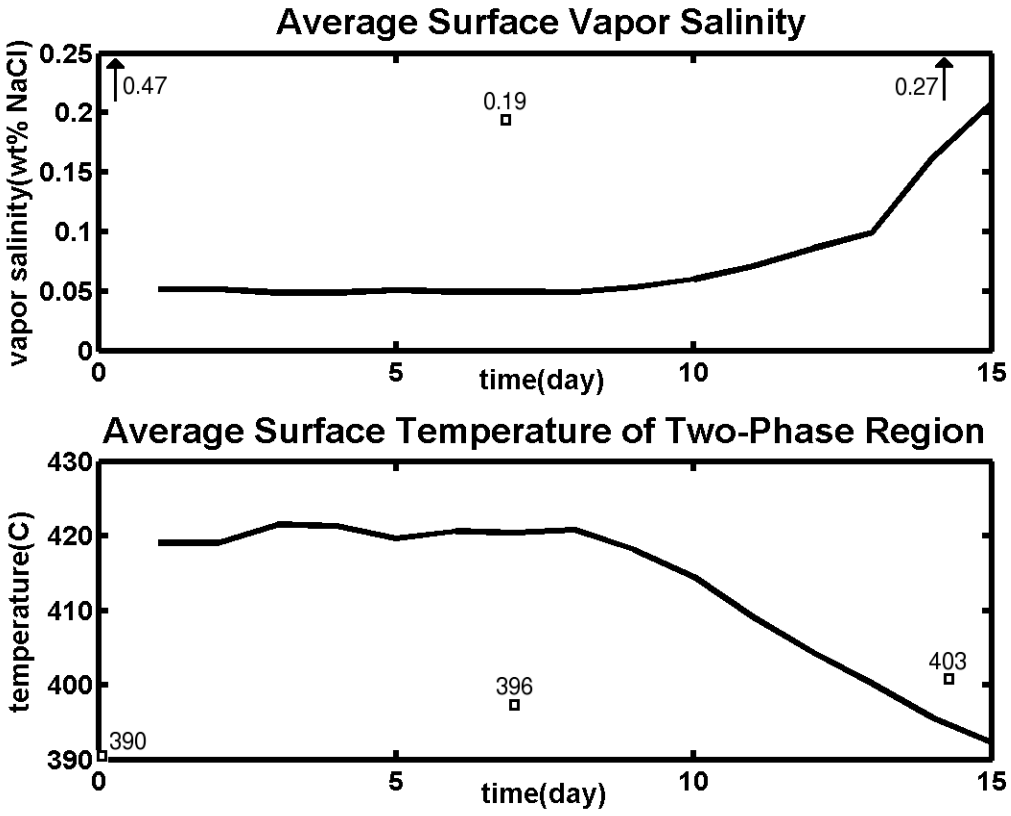

Figure 11 Surface vapor salinities and temperatures calculated using the pure conductive cooling model. Where possible, the actual data are shown with boxes.

To test the idea of disequilibrium, a buoyancy-driven Darcian flow model that is constrained by the observational data from "A" vent is constructed. For simplicity it is assumed that within the two-phase zone, the Darcian velocities (specific discharges) u_v

and u_b of vapor and brine, respectively were driven by the density differences between these fluids and the cold fluid far from the dike. That is,

$$u_v = -\frac{k(1-S)g(\rho_f - \rho_v)}{\mu_v}$$

$$u_b = -\frac{kSg(\rho_f - \rho_b)}{\mu_b} \qquad (3.2)$$

where g is the acceleration due to gravity, k is the rock permeability, S is the volumetric liquid saturation, ρ is the density, and μ is the dynamic viscosity. The subscripts f, b, and v refer to the far field liquid, brine, and vapor, respectively. The negative sign indicates upward flow. The vapor saturation 1-S is essentially constant with depth (Figure 8) and it is assumed that the density of the brine and vapor phases represent averages both across and along the two-phase zone. Because 1 - S ~ 1 and $\rho_v << \rho_f$ (see Figures 5 - 7) and $\mu_v << \mu_b$, it is assumed that the brine phase was stationary with respect to the ascending vapor phase that vented at the seafloor. The validity of this assumption is discussed below.

An attempt is then made to match the temperature and salinity data from "A" vent by determining whether vapor initially in equilibrium at a given temperature and pressure in the two-phase region near a cooling dike could rise and appear at the seafloor at the one-week time intervals observed without undergoing equilibration during its ascent. In constructing this model it is recognized: (a) that the temperature at "A" vent increased from 390˚C (very near the two-phase boundary at 250 bars) to 403˚C, two weeks later (lower left panel of Figure 1) and (b) that steep vertical gradients in vapor salinity occur

only near the edge of the two phase zone (Figures 5-7). It thus suspected that the observed (T, x) values at "A" represent a period in which the two-phase zone is expanding away from the dike wall and that sampling at "A" vent took place near the edge of the two-phase zone. The initial conductive model with thermal diffusivity $a = 10^{-6}$ m^2s^{-1} grows and completely decays within 16 days, so it is impossible to fit the observations with this model. On the other hand, the conductive model of a 2 m wide dike with $a = 3 \times 10^{-7}$ m^2s^{-1} (Figure 10), that more nearly represents the lifetime of a system including advection lasts considerably longer. Hence this model is used to simulate the temperature field. In order to try to match the observed (T, x) data from April 1991 at "A" vent, one needs to consider a region near the dike wall in which the two-phase zone lasts at least two weeks, and in which the temperatures hover near 400˚C.

Figure 12a plots the temperature distribution as a function of time at selected distances from the dike wall using equation (3.1). The horizontal dashed line is the temperature of the edge of the two-phase boundary at the surface (388°C, 250 bars). The vertical dashed lines represent one-week time intervals. In order to sample fluid from the two-phase region, fluid sampled at each week must be at a temperature above the horizontal line. The region surrounded with a square is shown magnified in Figure 12b. The shaded area between 20 and 25 cm from the dike wall is the only region where the temperatures hover near 400˚ for at least two weeks. As is shown below, this area also corresponds to the region from which the appropriate vapor salinities can be advected upward at the observed time interval.

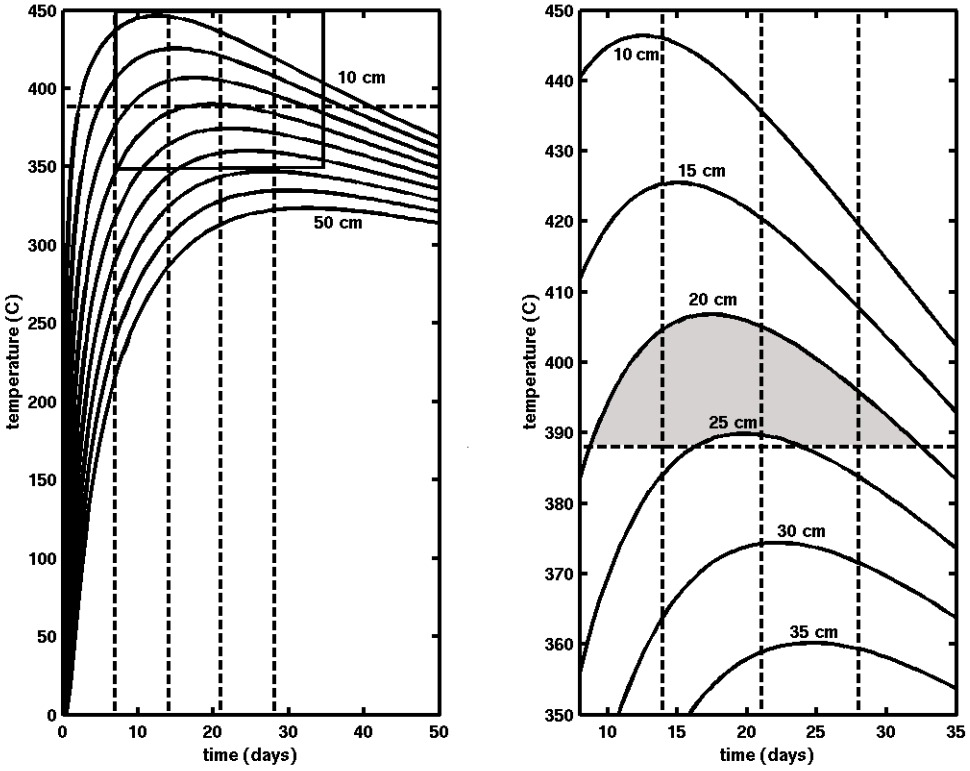

Figure 12 (a) Surface temperature distribution as a function of time at selected distances from the dike wall using equation (1); (b) Magnification of the region surrounded by a square in (a).

To determine the vertical transport of vapor the points 10, 15 and 20 cm from the dike wall at $z = 0$ are considered as the two-phase boundary expands. As vapor and brine form beneath these points, vapor is transported upward at the rate of its Darcian velocity (Equation 3.2) with time steps such that the vapor phase always moves one grid spacing (20 vertical meters) per time step. It is assumed that the rising vapor remains thermally equilibrated even though it is in complete chemical disequilibrium after its initial formation.

By varying the permeability (and thus the velocity), it was attempted to match the short time scale data from "A" vent as the two-phase region expanded past the three

surficial sampling points. The results are shown in Figure 13. The vapor salinity is zero until the edge of the phase boundary reaches the sampling point, when it jumps to ~ 0.24 wt % (corresponding to equilibrium at 390˚C and 250 bars). Then because the vapor salinity decreases with increasing temperature, but increases with increasing pressure, it is found that the values corresponding to the last two salinity data points of 0.19 and 0.27 wt% NaCl at depth below the various sampling points. These salinities are then assumed to be advected upward according to equation (3.2).

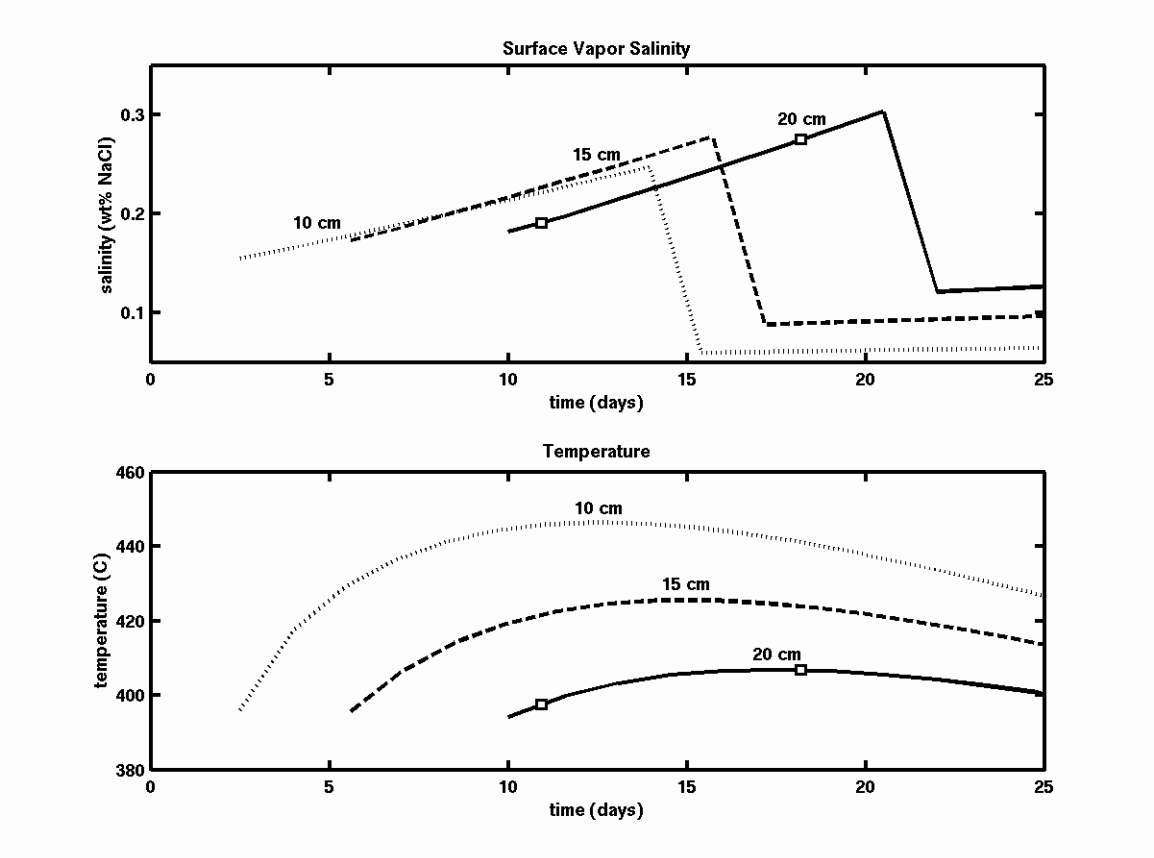

Figure 13 Surface vapor salinities and temperatures calculated for a 2 m wide dike at sampling distances of 10, 15, and 20 cm from the dike wall.

Figure 13 shows that, although the appropriate salinities arrive at the surface at distances less than 20 cm from the dike wall, the temperatures there are much higher than observed. Therefore, if the disequilibrium model has some validity, it suggests that the data at "A" vent was taken ~20-25 cm from the dike wall, where temperatures are much lower. Moreover, the permeability at these distances would need to be ~ 2 x 10^{-13} m^2 in order for the observed salinity values to arrive 1 week apart. Given this permeability value, Figure 13 shows the time interval separating the arrival of appropriate salinity values less than 20 cm away from the dike is smaller than observed.

The inability of the model to match the first salinity datum (0.47 wt% NaCl) was not surprising because this value was much higher than the other two. If this point represents an equilibrium vapor salinity, all the vapor salinities in the system below that point would have to be greater than this value, because, at any given time, the vapor salinity increases with depth. The first datum may represent a mixture of vapor and brine. Mass balance calculations show that a mixture of about 5 wt% brine in equilibrium with vapor at 250 bars would give the observed vent salinity. The appearance of a brine-vapor mixture in the early stages of discharge may be analogous to the initial stages of geyser activity in which relatively liquid rich fluids are followed by more vapor rich ones [Ingebritsen & Rojstaczer, 1996].

Another possibility is that the observed time series of salinity at "A" vent represents a mixture of brine with vapor. Although brine transport was neglected in the disequilibrium model, the density distribution in the two-phase zone shows that $\rho_b > \rho_f$ near the dike wall but $< \rho_f$ near the edge of the two-phase zone (Figures 5-7). Thus the brine phase may be either rising or sinking relative to the cold far-field fluid. On average,

however, $\rho_b < \rho_f$, so even though the vapor is ascending much more rapidly than brine it is likely that the sampled vent fluid is a mix of brine and vapor. This is the best explanation for the first datum at "A" vent. Mass balance calculations show that less than 1 wt% brine mixed with the equilibrium vapor at "A" vent would yield the observed vent salinity. A complete numerical model of two-phase flow of seawater near a dike would also help determine whether disequilibrium or mixing is the more likely explanation of the salinity data.

3.3.3 Evolution of vent salinity following diking events

The model presented here indicates that the phase separation occurring after dike emplacement results in venting of mainly the vapor phase. Halite and high-salinity brine are sequestered in the porous rock during the two-phase flow. After the two-phase flow ceases, the residual brine will mix with single-phase seawater. Because the two-phase zone disappears from below, and because the brine salinity decreases with depth, the first brine to emerge at the surface should have a very high salinity. If little mixing with seawater occurs, it could in fact be the conjugate of the vapor phase. The transition from vapor salinity to brine salinity may be quite sharp. Moreover, because the salinity of the residual brine decreases with depth and mixing with seawater increases with depth, the salinity of the venting brine should decrease with time. Eventually, the vent salinity should return to normal.

If two-phase flow results solely from dike emplacement, the vent temperature should drop rapidly with time (~ weeks to months) and the vent salinity should return to the seawater value on a similar time scale (Figure 14). An episode of brine venting may have occurred at "A" vent but ended prior to sampling in 1992.

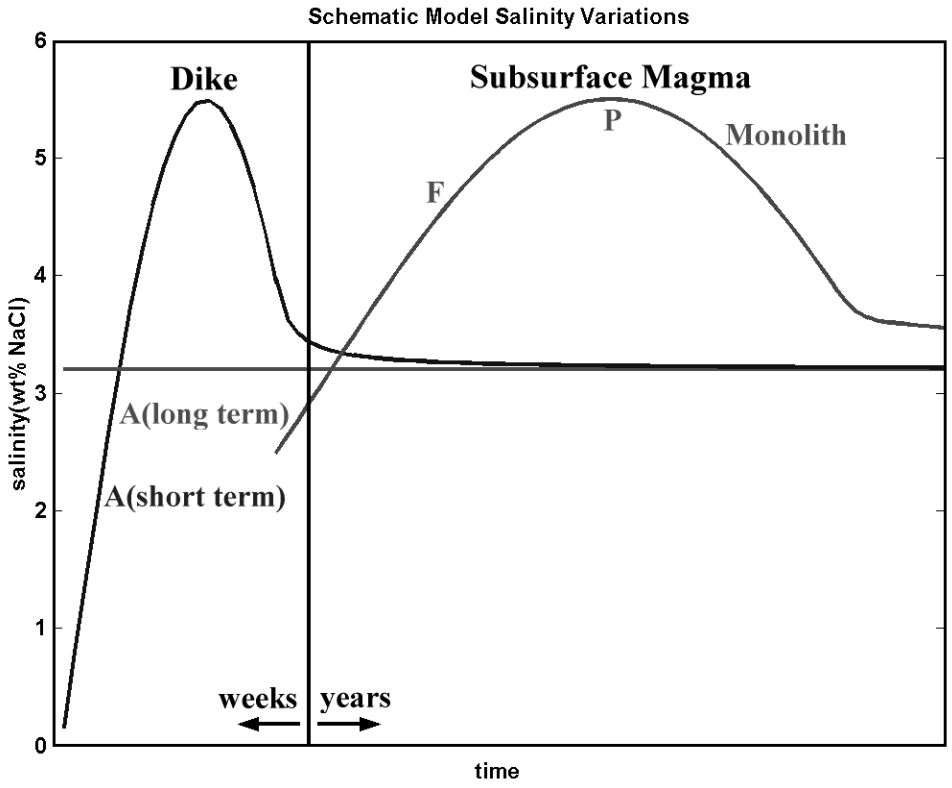

Figure 14 Conceptual model of salinity variation with time at hydrothermal vents as a result of different temporal scales of phase separation processes.

If magma emplacement at depth also drives the system, then two-phase flow and phase separation will also occur there. Because it takes time for this deep-seated fluid to traverse the system, this phase-separated fluid may not appear for some time. It is possible that such fluid could mix with brine generated by phase separation following dike emplacement. In vents discharging phase-separated fluid from depth, the initial vent salinity may be less than seawater and gradually grow with time (e.g. "A" vent from 1991 to 1994, Figure 1). Brine from depth may appear at later times ("F" vent between 1991 and 1994, Figure 1). Finally, as seawater dilutes the brine, the salinity would gradually

return to normal (e.g., Monolith vent on the Juan de Fuca Ridge, Figure 1). The gradual fall of vent salinity with time may result from simple dilution, but it may also in part reflect the initial distribution of brine formed in the system. The lifetime salinity values of "P" vent at EPR 9˚N exemplify these schematic model variations; however, actual systems will often be more complicated than this schematic model suggests. For instance, Bio9 and Bio9' increased toward seawater salinity over a number of years, but began to decrease steeply before they ever reached this value. This may have occurred because the system has been rejuvenated and is again undergoing active phase separation.

3.4 Conclusions from the quasi-numerical approach

Though it does not take advective heat or solute transfer into account, the model offers some insight into the nature of phase separation of seawater near an igneous dike. The model provides some limits on the duration and width of the two-phase zone. It predicts the existence of a halite region near the dike interface, consistent with in situ observations of halite around vent openings. Finally, it shows that at least a small degree of the widening of the two-phase region with height will occur purely as pressure effect, and that the two-phase region would decay from the bottom upwards.

This model cannot explain the variation in the salinity at vent "A" on the EPR, but incorporating a simple fluid advection model suggests that either disequilibrium during upward vapor transport or near-surface mixing between brine and vapor phases is important. A broad schematic picture of salinity evolution related to diking or deeper magma intrusions was also outlined.

CHAPTER 4: THE INTRODUCTION OF A FULLY NUMERICAL METHOD[3]

A fully numerical code for modeling NaCl-H_2O hydrothermal systems will now be constructed by combining a finite volume equation solver with equations of state comprised of thermodynamic lookup tables. The equation solver will be described by giving an account of the equations it uses, the way these equations are discretized, and the method by which the interdependent components of the equations are coupled together in a time marching scheme.

4.1 Other Existing Numerical Approaches

At present, there are two numerical schemes, besides the one developed in this thesis, suitable for simulating fluid flow in seafloor hydrothermal systems. First, there is the code NaCl-TOUGH2 (Kissling, 2005a, b), which extends the widely used TOUGH2 to handle fluids containing NaCl. NaCl-TOUGH2 uses equations of state developed by Palliser and Mckibbin (1998a, b, c). While these are adequate for regions of phase space that are below the critical point of pure water, the bulk quantities above the critical point meander unreasonably (see Figure 15) in several regions of *P-T-X* space, and unphysical behavior arises near the pure water critical point itself. For instance, negative heat capacities result from decreasing enthalpy with increasing temperature at constant salinity just above the critical point. These imply negative heat capacities and are therefore unphysical. Because a great many phenomena of interest in seafloor hydrothermal systems involve fluids in thermodynamic regimes including the pure water critical point and regions above this point, NaCl-TOUGH2 is unfortunately not adequate for studying these systems. The enthalpies to be used in this study do not share the problems of

[3] This chapter describes the theoretical framework behind FISHES – for a guide to the practical use of this code, see Appendix 3.

Palliser and Mckibbin's. Second, there is the code of Geiger et al. (2006a, b), which uses equations of state developed by Driesner and Heinrich (2005) and Driesner (2005). This code, in addition to having equations of state that avoid the problems of Palliser and Mckibbin's formulation, can also employ non-rectangular meshes, making it able to resolve complex geological features. Because of these considerations, as well as others, it is likely to be very well equipped for studying fluid flow in seafloor hydrothermal systems; however, neither this code nor the equations of state from Driesner et al. were available for public use when the author decided to embark on numerical methods (indeed, they aren't available now either). Furthermore, it is important for different numerical schemes to co-exist, because they can serve as checks on each others' results, and may yield different and yet equally valid insights about a given flow phenomena. Finally, although I do not wish to imply that the code FISHES is superior to that of Geiger et al. (or for that matter, to that of Kissling aside from the equations of state issue), this code does have certain advantages of its own:

- It is written in FORTRAN 90, which avoids the typical problems of FORTRAN 77 and reinforces sound programming practices. Although FORTRAN 90 is not an object-oriented language, it is arguably easier to learn and read than languages such as C++. Kissling's code is written in FORTRAN 77, and Geiger et al.'s is written in C++.
- FISHES was written with explicit intent to be easy for others not familiar with it to be able to learn, use, and modify. As such, it is internally documented, and nearly all the variables have intuitive names.

As mentioned below (section 4.2), the code uses exclusively the finite volume method, which has a very direct and meaningful physical interpretation. Geiger et al. use the finite volume method on the hyperbolic parts of their equations, but they use the Bubnov-Galerkin method on the parabolic parts (as well as on the pressure equation), and this approach has no easy physical interpretation of which I am aware.

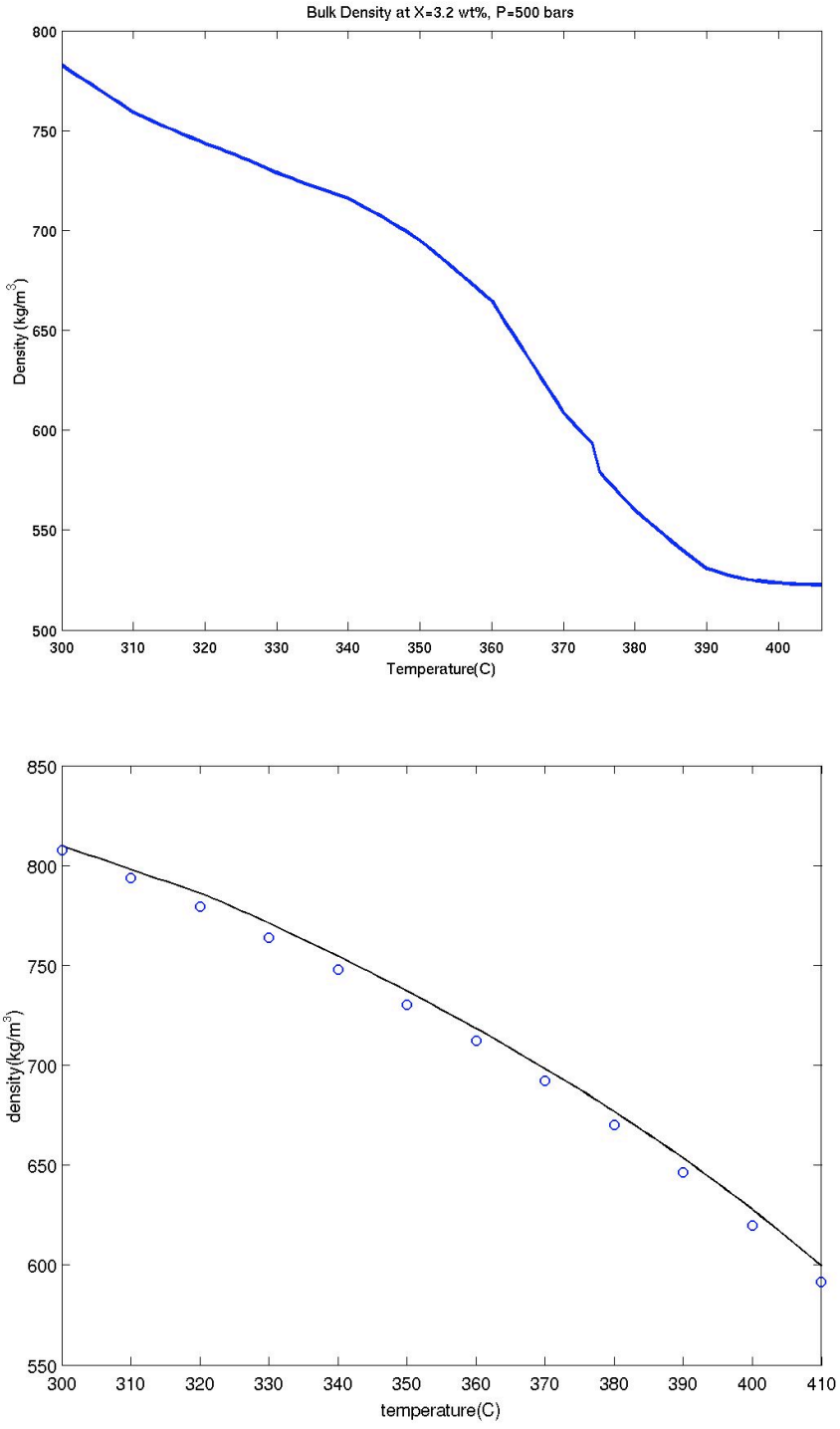

Figure 15 Bulk densities at 500 bars and 3.2 wt% NaCl obtained using the correlation equations of Palliser and Mckibbin (1998a,b,c) (top plot); bulk densities at the same salinity and pressure calculated from the equations of state FISHES uses (bottom plot). Blue circles represent values taken from Bischoff and Rosenbauer [1985].

4.2 The Equation Solver

The equations that govern the conservation of mass and energy in NaCl-H_2O systems are derived in Faust and Mercer [1979a]. The specific forms of these equations, from which are derived the equations used in FISHES, are as follows: the mass continuity equation is

$$\begin{aligned} &\frac{\partial(\phi\rho)}{\partial t} + \nabla\cdot(\rho_v\vec{v}_v + \rho_l\vec{v}_l) = 0 \\ &\vec{v}_v = -\frac{Kk_{rv}}{\mu_v}(\nabla P - \rho_v g\nabla z) \\ &\vec{v}_l = -\frac{Kk_{rl}}{\mu_l}(\nabla P - \rho_l g\nabla z) \end{aligned} \tag{4.1}$$

where ϕ is the porosity, ρ is the density, v is the Darcian velocity, K is the permeability, k_r is the relative permeability, P is the pressure, z is the depth, μ is the dynamic viscosity, g is the gravitational acceleration, and the subscripts v and l refer to the vapor and liquid phases, respectively; and the energy conservation equation is

$$\frac{\partial}{\partial t}[\phi\rho h + (1-\phi)\rho_r c_r T] + \nabla\cdot(\rho_v h_v\vec{v}_v + \rho_l h_l\vec{v}_l) = \nabla\cdot(\lambda_m\nabla T) \tag{4.2}$$

where h is the specific enthalpy, T is the temperature, λ_m is the effective medium thermal conductivity, and the subscript r refers to the rock; ρ and h without subscripts refer to bulk quantities. In addition to these equations, an equation describing salt conservation is needed; hence, the following equation from Bai et al. [2003] is added:

$$\frac{\partial}{\partial t}(\phi\rho X) + \nabla\cdot(\rho_v\vec{v}_v X_v + \rho_l\vec{v}_l X_l) = \nabla\cdot(\phi\rho_l D\nabla X_l + \phi\rho_v D\nabla X_v) \tag{4.3}$$

where X is the bulk salinity and D is the salt chemical diffusivity (taken to be $1\text{x}10^{-9}$ m^2/s in this thesis[4]). Because the system consists of two components, three independent variables are needed to characterize the state of the system. These are the pressure, temperature, and bulk salinity, obtained from solving equations (4.1), (4.2), and (4.3), respectively. To supply (4.1a) with an unsteady term in the pressure, the time derivative term is rewritten as

$$\frac{\partial(\phi\rho)}{\partial t} = \varphi\left[\frac{\partial\rho}{\partial P}\frac{\partial P}{\partial t} + \frac{\partial\rho}{\partial X}\frac{\partial X}{\partial t} + \frac{\partial\rho}{\partial T}\frac{\partial T}{\partial t}\right] \tag{4.4}$$

and the derivatives involving X and T are evaluated as source terms. To supply (4.2) with advective terms in the temperature, the enthalpy advection terms are rewritten as

$$\nabla\cdot(\rho_v c_v \vec{v}_v T + \rho_l c_l \vec{v}_l T) \tag{4.5}$$

where

$$\begin{aligned} c_v &= \frac{h_v}{T} \\ c_l &= \frac{h_l}{T} \end{aligned} \tag{4.6}$$

Also, the derivative of the product of ϕ, ρ, and h in (4.2) is rewritten as

$$\frac{\partial(\varphi\rho h)}{\partial t} = h\frac{\partial(\varphi\rho)}{\partial t} + \varphi\rho\frac{\partial h}{\partial t} = -h\nabla\cdot(\rho_v\vec{v}_v + \rho_l\vec{v}_l) + \varphi\rho\frac{\partial h}{\partial t} \tag{4.7}$$

using (4.1a), to make explicit the coupling with the mass conservation equation. Equations (4.1), (4.2), and (4.3) with the changes indicated in (4.4), (4.5), (4.6), and (4.7)

[4] Na^+ actually diffuses less rapidly than Cl^-, which would seem to imply a need for two chemical diffusivities for aqueous NaCl; however, due to mutual molecular attraction, the diffusion of the Cl^- ion is limited by that of the more slowly diffusing Na^+, resulting in a single diffusivity for aqueous NaCl that is strongly weighted toward the diffusivity for Na^+ [Cussler, 1984].

are solved in FISHES using the finite volume method, as developed in Patankar [1980], with upstream weighting applied to the coefficients of the temperature equation. For the time marching, the fully implicit method was used for all three equations, so that the newest available values of T, P, and X dominate over each time step. To see derivations of the fully discretized forms of the temperature, pressure, and salinity equations, see Appendix 1. Iteration loops with relative convergence criteria can be turned on or off in the input files. Additionally, to avoid having to use an impractically small time step size for some simulations, under-relaxation is used. Using this method, if ξ is the most recent solution of its corresponding equation, then the new value of ξ is set to

$$\xi_{new} = \xi_{old} + R(\xi - \xi_{old}) \tag{4.8}$$

where R is the relaxation factor and ξ_{old} is the value of ξ at the end of the last time step. R is between zero and unity, with unity corresponding to no under-relaxation and zero corresponding to the case where ξ is held constant in time. Under-relaxation causes ξ to evolve more slowly with time than it otherwise would, and so an iteration number adjustment parameter is available, which causes the code to solve the equation for ξ a number of extra times at each time marching step. This parameter thus makes it possible to avoid the problem of reduced time-accuracy in situations where the code can be calibrated for a given system geometry against known results for some simple scenario. Under-relaxation without iteration number adjustment is often necessary for solving the salinity equation, because equation (4.3) makes it necessary to solve for the convection and diffusion terms as "source" terms, which causes salt to be transported too rapidly in many cases in the absence of under-relaxation. $R = 0.1$ results in adequate salt transport rates for most of the cases considered in this thesis.

Values of parameters such as the liquid and vapor salinities are evaluated at node interfaces using upstream weighting. While this method causes numerical dispersion, the amount of dispersion in the temperature is small compared to the effects of heat conduction, and although the numerical dispersion is not small compared to the effects of salt diffusion, mechanical dispersion of salt is not included and would tend to make salinity profiles sharper than they would be otherwise. Hence, numerical dispersion can to some degree simulate the mechanical dispersion that is not included. In the absence of information that would constrain the components of a dispersion tensor, this way of handling dispersion is reasonable. Figure 16 is a schematic outline of the general code algorithm. No steps for calculating the initial hydrostatic pressure are included because these pressures are computed from the whole code, with the results inserted back into the input files, before any non-hydrostatic simulations are begun.

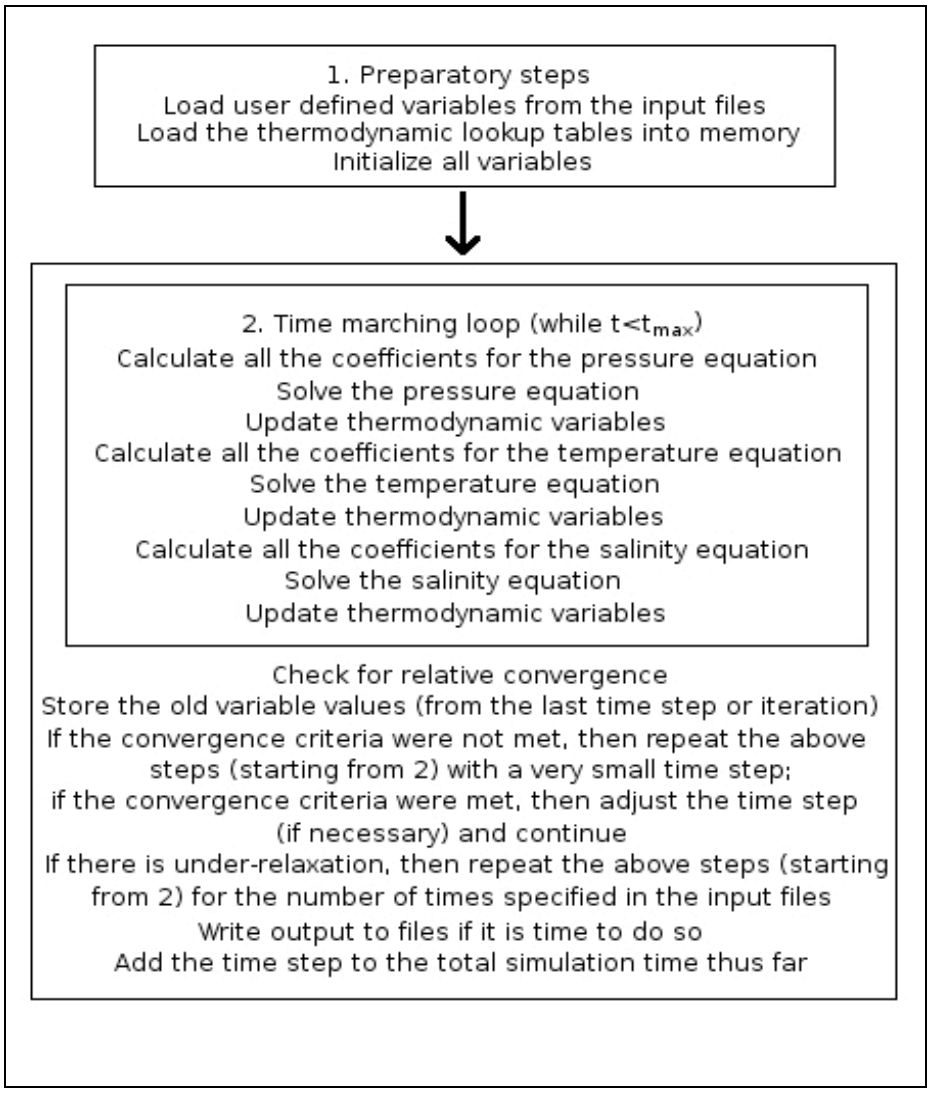

Figure 16 Schematic outline of the main algorithm for FISHES.

4.3 Thermodynamic Properties

The densities, salinities, and enthalpies as functions of *P-T-X* are evaluated via linear interpolation between values in thermodynamic lookup tables[5]. These tables are valid for pressures between 85 bars and 1 kbar, temperatures between 0° and 800° C, and salinities between 0 and 100 wt% NaCl. For the bulk densities above 300°C as well as for

[5] To see how the interpolations are carried out in detail, see Appendix 2.

values of the salinity and density on the upper boundary of the two-phase region above this temperature, these tables were compiled using a computer program developed by A. Anderko, which is based upon the theoretical free energy framework presented in Anderko [1993]. This framework is only valid for temperatures between 300° and 800°C; however, the two-phase region does not exist below 300°C and pressures above 85 bars, because the critical curve drops below that pressure for temperatures lower than 300°C. For the bulk density values from 300°C to 0°C, a program developed by D. Archer was used, based upon the framework presented in Archer [1992]. Specific enthalpies between 300° and 600°C were compiled using the framework of Tanger and Pitzer [1989]. Enthalpies below 300°C were compiled by integrating specific heats derived from Archer's program (mentioned above) from 300°C downward, and using the enthalpies at 300°C to solve for the first constants of integration. Enthalpies between 600° and 800°C were compiled by integrating the specific heats at 600°C (from Tanger and Pitzer [1989]) upward, using the enthalpies at 600°C to solve for the first constants of integration. Enthalpies on the upper boundary of the two-phase region are calculated from the bulk enthalpies at the *T-P-X* values on that surface. Finally, the salinities on the salt saturated vapor surface were obtained using the correlation equation from Palliser and Mckibbin [1998a], and the other quantities on that surface are obtained from the bulk quantities at the *P-T-X* values on that surface. The densities and salinities on the upper boundary of the two-phase region are shown in Figures 17 and 18, respectively. Figures 19 and 20 show the bulk density and enthalpy as functions of constant composition at 250 bars for temperatures between 200 and 450°C. It is important to note that the values near the transition point at 300°C between the different frameworks for density and enthalpy are

smooth. The trajectories along which the densities and enthalpies are being evaluated crosses the upper boundary of the two-phase region when the temperature is near 390°C; as can be seen from the figures, values near this transition point are also smooth. Some of the density curves were compared with those of T. Driesner in private correspondence and found to agree quite well. Figure 17 show ripples on the upper boundary of the two-phase region, but these oscillations are a plot artifact. For comparison, Figure 21 shows a typical segment of densities along the upper boundary of the two-phase region with increasing temperatures and a constant pressure and salinity of 400 bars and 50.0 wt% NaCl, respectively (the high pressure was chosen so that a large portion of the surface could be traversed by a single density curve). The apparent waviness in Figure 18 for lower temperatures is also a plot artifact.

Foustoukos and Seyfried [2007a] have performed experimental measurements of vapor salinities along the upper left boundary of the two-phase region near the 3-phase pressure and extending to the salt saturated vapor surface below the 3-phase boundary. Figure 22 shows a comparison of their experimental results and the values of vapor salinity predicted from the equations of state described above. There is strong agreement between the predicted and measured values of vapor salinity. Foustoukos and Seyfried [2007a] have also investigated partitioning of Li, Br, Rb, Cs, and B along these phase equilibria surfaces. For a review of the current state of knowledge concerning partitioning of elements between phases in the NaCl-H_2O system, see Foustoukos and Seyfried [2007b]; for an experimental study of quartz partitioning in this system, see Foustoukos and Seyfried [2007c].

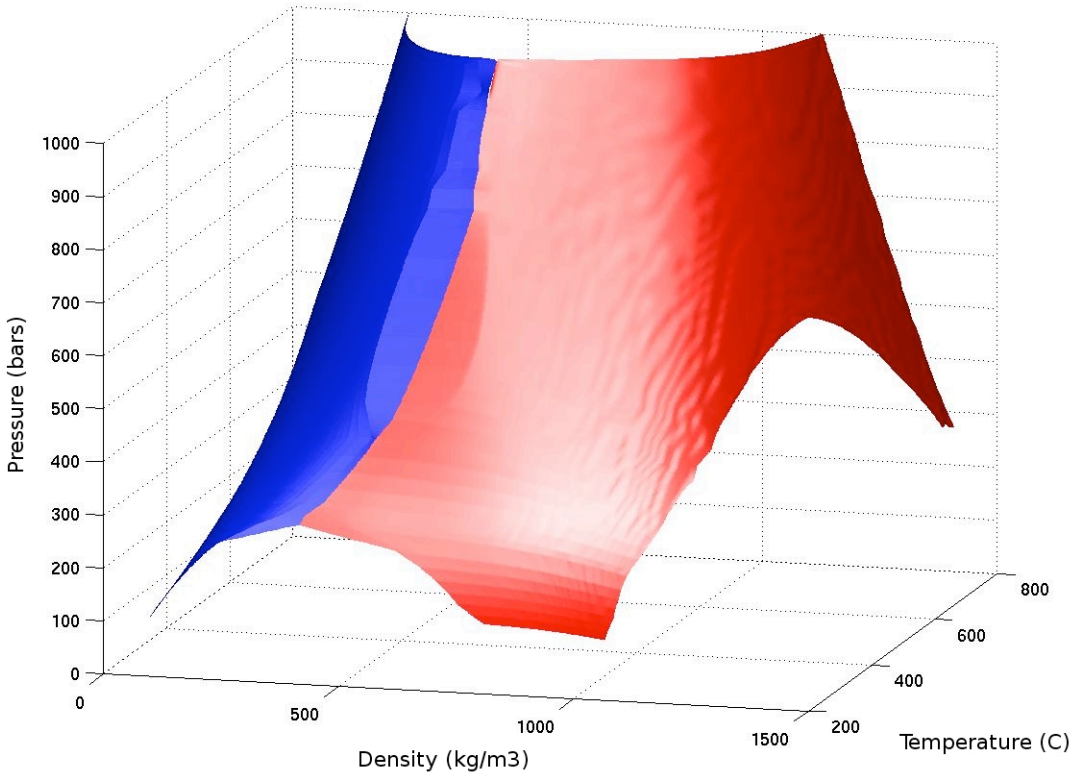

Figure 17 Densities on the surface of the two-phase region, calculated via linear interpolation between table values based on Anderko [1993].

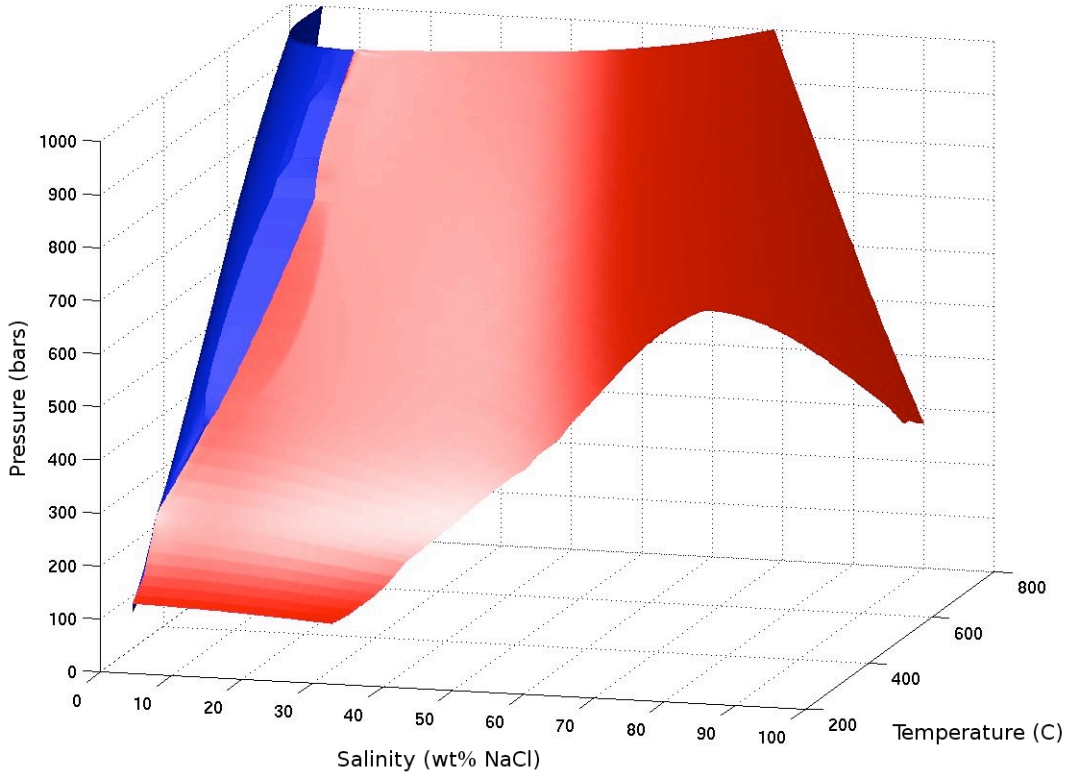

Figure 18 Salinities on the surface of the two-phase region, calculated via linear interpolation between table values based on Anderko [1993].

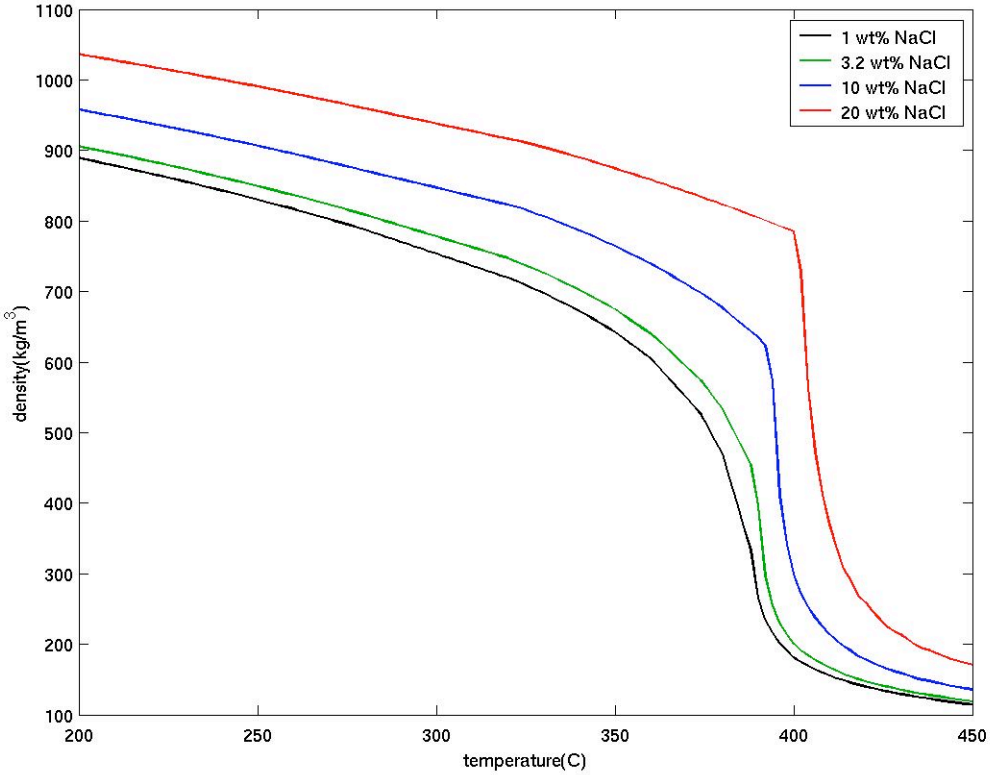

Figure 19 Bulk density as a function temperature and constant composition at 250 bars.

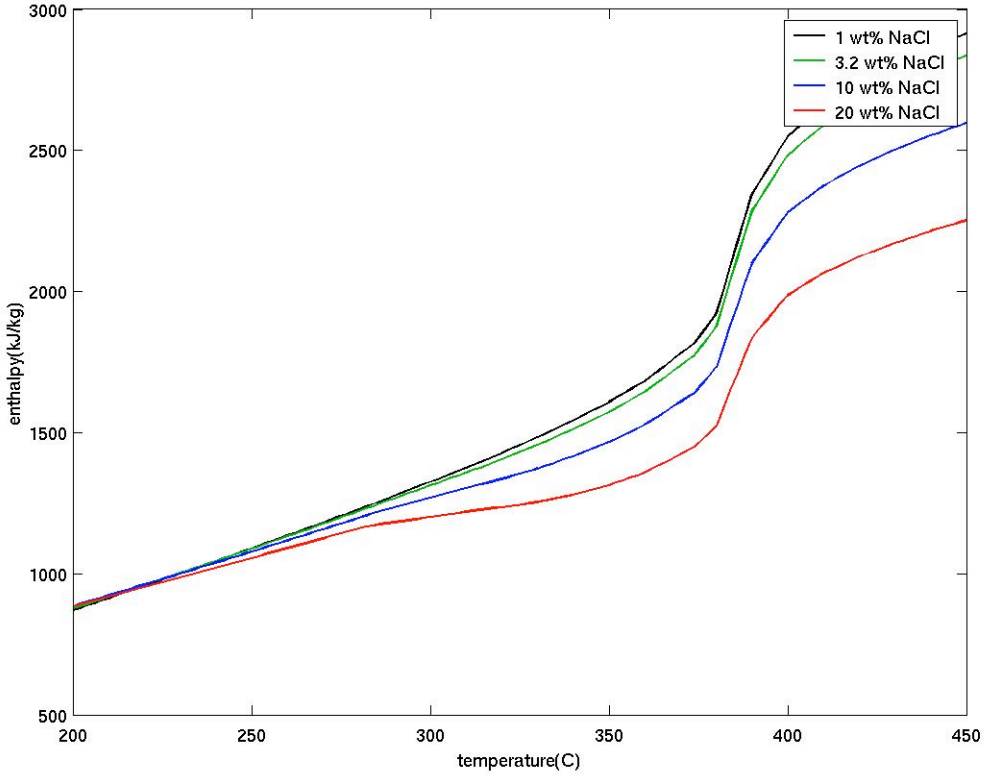

Figure 20 Bulk specific enthalpy as a function temperature and constant composition at 250 bars.

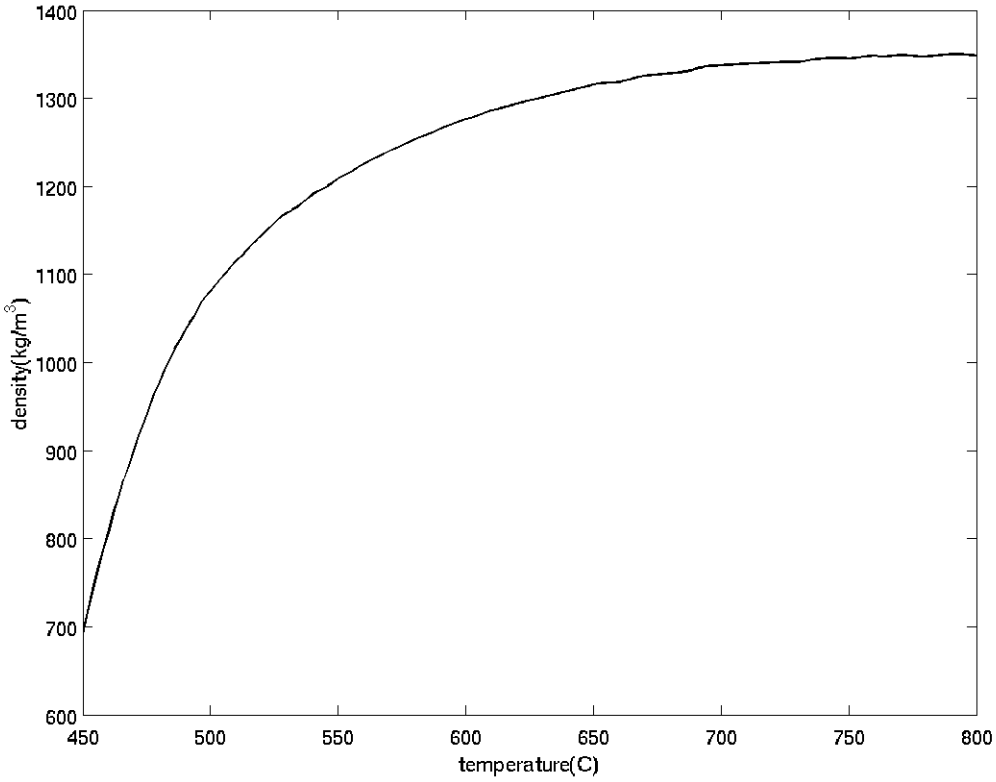

Figure 21 Density as a function of temperature for P = 400 bars and X = 50.0 wt% NaCl along the liquid side of the upper boundary of the two-phase region.

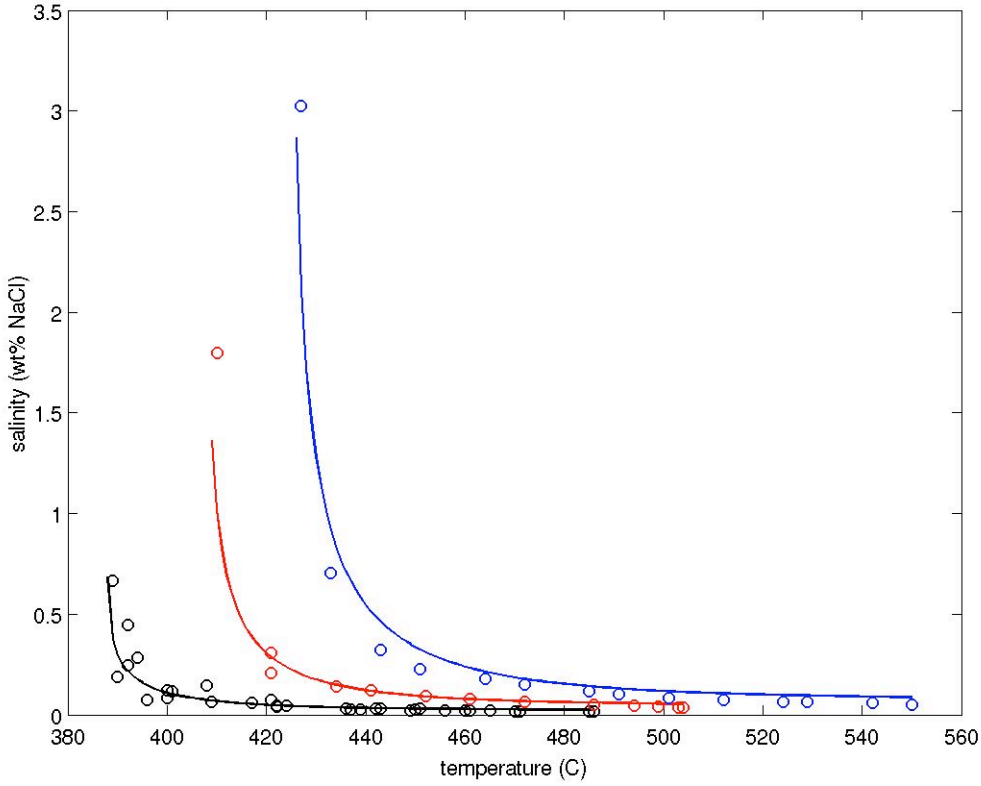

Figure 22 Comparison between vapor salinity values predicted from the equations of state used in FISHES and the experimental measurements carried out by Foustoukos and Seyfried [2007]. Solid curves represent predicted values and circles represent measurements. Black, red, and blue represent values at pressures of 250 bars, 300 bars, and 350 bars, respectively.

In the two-phase region, the liquid volume saturation is calculated according to

$$S_l = \frac{\rho_v (X_v - X)}{\rho_v (X_v - X) + \rho (X - X_l)} \tag{4.9}$$

and the vapor volume saturation $S_v = 1 - S_l$. The relative permeabilities for the liquid and vapor phases are set equal to S_l and S_v, respectively. For regions in which halite can precipitate, the halite saturation is calculated according to

$$S_H = \frac{\rho_l (X_l - X_{l3})}{\rho_H (1 - X_l) + \rho_l (X_l - X_{l3})} \tag{4.10}$$

and

$$S_H = \frac{\rho_v (X_v - X_{v3})}{\rho_H (1 - X_v) + \rho_v (X_v - X_{v3})} \tag{4.11}$$

for the liquid plus halite and vapor plus halite regions, respectively. ρ_h is the halite density, X_{l3} is the salinity at the point where the liquid side of the upper-boundary of the two-phase surface meets the 3-phase coexistence surface, and X_{v3} is the salinity at the point where the vapor side of the upper-boundary meets the 3-phase surface. Equations (4.10) and (4.11) assume that the mass fraction of halite is a linear function from zero halite at X_{l3} and X_{v3} to the pore space being completely filled with halite at X=1. The porosity is adjusted as

$$\phi = \phi_0 (1 - S_H) \tag{4.12}$$

where ϕ_0 is the initial porosity. Unless some specific relationship between the porosity and the permeability is being assumed, such as the Kozeny-Carman equation [Carman, 1956], the relative permeabilities are also each multiplied by one minus the halite saturation. Also, due to lack of available information to constrain a more sophisticated approach, the relative permeabilities k_{rv} and k_{rl} are set equal to the vapor and liquid volume saturations, respectively. Except for variations due to halite deposition or relative permeability effects, the permeability is treated as constant.

CHAPTER 5: CODE BENCHMARKING

To benchmark the new code, the results of a submarine geothermal heat pipe simulation will be compared with previously published results from the code GTHSW [Bai et al., 2003]. Also, to test the coupling between the salinity and pressure equations, the code will be benchmarked against published numerical solutions to the Elder problem [Geiger et al., 2006b; Ackerer et al., 1999; Simpson and Clement, 2003]. The code will then be applied to a single pass system, in which it will be shown that it is able to reproduce the well-known solution to the thermal convection-diffusion equation in the discharge zone, and also that the circulation induced by asymmetric heating from the bottom shows the correct features.

5.1 Code comparisons based on heat pipe simulations

The standard heat pipe reference model based on Bai *et al*. [2003] is shown in Figure 23. For this simulation, the system is 1D and extends to 100 m below the seafloor (mbsf). The mass and salt fluxes at the bottom are set to 0, while the heat flux there is 1 W/m^2. At the top, the pressure is set at 260 bars, while the temperature and salinity values there depend on the direction of fluid flow: if fluid flows out of the system, the temperature and salinity are set to the values just below the surface; if fluid flows into the system, then the temperature and salinity are set to 390°C and 3.2 wt% NaCl, respectively. The initial interior values of temperature and pressure are 390°C and 3.2 wt% NaCl, respectively, with the permeability set to 10^{-15} m^2 and the porosity to 0.1. In this model, a two-phase zone begins growing at the base of the system and reaches the top at approximately 30 yrs. After this event, a vapor rich layer forms at the top and

works its way downward. Meanwhile, a high salinity brine layer grows slowly at the base of the system. At around 150 yrs, the downward progression of the vapor layer is halted by the upward growth of the brine layer at a depth of approximately 40 mbsf. Figure 24 shows the standard reference model computed again with FISHES. Again, a two-phase zone appears at the base and grows upward, reaching the top of the system at about 50 yrs instead of 30 yrs. Again, vapor collects at the top of the system; however, the brine layer is much more distinct this time, forming a well-defined slab at the base of the system. Because the brine collects more completely at the base of the system, it takes longer for the brine layer to reach the downward growing vapor. In fact, after 400 yrs the brine layer has only reached ~90 mbsf, while the rest of the system consists almost completely of pure vapor.

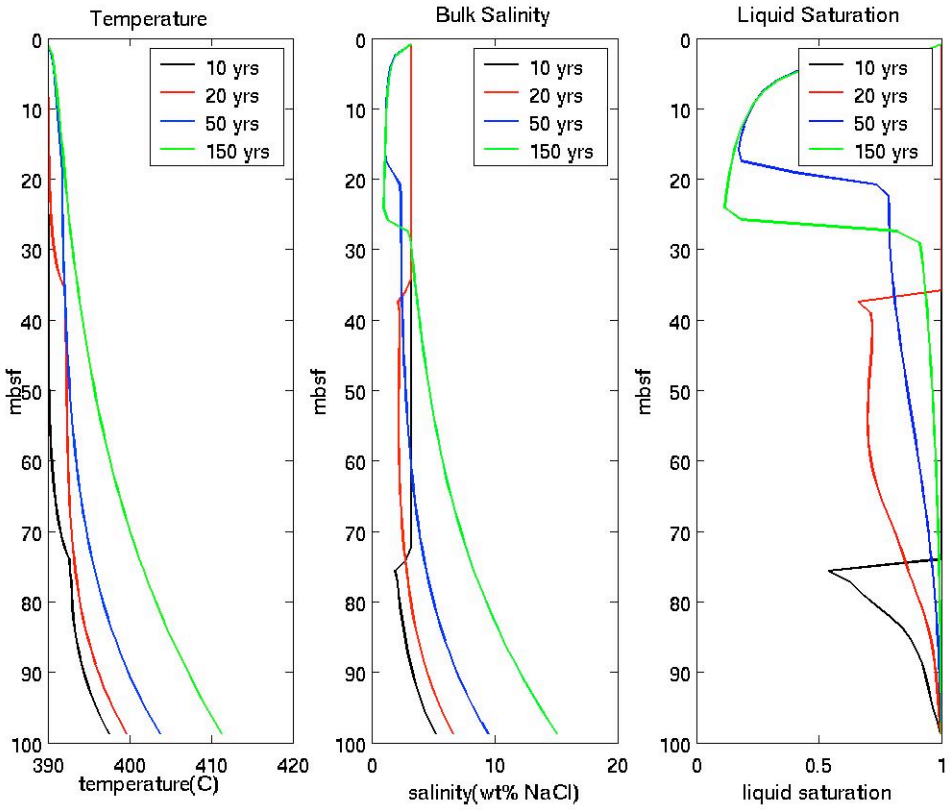

Figure 23 Reference heat pipe model from Bai et al. [2003].

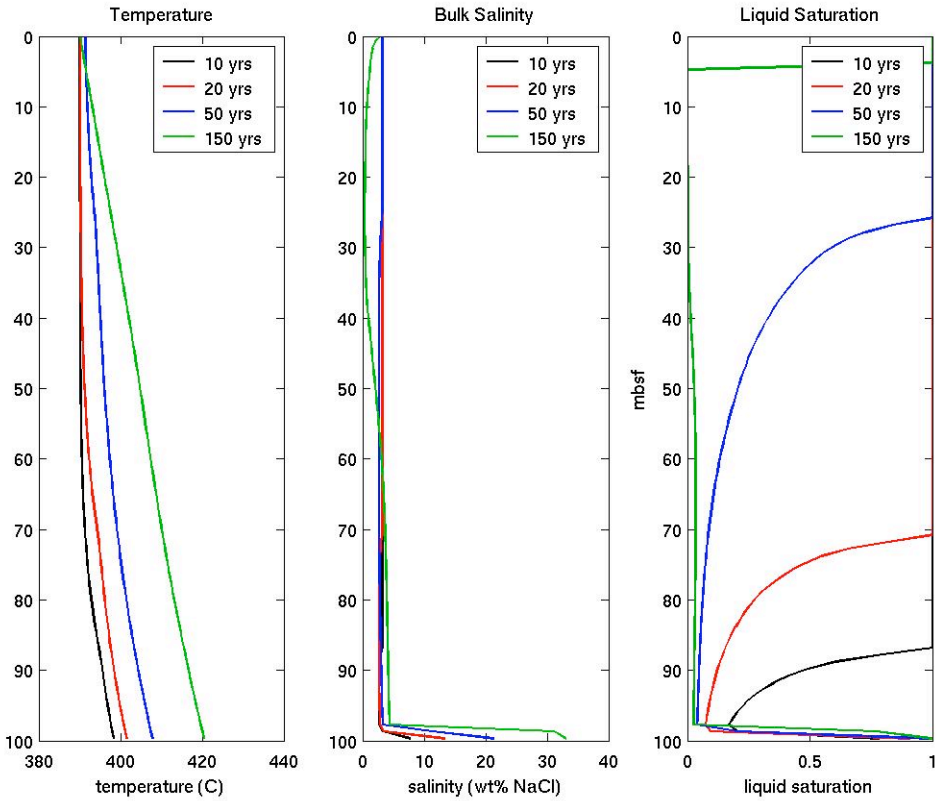

Figure 24 Reference heat pipe model re-computed from FISHES.

The differences between these results can be entirely explained by differences in the equations of state used by FISHES and GTHSW. GTHSW, like NaCl-TOUGH2, uses Palliser and Mckibbin's formulation, and these equations of state yield liquid salinities that are lower than those from the lookup tables of FISHES for a given bulk salinity in a given constant temperature slice of the two-phase region. As a consequence, buoyant forces are stronger in FISHES, causing brine to flow more vigorously downward than in the GTHSW simulation. Also, the two-phase zone takes longer to reach the top in the FISHES simulation because the lookup tables have slightly lower vapor enthalpy values than do the equations of Palliser and Mckibbin for a given *T-P-X* triple in this

region of phase space – the vapor in the two-phase region transfers less heat in FISHES than in GTHSW during a given time period. Finally, even for temperatures significantly higher than the critical point, the bulk densities from Palliser and Mckibbin's formalism meander strangely due to peculiarities caused by the use of interpolation equations between pure water densities and densities on the surface of the two-phase region (see Figures 15 and 19 from the previous chapter). The densities in FISHES show no such variations, and the lack thereof may be partly responsible for the output of FISHES generally appearing to be smoother than that from GTHSW. In addition to the simulations above, an earlier version of FISHES was shown to produce the same output for the heat pipe simulation as GTHSW when both codes were modified to partly contain the equation of state currently used (unpublished results). GTHSW cannot easily (or perhaps at all) be made to implement the full equations of state as currently implemented by FISHES, because the former is written in FORTRAN77, which (as far as I can tell) lacks the ability to implement recursion, while the implementation in FISHES is highly recursive. As a final check, the total mass ejected from the top of the system (which should strictly be zero) was recorded for the original GTHSW heat pipe simulation and compared with that from FISHES. Both were slightly non-zero due to numerical error, with the total ejected mass from FISHES slightly lower than that from GTHSW. Even though the system is mostly filled with vapor at the end of the simulation, the reduced mass in the vapor layer is almost entirely compensated by the increased mass of the dense brine layer.

5.2 The Elder problem

The concentration gradient form of the Elder problem [Elder, 1967] is one of the classic methods for testing the coupling between the pressure equation and the salinity equation in the context of buoyancy driven convection. The geometry and boundary conditions for this problem are shown in Figure 25. At the top of the system is a layer of 100 wt% NaCl fluid, while the bottom boundary is held at 0 wt% NaCl. Halite accumulation, and its attendant clogging of the pore space, is not allowed in this problem. Moreover, to facilitate meaningful comparisons with solutions in the literature, the equation of state relating the density to the salinity is assumed to be

$$\rho = 1000 + 200X \tag{5.1}$$

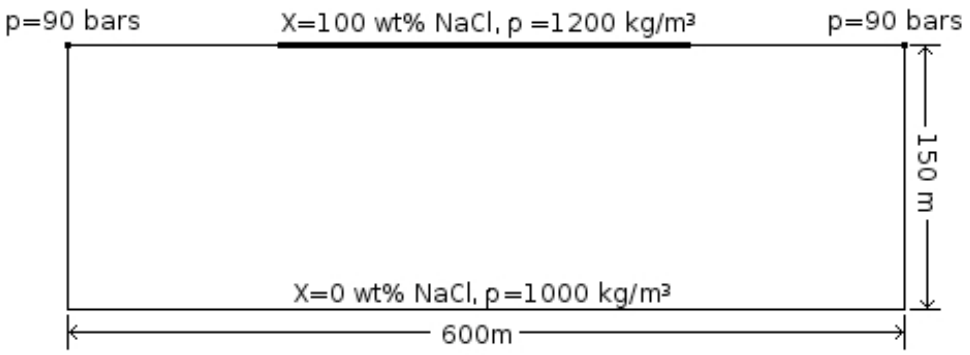

Figure 25 Geometry and boundary conditions for the Elder problem. The pressure is held constant only at the upper left and right corners of the system, where fluid is allowed to pass through.

The simulation results are shown in Figure 26. The solutions display axial symmetry with a central up-flow zone. Initially, there are six down-flow zones, the largest of which are at the left and right edges. These merge into two main down-flow

zones flanking the center. The results are in fair agreement with other results in the literature [e.g., Geiger et al., 2006b; Ackerer et al., 1999; Simpson and Clement, 2003]. The agreement is not complete because, firstly, FISHES is only a first-order accurate scheme, and secondly, the results of the Elder problem are very sensitive to details of the numerical scheme employed, and the grid spacing [Simpson and Clement, 2003]. The number of nodes used in these simulations is 41 x 30 = 1230, with a resolution of about 15 m in the x direction and 5 m in the z direction.

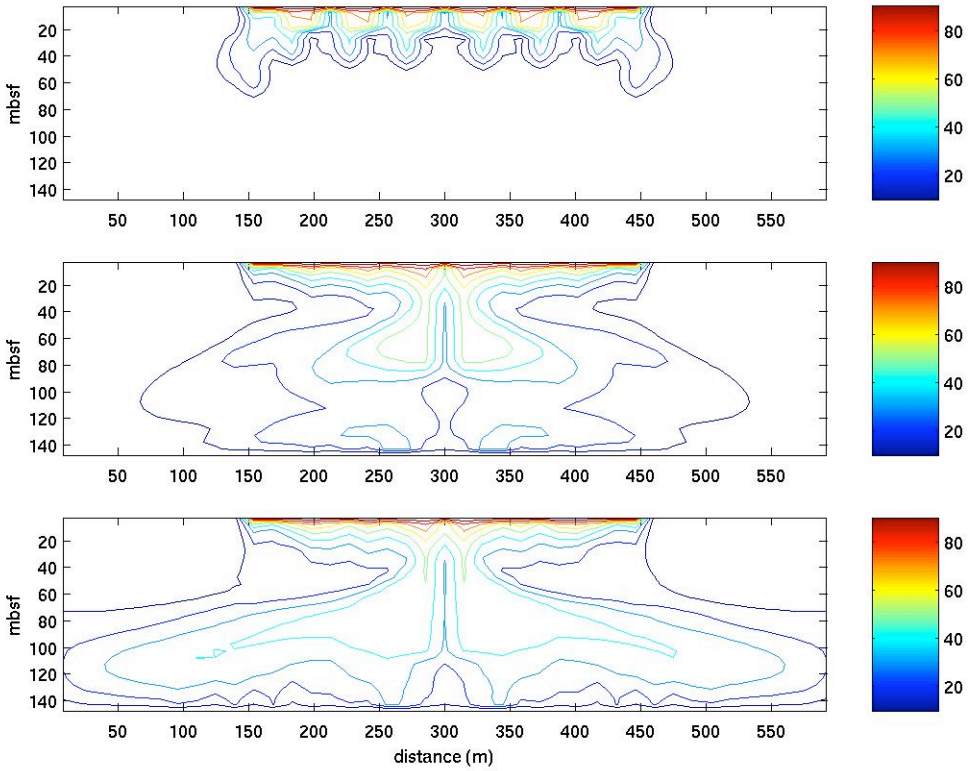

Figure 26 Elder problem simulation results for 2, 10, and 20 yrs, numbered from top to bottom. Colorbars show salinity values on the isochlors in wt% NaCl.

Figure 27 shows results for the same setup except that these simulations employed FISHES's full equation of state to relate the salinity and pressure to one another. The axial symmetry and central up-flow zone remain as before; however, the down-flow zones on the edges are more pronounced, and the central down-flow zones less pronounced, than in the previous simulation. Also, instead of merging into two down-flow regions, now the initial down-flowing regions merge into four zones before finally merging into two. Although the equation of state used is more complex than the one typically used in the literature for this problem, the agreement between code output and the literature solutions is improved in terms of the number and spatio-temperal relationships between the down-flow zones; however, it is important to note that the number of isochlors within the down-flow regions is much less than in the first simulation. Because the density varies only slightly with varying pressure, this difference is most likely attributable to the fact that the density is no longer a linear function of the salinity for the full range of salinities between 0 and 100 wt% NaCl.

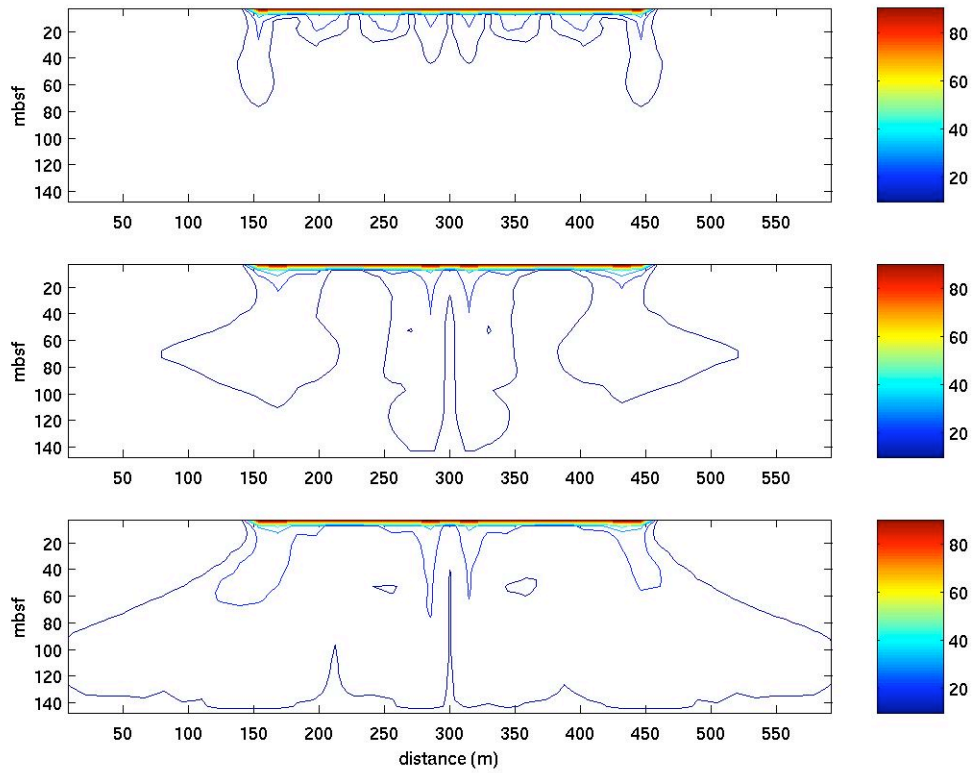

Figure 27 Elder problem simulation results, in which the full equation of state relating p and X was employed.

5.3 Thermal Convection-Diffusion in the Single Pass System

One very useful model for reasoning about seafloor hydrothermal systems is the single pass model (see Lowell and Germanovich [2004] for a review of this model's uses and several interesting results that follow). Because of the usefulness of this approach, for the rest of the simulations considered in this thesis, the system geometry and permeability structure will generally reflect that of the single pass model; this basic geometry is shown in Figure 28. It consists of a discharge zone with a heat source just below it, as well as a cross-flow channel fed by diffuse flow from a relatively wide

recharge zone. The permeabilities and the widths of the zones will be as depicted in the figure unless it is stated otherwise. Also, the permeabilities, even when they are different than depicted, will always be held in the same ratios to one another. For example, if the permeability in the discharge zone is changed to 10^{-15} m^2, then the permeability in the impermeable region will be changed to 10^{-18} m^2. The pressure at the top of the system is 250 bars and increases hydrostatically with depth (~100 bars/km). The temperature is 10°C at the top and increases linearly to 300°C at the bottom. The side boundaries of the system have zero salt, mass, and heat flux conditions imposed, and the bottom boundary has zero salt and mass flux conditions, with a constant temperature condition imposed. The top boundary is held at constant pressure, and upstream weighting is used to adjust the temperatures and salinities there depending on the direction of fluid flow.

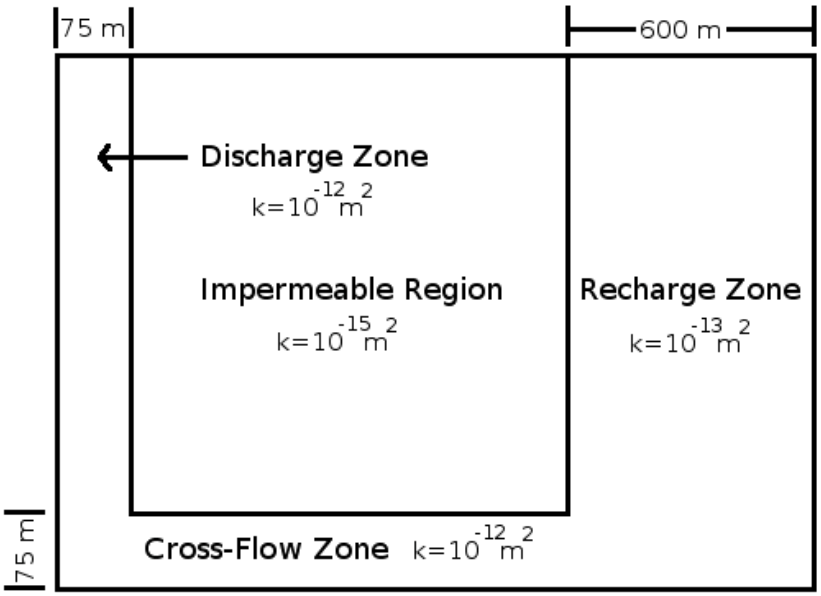

Figure 28 Basic geometry and permeability structure for the single pass model.

To test the coupling between the pressure and temperature equations, fluid temperatures in the discharge zone will be compared with the exact solution of the one-dimensional steady convection-diffusion equation. In order to approximate a one-dimensional scenario in the discharge zone, the width of this zone is shortened to 25 m, and lateral thermal conduction is set to zero. Also, the specific heats in equation (4.5) will be held constant, so that the equation solved by FISHES will be the same as the classical convection-diffusion equation. Finally, in order to increase the width of the steady state boundary layer and facilitate meaningful comparison, the permeability in the discharge zone is set to 10^{-15} m^2. To establish a heat source under the discharge zone, the temperature at the lower right corner is set to 400°C, and decreases linearly toward the left corner to 300°C. The system is then allowed to evolve for ~6000 yrs until steady state is reached.

The resulting isotherms and fluid velocity vectors are shown in Figure 29. The isotherms are depressed in the recharge zone, and deflected upward in the discharge zone, with the velocity vectors showing the clockwise rotational sense expected for this scenario. Figure 30 shows the temperature as a function of depth in the discharge zone (circles) plotted against the exact solution (solid curve). There is strong agreement between these curves.

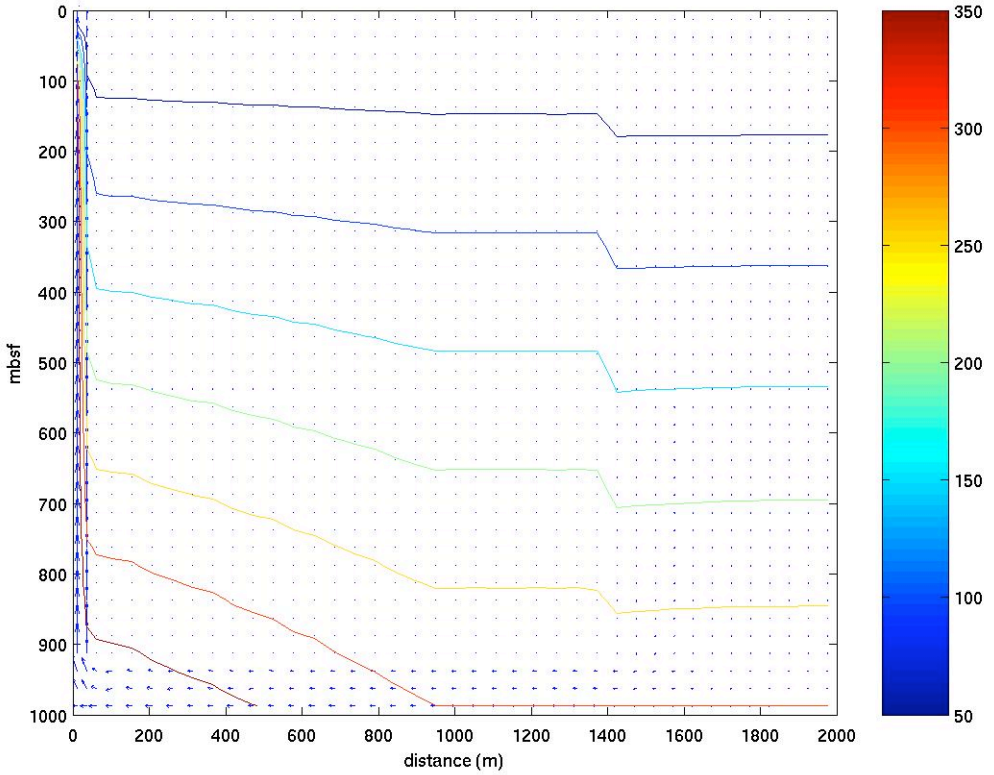

Figure 29 Isotherms and velocity vectors for the steady state scenario, with the bottom temperature held at 400°C on the left, decreasing linearly to 300°C on the right.

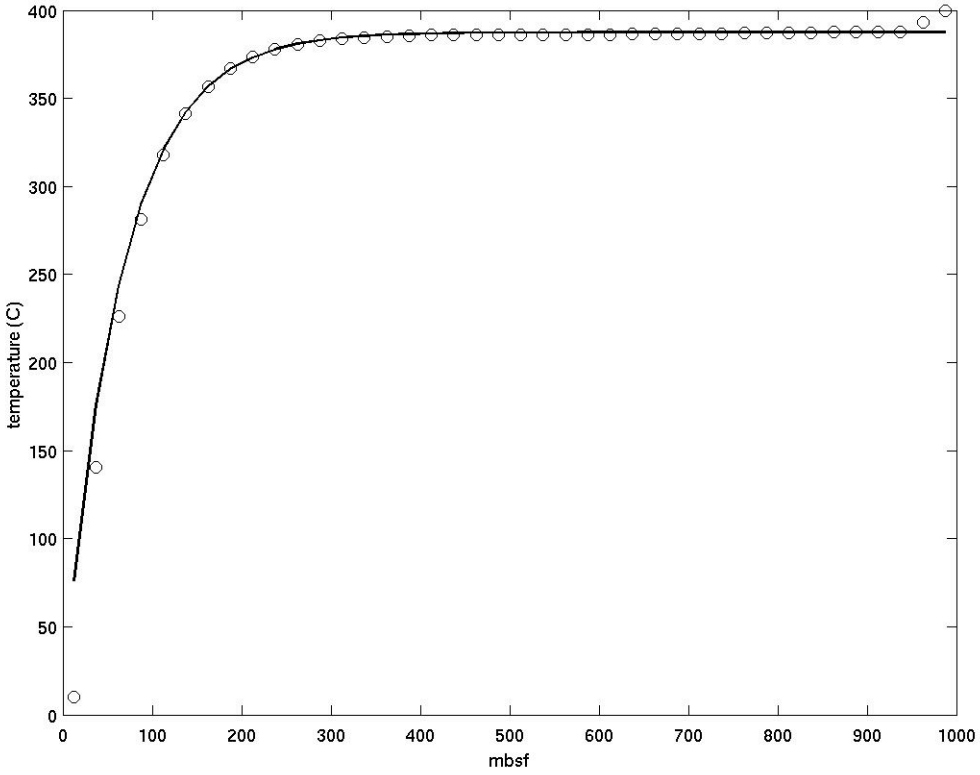

Figure 30 Output temperatures as a function of depth at steady state (circles) plotted against the exact solution to the steady one-dimensional convection-diffusion equation (solid curve).

CHAPTER 6: SINGLE PASS MODEL AND APPLICATIONS TO ENDEAVOUR

Finally, and still in the context of the single pass system, high temperature two-phase simulations will be presented, in which counter-flow of highly saline brine and low salinity vapor occurs. The implications of these results for seafloor hydrothermal systems are discussed. The results will be shown to be consistent with the conceptual model for the temporal evolution of vent fluid salinities outlined in section 3.3.3. Moreover, the results provide a framework from which one can explain the observed vent fluid salinity variations from the Main Endeavour Field on the JDF ridge.

6.1 Quasi-Steady State Two-Phase Zone Simulations

The first simulations will employ the reference single pass model described in section 5.3 and depicted in Figure 28. The bottom boundary is set at temporally constant temperatures starting at 390°C on the discharge zone side and linearly decreasing to 300°C on the recharge side. At the initial pressures, temperatures, and salinities described above, there is no boiling. The system is allowed to evolve until it has approximately reached steady state, after which the temperature at the bottom of the system is raised to vary linearly from 420°C on the left to 300°C on the right. This specific maximum temperature was chosen to be the lowest temperature that would induce boiling at the bottom of the system. The reason for choosing such a temperature is to minimize the numerical instability introduced into the system as a result of suddenly raising the temperature in the lower left corner. Once the two-phase zone has developed, the temperature can be raised to any desired value incrementally; however, for the purposes of the simulations that follow, raising the temperature significantly (i.e., >10°C) above

the boiling temperature will not be necessary. After the temperatures have been raised high enough on the discharge side to result in a zone of two-phase fluid near the bottom left-hand corner, the system is allowed to evolve this way for 10 yrs, during which highly saline brine collects on the bottom and low salinity vapor collects at the top of the two-phase zone, respectively. Figure 31 shows isotherms along with the directions and relative magnitudes of the liquid velocity vectors at the end of this 10 yr period. For all the simulations of this chapter, the global fluid flow pattern will closely resemble that of Figure 31, so that it will not be necessary to show a global plot for each individual simulation. Figure 32 shows the lower left-hand of the system expanded, and includes a box showing the approximate extent of the two-phase region. This two-phase region develops quickly (<< 1 yr) after the start of the simulation, and remains constant in extent for the entire 10 yrs of simulation time. Figure 33 shows the boxed region expanded and overlain with isochlors instead of isotherms. Note that fluid passing from the cross-flow zone into the discharge zone induces a counterclockwise eddy in the lower left corner of the system. Partly because of this eddy, and partly because the vapor collects above the brine in the two-phase region, brine becomes “locked” into the system as long as there is active phase separation. The vapor phase fluid, however, dilutes the fluid above the two-phase zone, resulting in a stream of lower-than-seawater salinity fluid flowing toward the top of the system. Also, because brine collects at the bottom of the system, the salinity values there represent mixtures of normal seawater salinity fluid with high salinity fluid, as opposed to the values that would be expected from thermal equilibrium considerations alone. Figure 34 shows the surface vent fluid salinities and temperatures for this system over the total 10 yrs of simulation time. Fluid salinity at the top of the system decreases

rapidly when the initial pulse of low salinity fluid reaches the top boundary, and then increases somewhat, maintaining a roughly constant value for the rest of the simulation; meanwhile, the temperature rapidly increases and maintains a constant value thereafter.

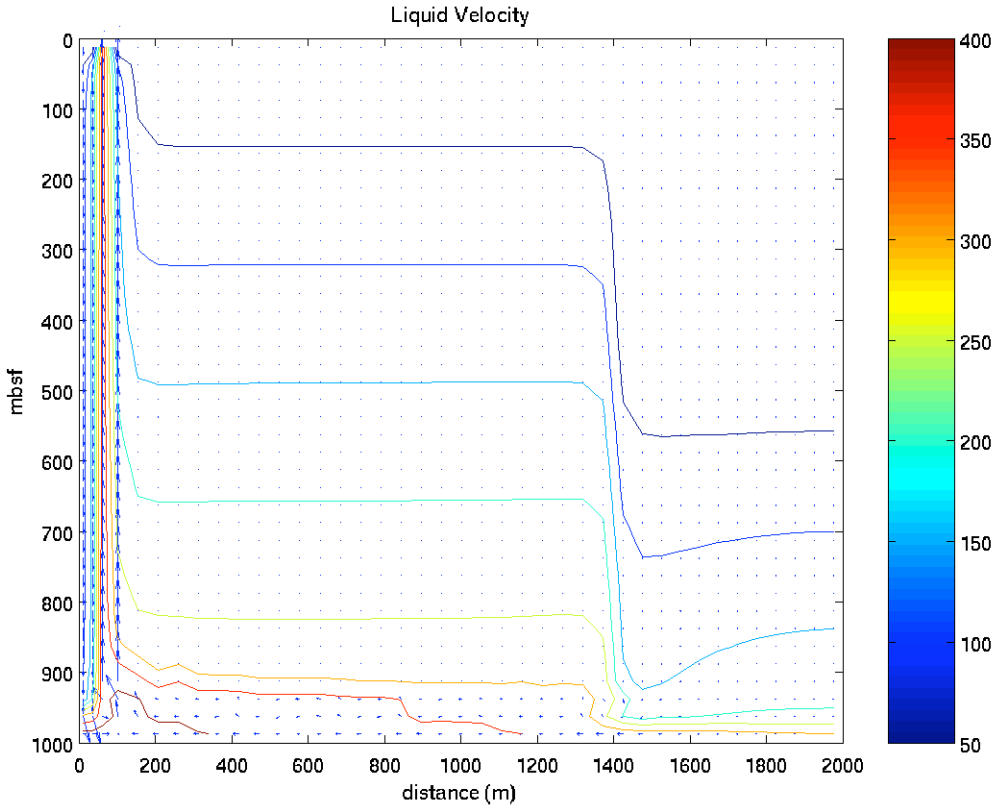

Figure 31 Isotherms and relative fluid velocities for the reference single pass model with a two-phase zone at the lower left corner after 10 yrs of simulation time.

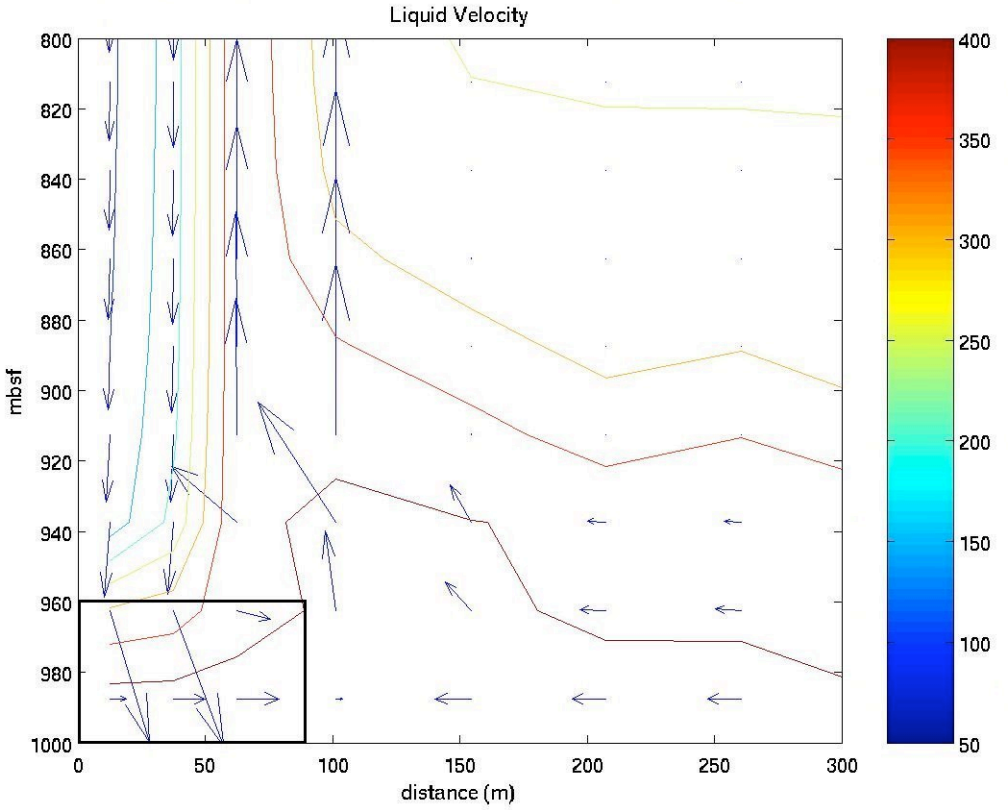

Figure 32 Liquid velocity vectors and isotherms (in °C) after 10 yrs of simulation time. The boxed region shows the approximate location of fluid in the two-phase regime.

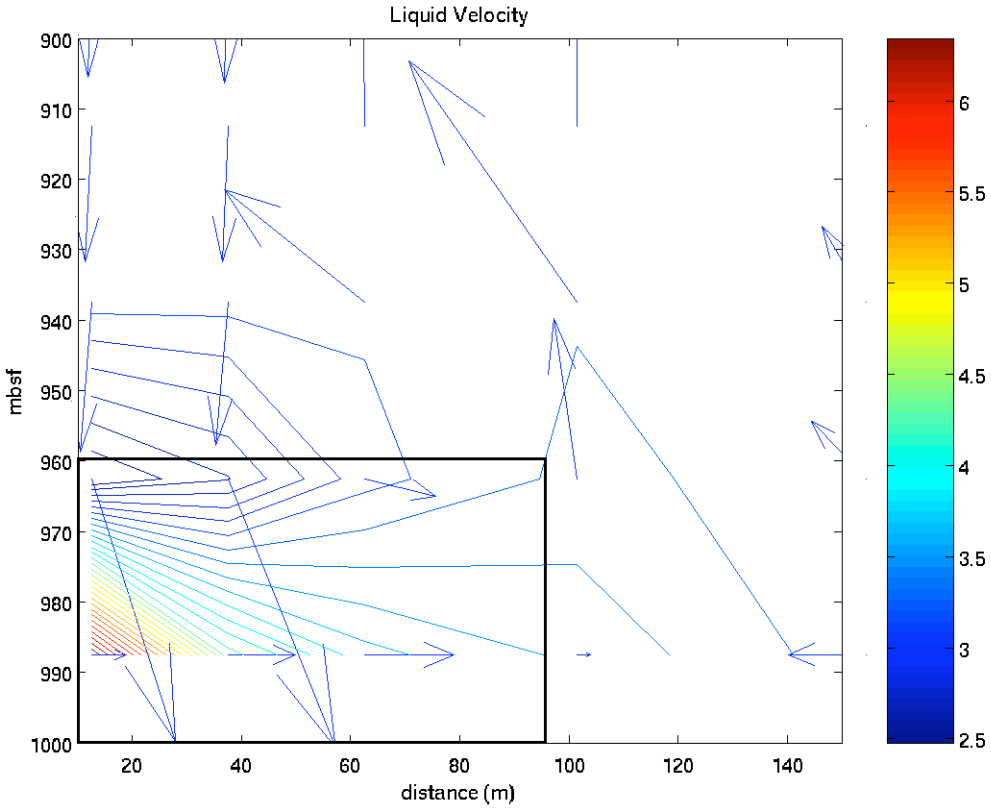

Figure 33 Expanded lower left corner of Figure 31, with isotherms replaced by isochlors (in wt% NaCl). Isochlors not extending all the way to 1000 mbsf is a plot artifact.

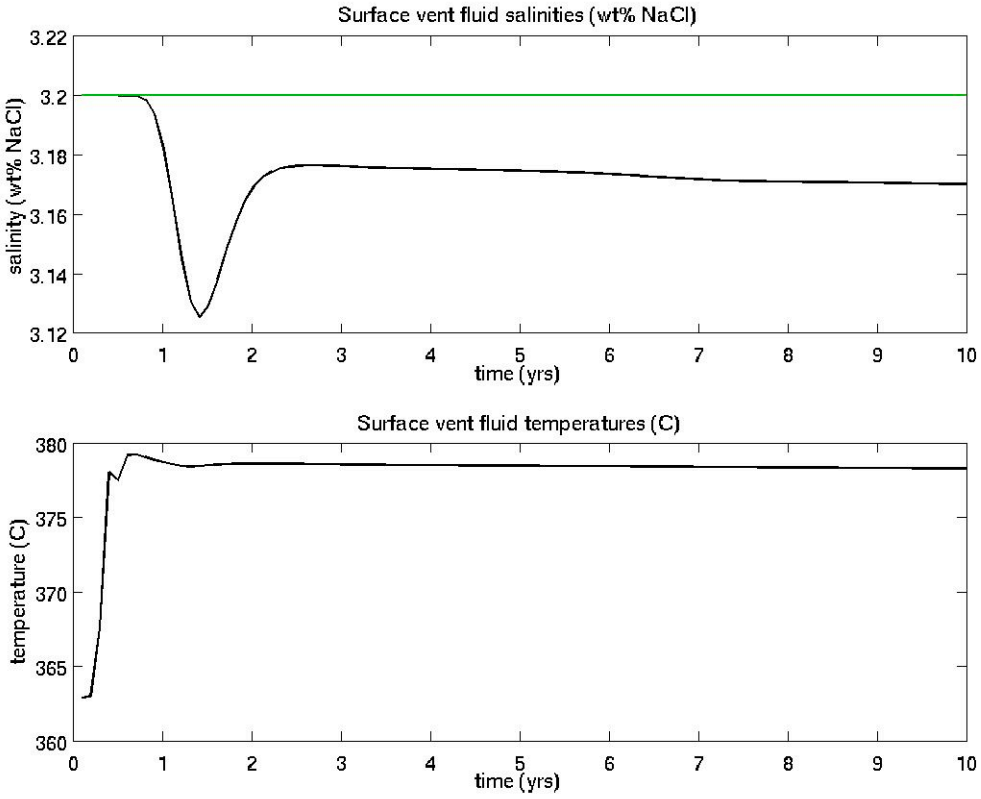

Figure 34 Surface vent fluid salinities and temperatures vs. time. The green line in the top figure represents ordinary seawater salinity.

It should be noted that there is a fluid down-flow region in the discharge zone extending from the top to nearly the base of the system. This down-flow region results because of the necessity of maintaining a global mass balance for the system – not enough fluid passes down through the recharge zone to replace fluid leaving from the discharge zone. The strength of the downward flow in the discharge zone thus depends on the width of the recharge zone and on how high the temperature contrast is at the base of the system from the right-hand-side to the left. Increasing the width of the recharge zone, decreasing the lateral temperature gradient at the bottom boundary, and starting the

system with a high temperature perturbation in the discharge zone can significantly weaken or eliminate this down-flow zone; however, it can be difficult in practice to both eliminate the down-flow zone and study the effects of varying various parameters such as the permeability and temperature boundary values for the system. Hence, the down-flow effect in the discharge zone will be tolerated in the present study. Although the down-flow zone contributes to the strength of the counterclockwise eddy in the lower left corner, it is primarily the effect of the vapor phase on the relative permeability, along with the brine phase's high density, that results in the sequestering of the highest salinity fluid at the bottom of the system; therefore, removal or weakening of the downward flowing zone is not likely to have a large affect on the salinities of venting fluids.

If one re-plots Figure 31 with logarithmically scaled velocities, as in Figure 35 below, another interesting effect becomes apparent. Fluid in the cross-flow region forms a wave pattern as it travels from the right corner toward the left corner of the system. This behavior results from the fact that the Rayleigh number, calculated using the height of the cross-flow region as the relevant length scale, is much greater than the critical value required for the onset of vertical convection there. The fluid flows upward as it travels from left to right and, because there is a boundary impeding it's upward progress, adjacent fluid is forced downward to maintain mass balance; hence, a wavelike pattern is created. The wavelength of this pattern is dependent on the both the lateral and vertical temperature gradients, but in general, the stronger the lateral gradient, the shorter the wavelength.

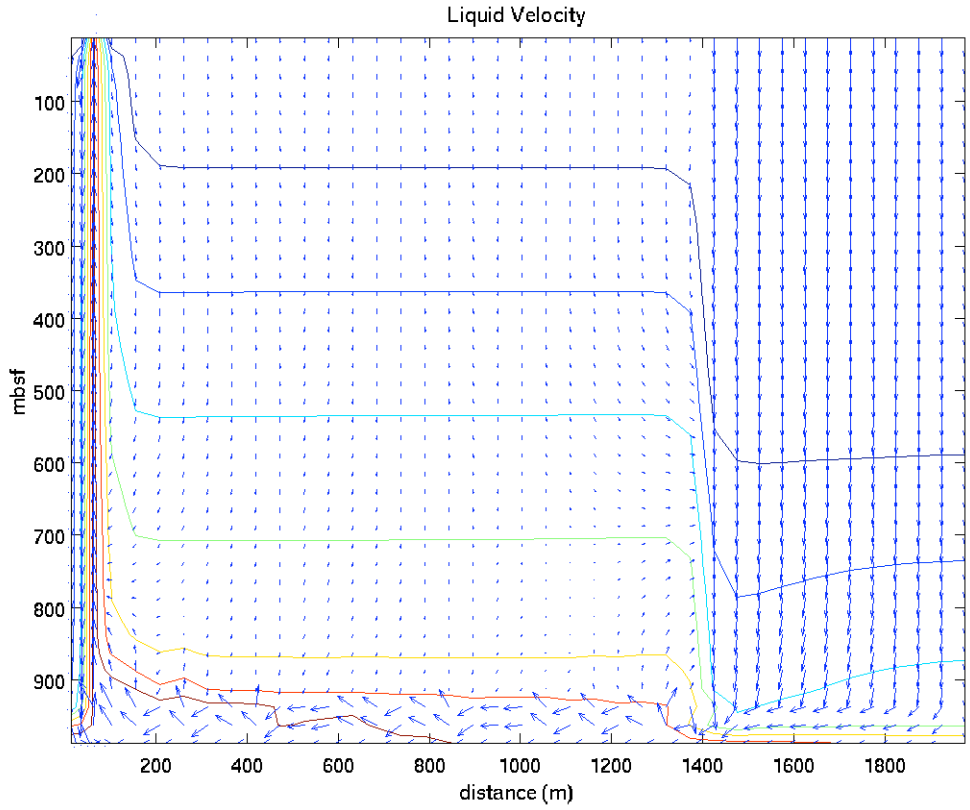

Figure 35 Re-plot of Figure 31 with logarithmically scaled velocity vectors. A wavelike pattern becomes evident in the cross-flow region.

To investigate the effects of higher temperatures on vent fluid properties, the simulation described above is repeated, except that when the temperature at the bottom boundary is raised above the boiling point, it is now made to vary linearly from 430°C on the left to 300°C on the right. The resulting vent fluid salinities and temperatures are shown in Figure 36. The overall pattern of temperature and salinity variation is very similar to that in Figure 34, except that now the salinity difference is more marked, reaching salinities below 2.8 wt% NaCl. These lower salinities are primarily due to the fact that increasing the temperature in the lower left corner creates a more extensive two-

phase region along the bottom; hence, more brine and vapor are created than for lower temperatures.

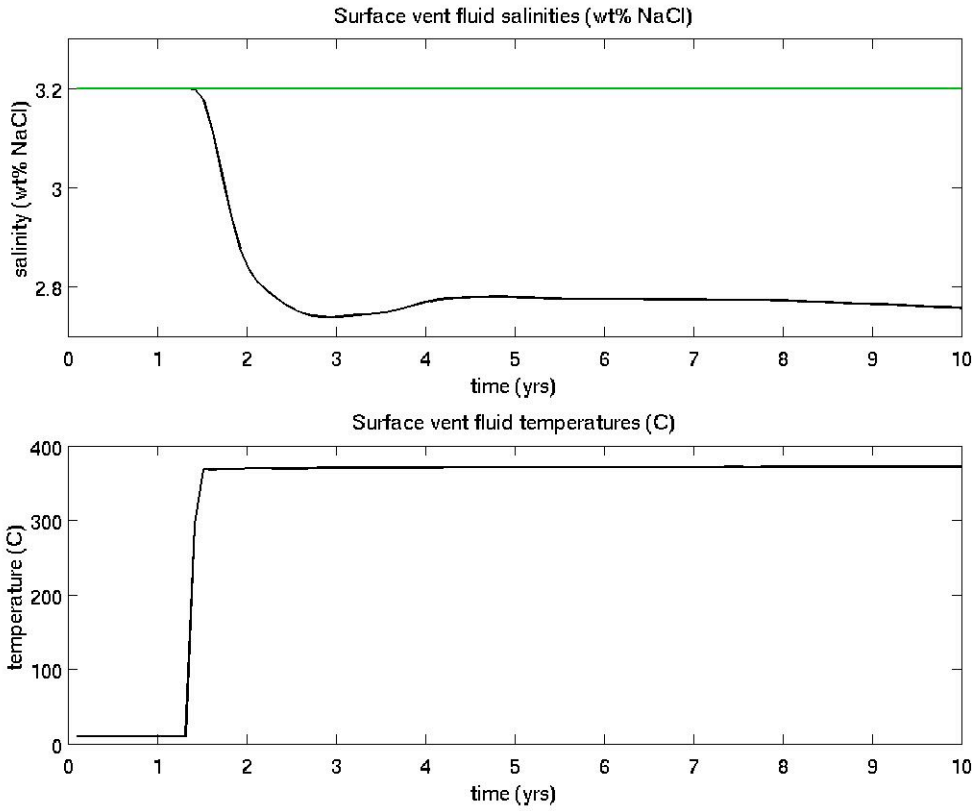

Figure 36 Surface vent fluid salinities and temperatures resulting from increasing the temperature at the bottom left corner relative to the simulation depicted in figure 34.

To show that increasing the extent of the two-phase region alone can result in large contrasts in surface vent salinities, the simulation is repeated with a maximum bottom boundary temperature of 420°C, but with the temperature remaining this high for ~600 m away from the left boundary until dropping off linearly to 300°C at the right corner of the system. In this way, the extent of the two-phase zone is increased without

raising its average temperature. Figure 37 shows the directions and relative magnitudes of the liquid velocities at the bottom left corner of the system along with the isochlors after 10 yrs of simulation, and Figure 38 shows the surface vent fluid salinities and temperatures as functions of time. Similar to the previous high temperature simulation, the vent fluid salinities level off around 2.7 wt% NaCl; however, the vent fluid temperatures are lower and show a different initial shape than that in Figure 36 – after rising steeply, the temperatures drop just as steeply before rising again to the quasi-steady state value of ~375°C. The temperatures rebound in this way because cool water from the recharge zone side of the cross-flow zone was entrained in the initial hot fluid plume as it moved from above the two-phase region toward the discharge outlet, due to the large initial difference in fluid buoyancy created by rapidly increasing the bottom boundary temperatures. Figure 36 does not show this rebound feature in the temperatures, mostly likely because the bottom temperatures vary linearly all the way to the left boundary, which tends to offset sudden increases in buoyancy from rapidly increasing the strength of the heat source.

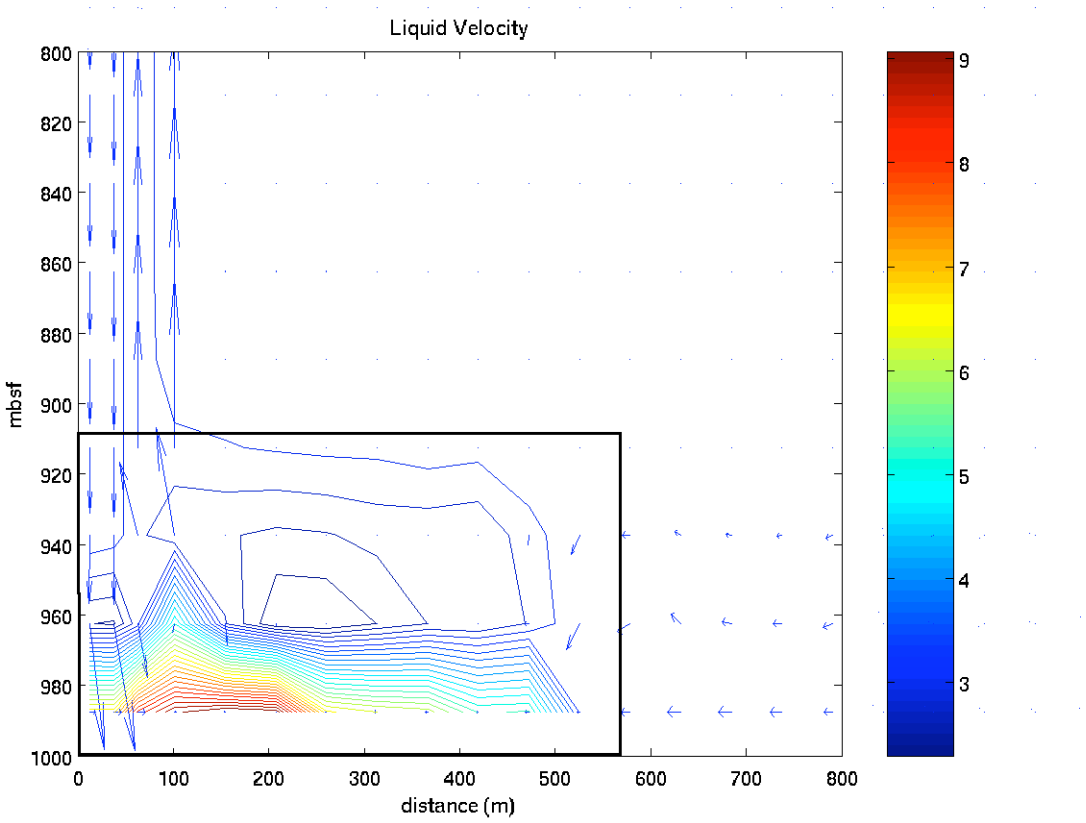

Figure 37 Directions and relative magnitudes of the liquid velocities, with isochlors (in wt% NaCl) at the bottom of the system. The two-phase region has been extended without raising its average temperature above 420°C. The box shows the approximate extent of the two-phase region.

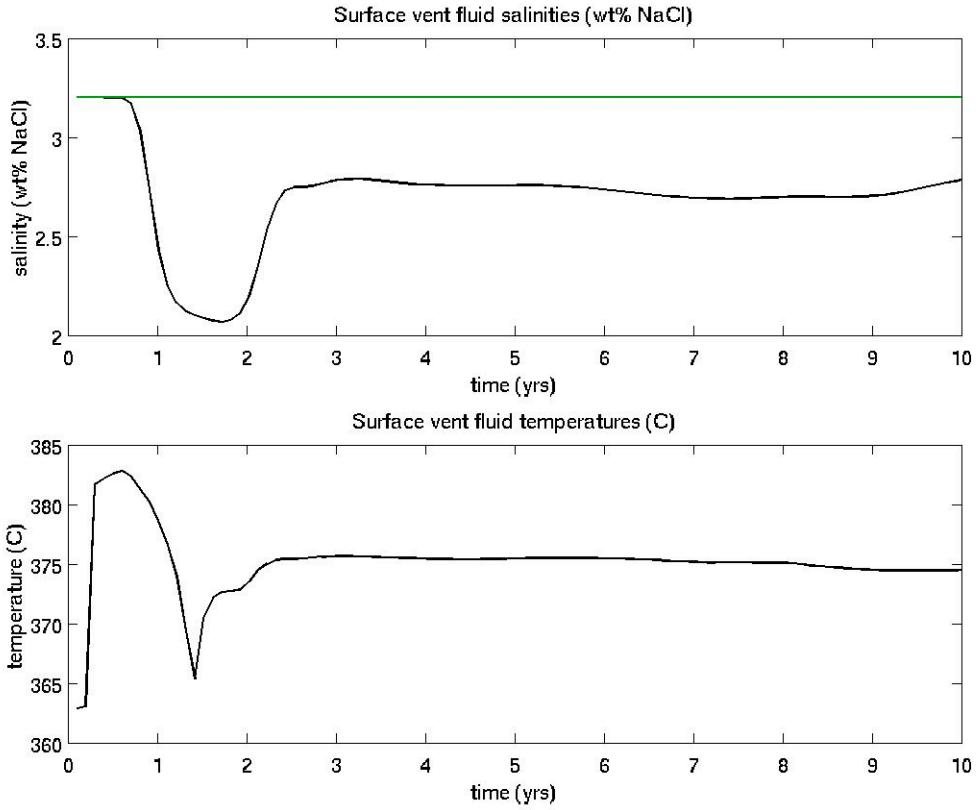

Figure 38 Surface vent fluid salinities and temperatures vs. time when the two-phase zone is extended without raising the bottom temperature above 420°C.

6.2 Simulations Such That The Brine Is Flushed From the System

In the simulations above, the fluids with the highest salinities are trapped in the system because they are located in the corner of the system, behind a strong eddy; because vapor surrounds the brine from above, leading to low relative permeabilities for liquid phase fluids in the upper half of the two-phase region; and finally because the brine is denser than the surrounding fluid. In order to release the brine from the system, simulations are performed such that there is an initial two-phase zone followed by several years of purely single-phase circulation. In the first of these simulations, the reference single pass system is employed, with the bottom boundary temperatures linearly

decreasing from 420°C on the right to 300°C on the left. After 3 years, the temperature on the bottom boundary is lowered so that it varies linearly from 390°C to 300°C (the pre-two-phase flow values as described in section 6.1). The system is then allowed to evolve for 10 yrs. Figure 39 shows the surface vent fluid temperatures and salinities for the entire simulation, including the initial two-phase zone stage. The fluid salinity drops below seawater values as the temperature rises, similar to the simulations of last section, but now as the brine is flushed from the system and the temperature decreases, the vent fluid salinities increase steeply, reaching a peak before decreasing rapidly to normal seawater values.

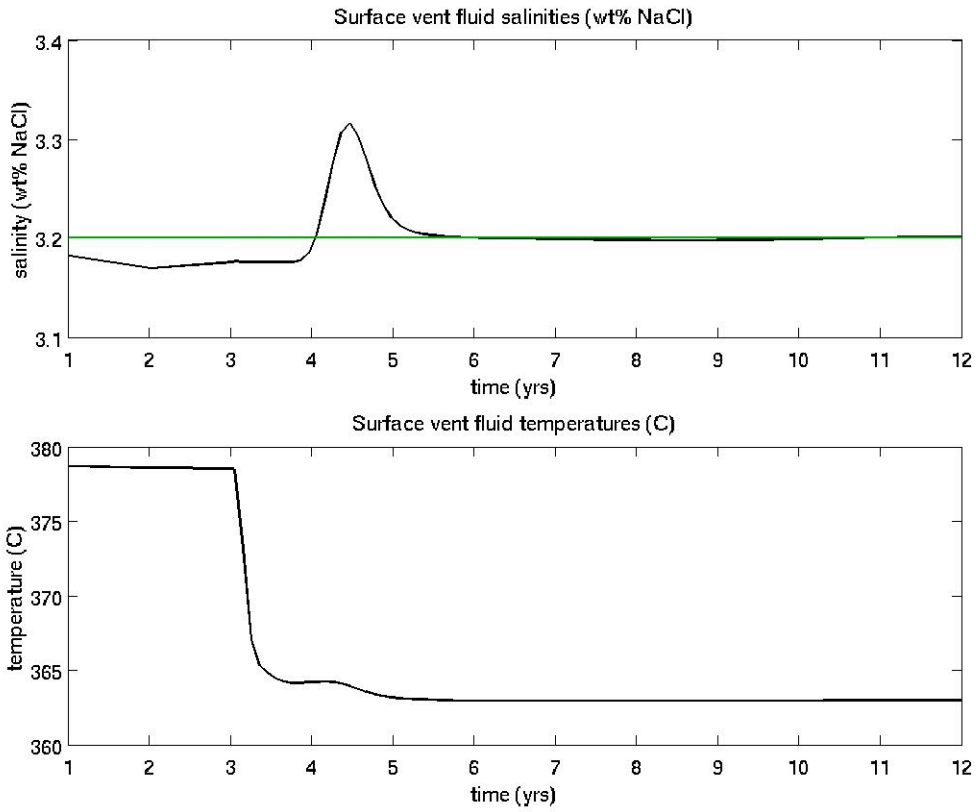

Figure 39 Vent fluid temperatures and salinities corresponding to an initial two-phase simulation (first 3 yrs) followed by purely single-phase flow in which brine is flushed from deep within the system.

In order to quantify the effects of varying the permeability, the above simulations were repeated with permeabilities in the discharge zone set to 10^{-13} m^2 and 10^{-14} m^2. In order to provide enough time for brine to be flushed from the lower permeability systems, the simulation times are increased by factors of 10 – the initial two-phase zone phase lasts 30 yrs for the 10^{-13} m^2 discharge zone permeability system, and 300 yrs for the 10^{-14} m^2 system. The lifetimes of the purely single-phase flow parts are increased by the same corresponding factors of 10. The resulting vent fluid properties from these simulations are shown in Figures 40 and 41, respectively. The peaks in fluid salinity occur at ~58 yrs and ~1200 yrs when the discharge zone permeabilities are 10^{-13} m^2 and 10^{-14} m^2, respectively. Compare with the peak at ~4.5 years when the discharge zone permeability is 10^{-12} m^2, as in the first simulation of this section. The peaks occur later in time for lower permeabilities than one might expect for a simple linear relationship; also, the time variations in surface temperatures and salinities are more complicated than for the reference permeability case.

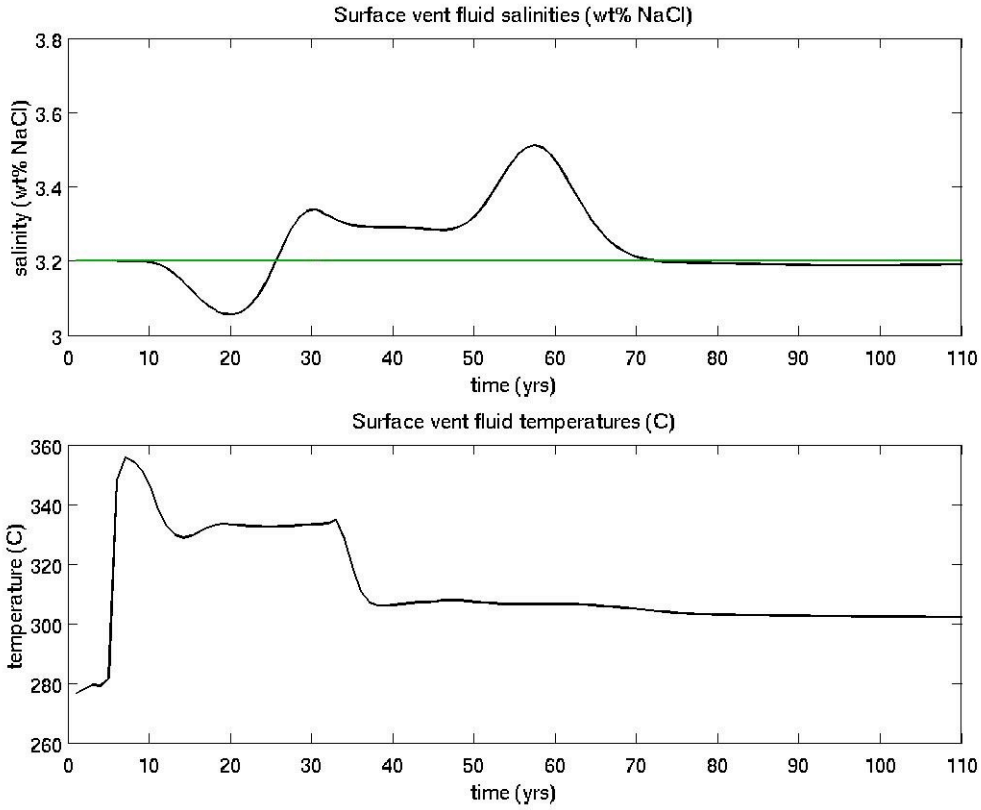

Figure 40 Surface vent fluid salinities and temperatures when the discharge zone permeability is set to 10^{-13} m^2, and the simulation times are extended by a factor of 10; hence, the initial two-phase zone lasts for the first 30 yrs instead of the first 3 yrs.

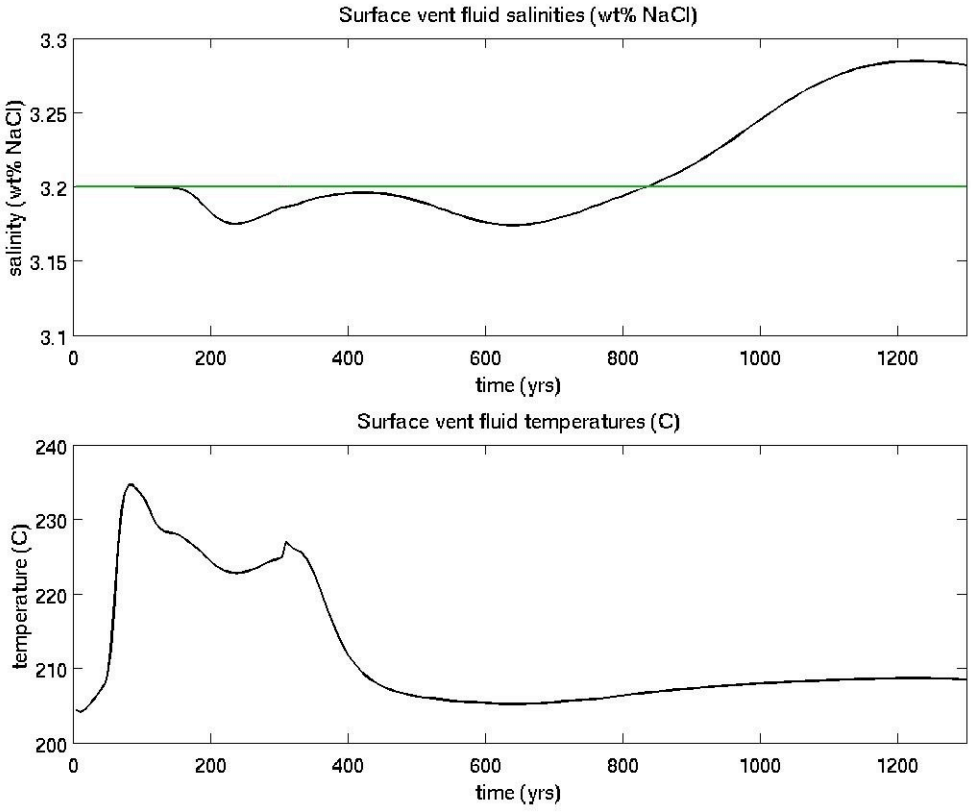

Figure 41 Surface vent fluid salinities and temperatures when the discharge zone permeability is set to 10^{-14} m^2, and the simulation times are extended by a factor of 100; hence, the initial two-phase zone lasts for the first 300 yrs instead of the first 3 yrs.

6.3 Implications for Seafloor Hydrothermal Systems

It has been shown in previous sections that the existence of two-phase fluids at depth gives rise to lower than seawater salinities at the surface discharge outlet, with the contrast increasing with increasing extent of the subsurface two-phase zone. Furthermore, if the bottom boundary temperature drops below the boiling point, the two-phase zone vanishes, freeing a layer of brine at the base of the system and leading to the venting of fluids with higher than seawater salinities at the seafloor. Such a pattern conforms to the conceptual model for vent fluid salinity variation outlined in section 3.3.3. Because the

timescale over which such a pattern manifests itself is roughly inversely proportional to the permeability, and because its amplitude is proportional to the extent of the subsurface two-phase zone, this pattern can likely be adjusted to fit the temporal vent fluid salinity profiles from some actual systems. For instance, the vents from 9-10°N EPR such as "F", "A", "P", Bio9, and Bio9' all manifest either partly or completely the qualitative pattern described by the conceptual model; hence, these may be amenable to numerical modeling employing the single pass model with two-phase fluids at depth.

6.3.1 Main Endeavour vent field

The hydrothermal systems at the Main Endeavour Field on the JDF ridge furnish another example of systems whose vent fluids may be exemplifying part of the pattern described by the conceptual model of vent fluid salinity variation. Each of these systems has been venting fluids below seawater salinity for a number of years; furthermore, there is a distinct spatial variation in vent fluid salinity among these systems. The vent salinity increases from the southwest to the northeast (Figure 42). Although Figure 42 only shows the vent salinities for 1988, roughly the same relative pattern of vent salinities is seen to hold during all the years for which there are data at the Main Endeavour Field (Figure 1). Also, with the exception of the aftermath of the 1999 magmatic event (see below), the vent fluid temperatures at the Main Endeavour Field have been temporally stable. The systematic vent fluid salinity pattern at Endeavour could possibly be explained if all the vents are fed by a single magmatic heat source, with the conductive boundary layer increasing in thickness from the southwest to the northeast. A thickening conductive boundary layer would result in two-phase zones that decrease in extent from the southwest to the northeast; in turn, this distribution of two-phase zone extent could give

rise to the observed spatial gradient in vent fluid salinity. Seismic reflection data indicates that the magma chamber does not have a significant along axis tilt [Van Ark et al., 2007], but this does not necessarily preclude the existence of a conductive boundary layer of variable thickness. Although the magma chamber displays a varying cross-axis tilt (between 8° and 36° across the entire Endeavour segment) [ibid.], this tilt is expected to give rise to at most slight variations in the *T-P-X* conditions of phase separation for each vent at the Main Endeavour Field. In 1999, there was a swarm of seismic activity at the Main Endeavour Field [Seyfried et al., 2003], which was later determined to be magmatic in origin [Seewald et al., 2003; Lilley et al., 2003]. A marked drop in the salinities of venting fluids immediately followed this recharge event; in the course of a few years, the vent fluid salinities began returning toward their pre-1999 values (Figure 1). Interpreted from the point of view of the single pass model, magmatic recharge at the base of the system could increase the extent of the two-phase zone beneath each vent, and if such an increase were uniform, it could give rise to all the venting fluids having lowered salinity, but still maintaining the appropriate vent-to-vent spatial relationship with each other. Results from magnetic studies suggest that fluids at the Main Endeavour Field are venting from focused channels not unlike the discharge zones envisioned in the single pass model [Tivey and Johnson, 2002].

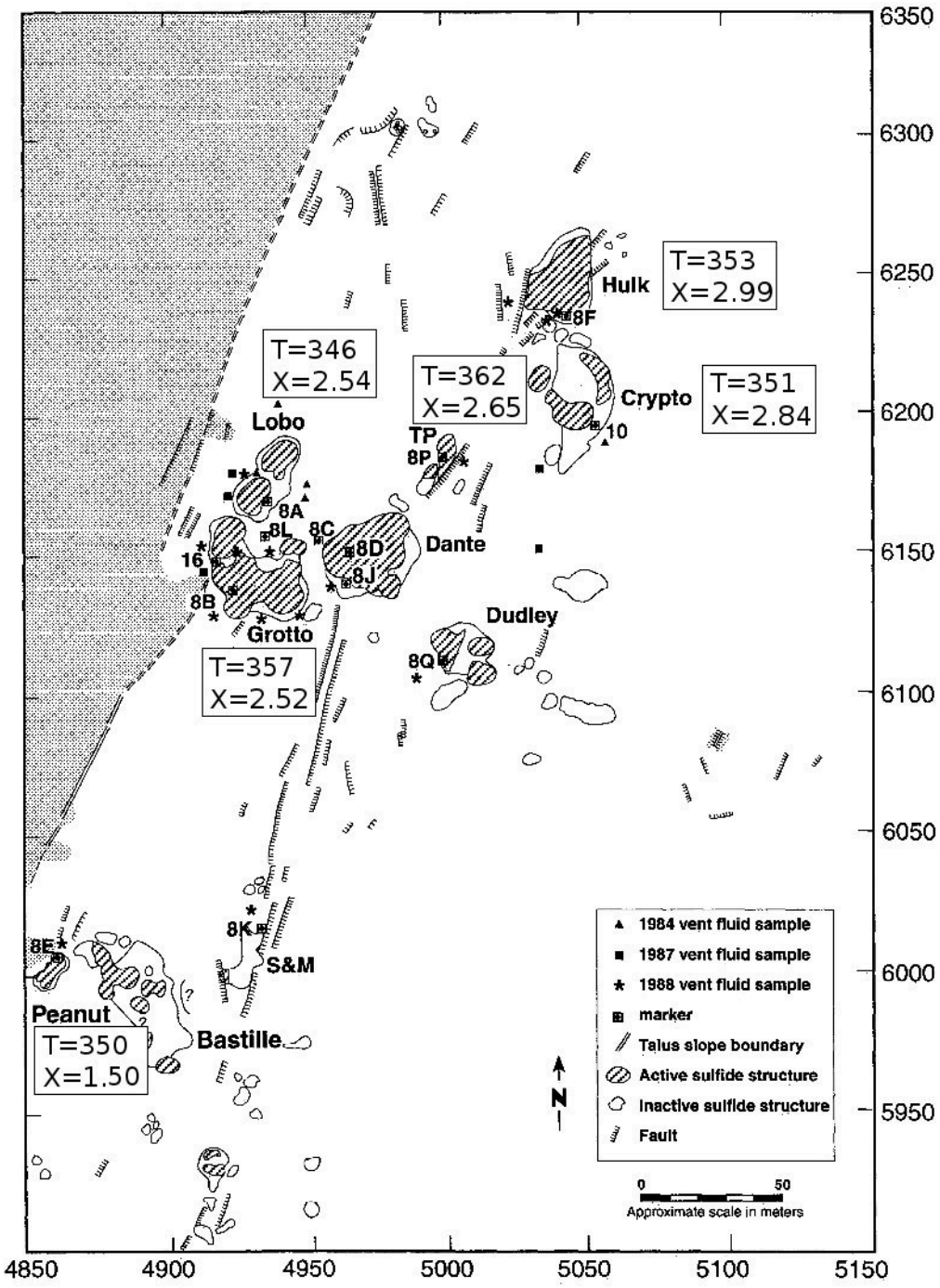

Figure 42 Map of the Main Endeavour Vent Field, showing selected temperatures (°C) and salinities (wt% NaCl) sampled in 1988. Each boxed figure refers to the vent whose name is closest to that box. This figure is adapted from Butterfield et al. [1994].

In order to determine if the single pass systems explored in this chapter have the essential features required to explain vent fluid salinities at the Main Endeavour Field, an initial-two-phase-zone/brine-flushing simulation is conducted with a single pass system set up to be roughly consistent with known geological constraints at the Main Endeavour Field [see Butterfield et al., 1994; Van Ark et al., 2007]. The pressure at the top of the system is set at 220 bars (instead of 250 bars), and the system depth is extended to 2 km (instead of 1km). Also, even though there is an extrusive layer of approximately 460 m thickness overlaying the Main Endeavour Field [Van Ark et al., 2007], precipitation of permeability sealing species such as anhydrite are likely to effectively eliminate the extrusive layer immediately adjacent to active venting sites [Lowell et al., 2003, 2007]. Hence, no extrusive layer will be included in the following simulations. The permeability structure is the same as in the reference model depicted in Figure 28, whereas the width of the discharge and cross-flow regions is slightly decreased to 70 m. The total number of nodes for the previous simulations was 1600 nodes, and this number is increased to 2400 nodes for the following simulation. In both the previous and the present case, the node spacing is non-uniform, with the greatest resolution in the left part of cross-flow zone and the entire discharge zone. Because the distance to the seafloor is 1 km further than in the previous simulations, the dynamics of temperatures and salinities at the surface could be considerably altered. In order to mitigate somewhat the expected increased dilution of the discharge zone fluid due to mixing, the two-phase region at the base of the system is of the extended type, i.e., the temperature of the bottom boundary begins to drop some distance away from the left-hand boundary - similar to that of the system depicted in Figure 37. For the first simulation the maximum temperature is set to 480°C for up to ~60

m away from the left boundary, decreasing linearly to 300°C at the right boundary. Note that temperatures higher than the reference value of 420°C were chosen in order to be near the two-phase boundary, which occurs at higher temperatures for pressures near 420 bars, as opposed to those near 350 bars, such as in the simulations from last section. A region of two-phase fluid above the bottom boundary, with a temperature distribution described above, is set up at the left-hand corner of the system, and the system is allowed to evolve for 30 yrs. The results are shown in Figures 43, 44, and 45. As can be seen in Figure 43, there is a counterclockwise eddy where fluid transitions from the cross-flow to the discharge zone extending from 1600 m to the bottom of the system. Cool downward flowing fluid feeds this corner circulation, resulting in a diminished two-phase region at the left corner as can be seen in Figure 44. As in the previous simulations, fluid in the two-phase region tends to separate into downward flowing brine and upward flowing vapor, resulting in low salinity fluids that rise toward the top of the system. As brine settles out of the bottom of the two-phase zone near the left hand corner, however, it falls into the counter clockwise eddy of single-phase fluid and mixes with it. Some of the upward moving fluid originates from the circulating eddy fluid, resulting in slightly higher salinity fluid rising toward the top of the system in a narrow conduit immediately to the left of the upward flowing low salinity fluid (see Figures 43 and 44). Because this higher salinity fluid is denser than the low salinity fluid, it ascends more slowly through the upflow limb. Consequently, higher than seawater vent fluid salinities do not arrive at the seafloor during the course of the 30 year simulation (see Figure 45). Figures 43 and 44 are both taken at the 30^{th} year of simulation time. Also plotted in Figure 45 are measured vent fluid salinities and temperatures from Dante vent at the Main Endeavor

Field from the years 1988, 1991, and 1995. The vent fluid salinities nearly match, although there is a greater discrepancy between the simulated and observed temperatures.

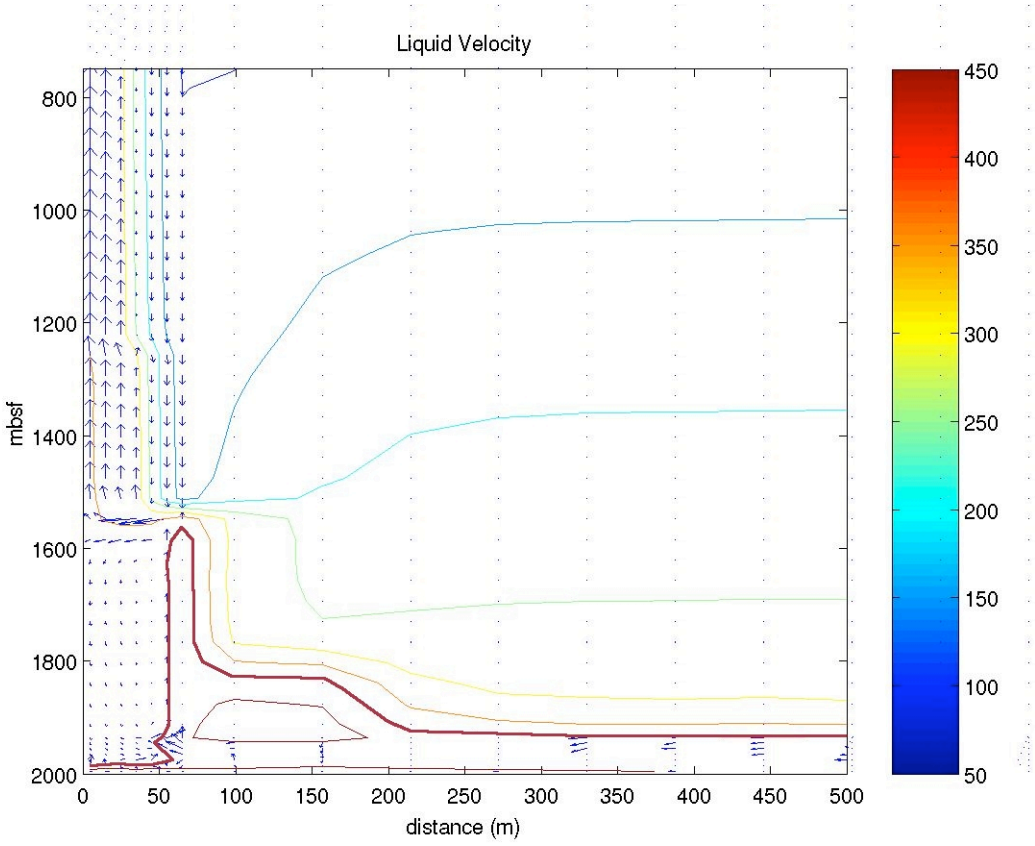

Figure 43 Velocity vectors (shown in relative magnitudes) and isotherms at the intersection of the discharge and cross-flow zones. The two-phase boundary corresponds roughly to the bolded isotherm.

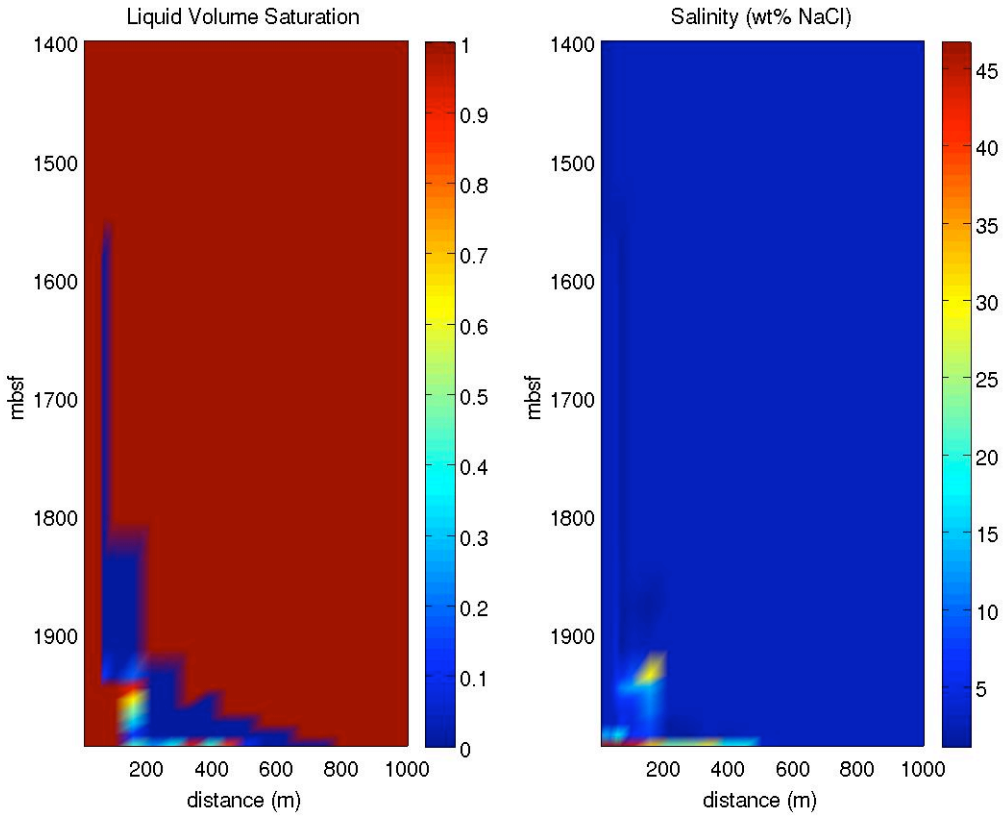

Figure 44 Liquid volume saturations and bulk salinities (wt% NaCl) at the intersection of the cross-flow and discharge zones. The two-phase zone extends all the way to the left hand boundary, but is very thin there, and so cannot be seen in the scale of these figures.

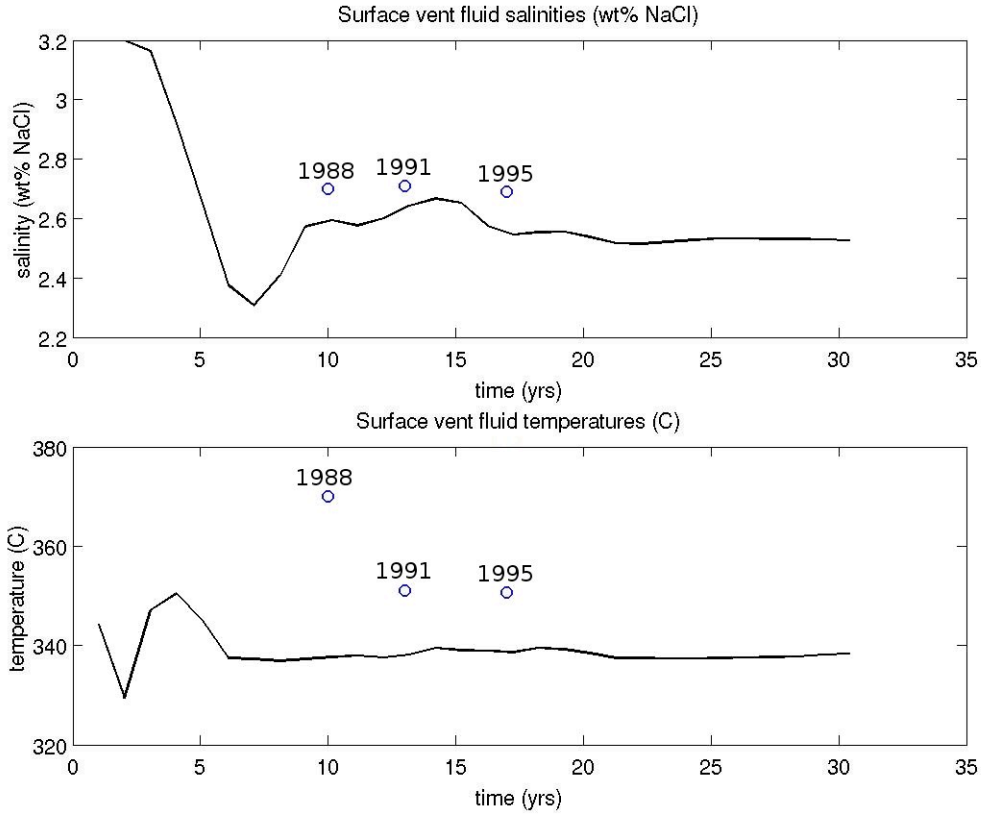

Figure 45 Surface vent fluid salinities and temperatures. Circles represent observed values from Dante vent at the Main Endeavor Field.

The above simulation was repeated except with a maximum temperature of 460°C instead of 480°C, and the results are shown in Figures 46, 47, and 48. The results are very similar to those of the last simulation, except that the two-phase region is now smaller. Because the two-phase region does not exist above the fluid from the counter clockwise eddy, brine is no longer mixed there and settles at the base of the system (Figures 46 and 47). Hence, there is only low salinity fluid heading toward the top of the system in this simulation, resulting in the vent fluid temperatures and salinity shown in Figure 48. Measured values from Hulk vent at the Main Endeavor Field are shown for the years

1988, 1991, and 1995. The vent fluid salinities match fairly well, though again there is a discrepancy between the simulated and observed temperatures.

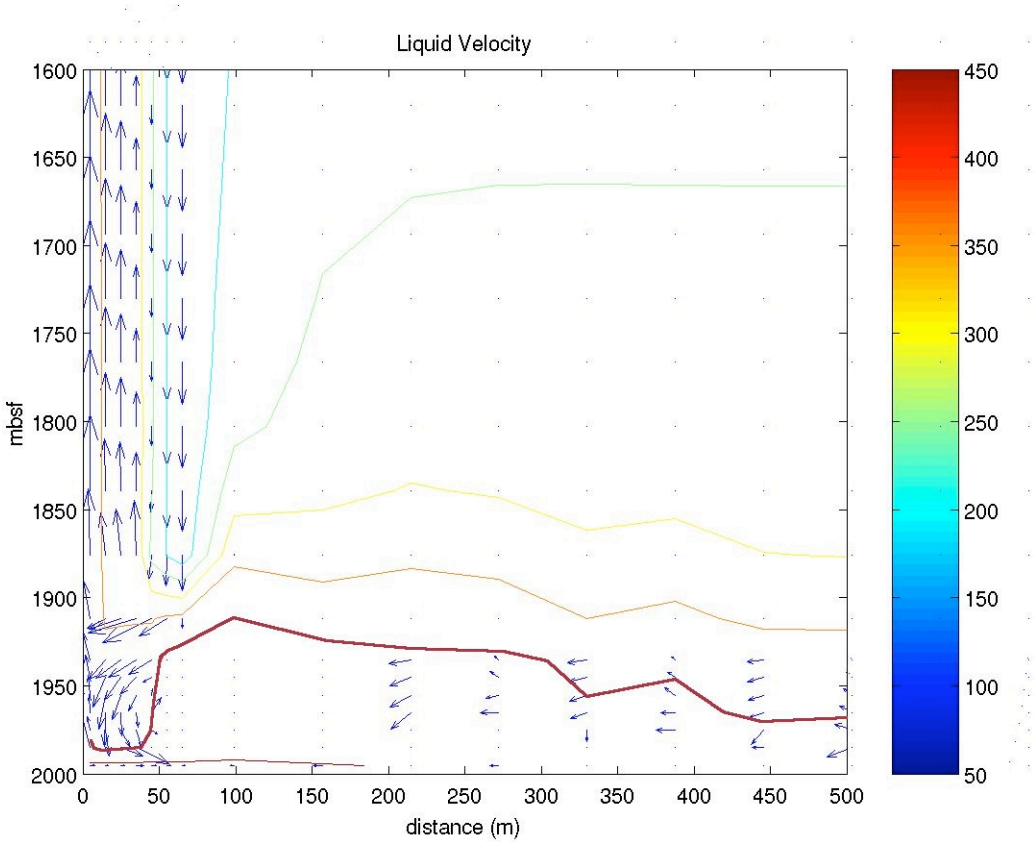

Figure 46 Liquid velocities and isotherms (°C) at the intersection of the cross-flow and discharge zones. The boundary of the two-phase region coincides roughly with the bolded isotherm.

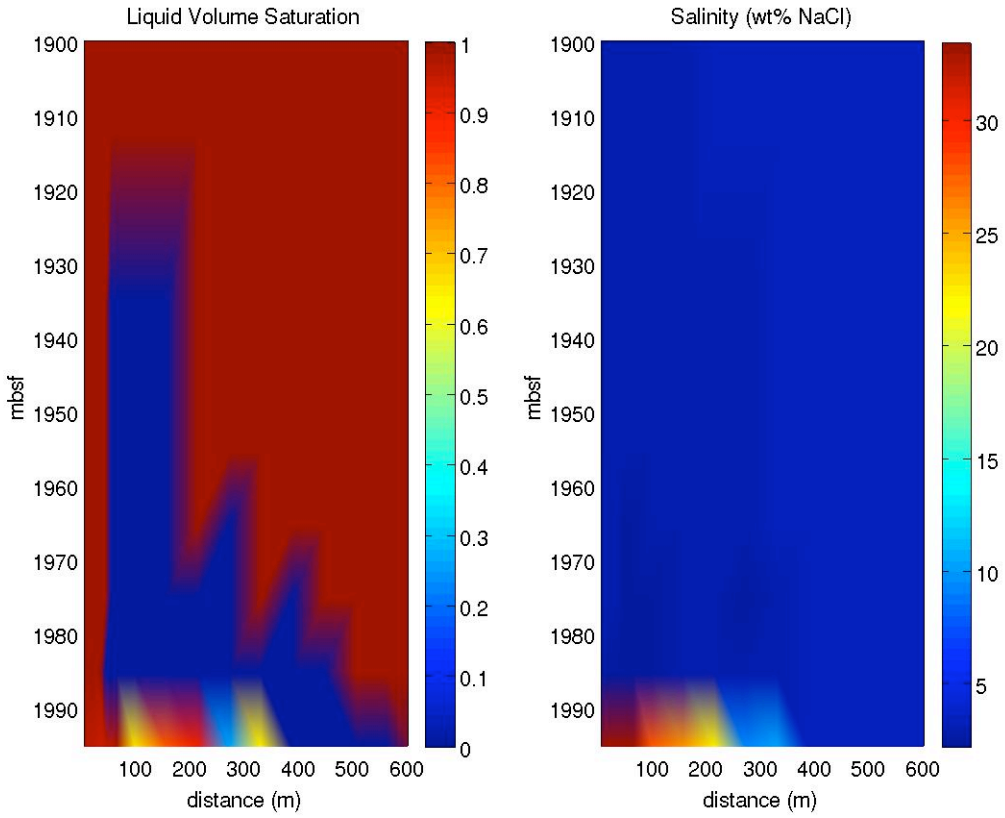

Figure 47 Liquid volume saturations and bulk salinities (wt% NaCl) at the intersection of the cross-flow and discharge zones.

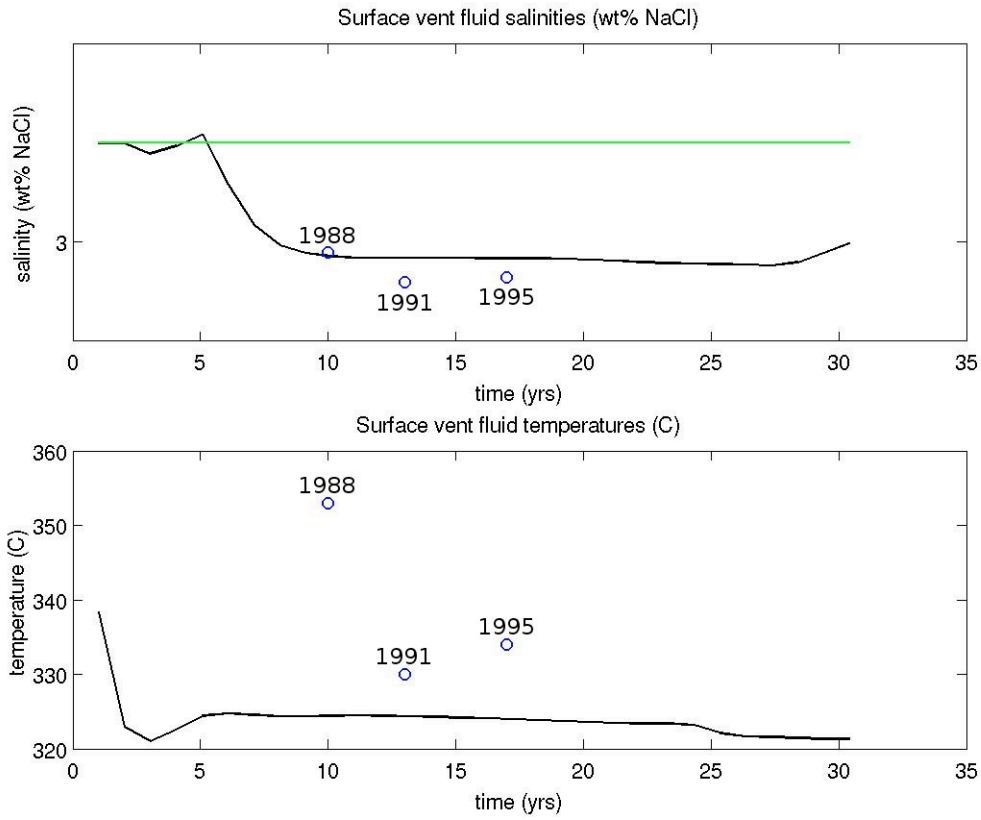

Figure 48 Surface vent fluid salinities and temperatures. Blue circles represent observed values from the vent Hulk and the Main Endeavor Vent Field.

When the single pass model is constructed to fit known geological constraints at the Main Endeavour Field vents, simulations of a quasi-steady state two-phase zone at depth still display many of the key features outlined for the systems in section 5.1: brine is formed at the base of the system, low salinity vapor collects at the top of the two-phase region and dilutes the single-phase fluid above it, forming a channel of low salinity fluid that makes its way toward the seafloor in a well-defined, high temperature conduit, and finally these processes give rise to vent fluid temperatures and salinities that evolve to roughly constant values on a decadal time scale. However, when the two-phase zone is

extensive enough to overlay the single phase fluid corner eddy, brine dropping out from the two-phase region becomes well mixed and begins to head toward the seafloor, though at a slower rate than the low salinity fluid.

In addition to the Endeavour-type simulations having the same general features of the earlier single pass simulations of this chapter, the observed pre-1999 salinities of venting fluids from Dante and Hulk at the Main Endeavor Field have been matched using the numerical single pass model approach. One can generate, via this approach, constant temperatures within the appropriate range (i.e., between approximately 330 and 380°C, as in Figures 44 and 47); however, the present approach is not able to reproduce the exact observed temperatures, as the current framework predicts temporally constant vent fluid temperatures. Moreover, the simulated temperatures are consistently lower than the observed temperatures. To obtain vent fluid salinities matching the other vent fluids at the Main Endeavor Field (which have salinities lower than 2.7 wt% NaCl), the two-phase zone would have to be made more extensive, thus increasing the chances that brine flowing out of the two-phase region will become mixed with upward moving fluid. In a study of brine storage applied to the Main Endeavour Field, Fontaine and Wilcock [2006] argue that interfacial tensions between fluid and halite phases tends to force brines into lower permeability structures and vapor into those of higher permeability. If they are correct, then heterogeneous permeability structures could be included in the single pass system to increase the efficiency of brine storage. Future work should concentrate on the effects of such heterogeneous structures on the storage of brine within the context of the models developed in this chapter. Similarly, if the two-phase zone can be expanded

without giving rise to upward moving brine, then its average temperature could be increased in order to produce surface vent fluid temperatures closer to those observed.

It should also be pointed out that, even though a variety of temporally stable vent fluid temperatures can be generated from the techniques described in chapter, the detailed linkage between the magma chamber and the bottom boundary of the system are not taken into account in the present work. It is an open question whether Dirichlet, Neumann, or some other type of boundary condition is the most appropriate for modeling heat transfer from a magma lens into a seafloor hydrothermal system. Future work should explore this issue – even if it turns out that there is no one type of boundary condition that is best for most cases, it is still worthwhile to investigate the effects that a variety of heating boundary conditions would have on the character of fluid flow in seafloor systems.

6.4 Conclusions from the fully numerical approach

A new finite volume algorithm for simulating fluid flow in seafloor hydrothermal systems has been introduced. The equations it employs and how they are coupled together via a time marching scheme with appropriate equations of state has been described in detail. The code was benchmarked against previously published heat pipe results from GTHSW and the differences between results were attributable solely to differences in the equations of state used. Further benchmark simulations included the Elder problem and comparison of temperatures in an approximately one dimensional discharge zone with the analytic solution to the classical thermal convection equation; both of these comparisons produced results in agreement with those expected of a first-order accurate numerical scheme. Application of the code to the single pass model led to

results that help to flesh out the supposed mechanism underlying the conceptual model for understanding surface vent fluid salinity variations associated with seafloor hydrothermal systems. This model has now been shown to be consistent with at least approximate solutions to the equations governing mass, energy, and momentum conservation and for geometries plausible for actual venting systems. Finally, a simulation designed to represent a generic Main Endeavour Field venting system was executed, and the results were shown to have many of the essential broad features required in order to explain the spatio-temporal variations in vent fluid salinity at the Main Endeavour Field using the conceptual model of vent fluid salinity variation from the single pass model perspective. In particular, vent fluid salinities and temperatures near observed values from Dante and Hulk vents were reproduced using this approach.

RECOMMENDATIONS FOR FURTHER WORK

Firstly, it must be emphasized that FISHES is only a first-order accurate scheme. First-order accuracy is often appropriate for initial studies, particularly when there is no other numerical software available that is up to the task at hand; however, the numerical properties of FISHES should continue to be studied, with a view toward upgrading it to a scheme of second-order accuracy. Furthermore, the salinity equation as currently implemented has all but the unsteady term included in the source, which contributes to numerical instability. If a way could be found to discretize this equation such that the source term is reduced, then the stability of the code would be much improved. Useful additional features for the code in the future would be: time dependent permeability and boundary conditions; more detailed output, including options to print the Peclet numbers, Rayleigh numbers, and other commonly used non-dimensional quantities of fluid dynamics; automatic grid adaptation; and the ability to simulate three-dimensional systems. Also, the equations of state employed by FISHES only go up to temperatures of 800°C. To simulate dike intrusions without employing artificial boundary conditions, it is necessary that the equation of state go up to temperatures of at least 1200°C; hence, the lookup-tables should be extended to this temperature. Finally, the equations of state should be upgraded to fully include the thermodynamic effects of halite precipitation, as this process is likely to occur in very many, perhaps most, of the situations of interest in modeling phase separation in seafloor hydrothermal systems.

Although the effect of increasing the grid resolution was partly investigated in section 6.3.1, there is certainly a need for more grid resolution studies. In addition, the

effects of increasing system depth, changing the seafloor pressure, and having an extrusive slab overlaying the system should also be studied more thoroughly. Once the equation of state has been modified to handle higher temperatures (see above), dike intrusion studies should be carried out. The results of these studies should be compared with the semi-numerical results concerning two-phase flow adjacent to a dike from Chapter 3 of this thesis. Dike intrusion studies could be in the context of the single pass model, i.e., considering the case of a dike intrusion in the discharge zone, but also purely theoretical contexts are of some interest, such as phase separation adjacent to a dike that forms the side boundary of a large cell-convection type system.

APPENDIX 1: EQUATION DISCRETIZATION

The following sections describe how the differential equations presented in section 4.2 are discretized to produce systems of linear algebraic equations suitable for numerical solution in a time marching scheme. The reader is assumed to be familiar with the methods of Patankar (1980); additionally, the notation is chosen to reflect closely that used by Patankar as well as that employed in the code FISHES. Starting from the equations of section 4.2 and working from within the above-mentioned framework, one may use this appendix to understand the code that constitutes the equation solver for FISHES.

A1.1 The Pressure Equation

The pressure equation is

$$\phi\frac{\partial\rho}{\partial P}\frac{\partial P}{\partial t}+\nabla\cdot(\rho_v\vec{v}_v+\rho_l\vec{v}_l)=-\phi\left(\frac{\partial\rho}{\partial X}\frac{\partial X}{\partial t}+\frac{\partial\rho}{\partial T}\frac{\partial T}{\partial t}\right) \tag{A1.1}$$

where the symbols have the same meanings ascribed to them in section 4.2. After the expressions in (4.1) for the Darcian velocities are inserted, this equation takes the form

$$\phi\frac{\partial\rho}{\partial P}\frac{\partial P}{\partial t}-\nabla\cdot(\Gamma_1\nabla P)=Q \tag{A1.2}$$

when the following abbreviations are made:

$$Q\equiv Q_1+Q_2 \tag{A1.3}$$

$$Q_1\equiv-\phi\left(\frac{\partial\rho}{\partial X}\frac{\partial X}{\partial t}+\frac{\partial\rho}{\partial T}\frac{\partial T}{\partial t}\right) \tag{A1.4}$$

$$Q_2\equiv-\nabla\cdot(\Gamma_2\nabla z) \tag{A1.5}$$

$$\Gamma_1 \equiv \Gamma_{1v} + \Gamma_{1l} \tag{A1.6}$$

$$\Gamma_2 \equiv \Gamma_{2v} + \Gamma_{2l} \tag{A1.7}$$

$$\Gamma_{1v,l} \equiv \frac{Kk_{rv,l}\rho_{v,l}}{\mu_{v,l}} \tag{A1.8}$$

$$\Gamma_{2v,l} \equiv \frac{Kk_{rv,l}\rho_{v,l}^2 g}{\mu_{v,l}} \tag{A1.9}$$

where (A1.8) and (A1.9) represent two definitions each, one corresponding to vapor phase properties and another corresponding to liquid phase properties. Note that the gravity terms in Darcy's law are considered as part of the numerical source term Q via expressions (A1.5), (A1.7), and (A1.9). Equation (A1.2) is discretized by spatial integration over an individual node centered control volume and temporal integration over one time step:

$$\int_V \int_t^{t+\Delta t} \phi \frac{\partial \rho}{\partial P} \frac{\partial P}{\partial t} dt dV - \int_t^{t+\Delta t} \int_V \nabla \cdot (\Gamma_1 \nabla P) dV dt = \int_t^{t+\Delta t} \int_V Q dV dt \tag{A1.10}$$

For the time integration, the newest available values are assumed to dominate over the time step; this assumption constitutes the fully implicit approach. The newest values could be represented by primed variables, but primes will be omitted to avoid unnecessary clutter, while variables from the previous time step will be labeled with a naught subscript. With the above assumptions in place, the integrated unsteady term per unit volume and per unit time is

$$\phi \frac{\partial \rho}{\partial P} \frac{(P_P - P_0)}{\Delta t} \tag{A1.11}$$

where the subscript P refers to the value at the node on which the control volume is centered. The integrated source term per unit volume and time is approximated by

$$\overline{Q}_1 - \frac{\Gamma_{2b} - \Gamma_{2\tau}}{\Delta z} \tag{A1.12}$$

where the bar denotes an average value, the subscripts b and τ refer to values of the variable at the bottom and the top faces of the control volume, respectively, and Δz is the height of the control volume. The time derivatives in the averaged term are computed using values from two previous time steps, when two previous time steps are available (otherwise they are set to zero); the values of the derivatives at the center of the control volume (i.e., at the node) are taken as average values for the control volume as a whole. The integrated divergence term per unit volume and time is approximated as

$$\frac{\Gamma_{1e} P_E}{\delta x_{PE} \Delta x} + \frac{\Gamma_{1w} P_W}{\delta x_{PW} \Delta x} + \frac{\Gamma_{1\tau} P_T}{\delta z_{PT} \Delta z} + \frac{\Gamma_{1b} P_B}{\delta z_{PB} \Delta z} - \alpha P_P \tag{A1.13}$$

where

$$\alpha \equiv a_E + a_W + a_T + a_B \tag{A1.14}$$

$$a_{W,E} \equiv \frac{\Gamma_{1w,e}}{\delta x_{PW,E} \Delta x} \tag{A1.15}$$

$$a_{T,B} \equiv \frac{\Gamma_{1\tau,b}}{\delta z_{PT,B} \Delta z} \tag{A1.16}$$

The subscripts W, E, T, and B refer to values at the west, east, top, and bottom nodes relative to the current node P, respectively; subscripts w and e refer to values on the west and east faces of the control volume, respectively. Δx refers to the width of the control volume, and equations (A1.15) and (A1.16) represent two equations each. With the above

definitions and approximations, the entire integrated pressure equation per unit volume and time can be written as

$$a_P P_P = a_W P_W + a_E P_E + a_T P_T + a_B P_B + b \tag{A1.17}$$

with

$$b \equiv \overline{Q_1} - \frac{\Gamma_{2b} - \Gamma_{2\tau}}{\Delta z} + \phi \frac{\partial \rho}{\partial P} \frac{P_0}{\Delta t} \tag{A1.18}$$

and

$$a_P \equiv \alpha + \phi \frac{\partial \rho}{\partial P} \frac{1}{\Delta t}. \tag{A1.19}$$

When values for the coefficients in equation (A1.17) are stored for each node in the problem domain, a set of linear algebraic equations results, which can be solved for the pressure P_P at every node P.

A1.2 The Temperature Equation

The temperature equation can be written as

$$(1-\phi)\rho_r c_r \frac{\partial T}{\partial t} + \nabla \cdot (\vec{F} T) = \nabla \cdot (\lambda_m \nabla T) + Q_T \tag{A1.20}$$

with the following defined terms:

$$Q_T \equiv Q_{T1} + Q_{T2} \tag{A1.21}$$

$$Q_{T1} \equiv -\phi \rho \frac{\partial h}{\partial t} \tag{A1.22}$$

$$Q_{T2} \equiv h \nabla \cdot (\rho_v \vec{v}_v + \rho_l \vec{v}_l) \tag{A1.23}$$

$$\vec{F} \equiv \vec{F}_v + \vec{F}_l \tag{A1.24}$$

and

$$\vec{F}_{v,l} \equiv \rho_{v,l} c_{v,l} \vec{v}_{v,l} \,. \tag{A1.25}$$

All terms not defined here carry the same meanings ascribed to them in section 4.2. The integrated unsteady term per unit volume and per unit time is approximated by

$$\frac{(1-\phi)\rho_r c_r}{\Delta t} T_P - \frac{(1-\phi)\rho_r c_r T_0}{\Delta t} \tag{A1.26}$$

where the subscripts P and naught have the same meanings as in the derivation of the discretized pressure equation. The advective term is approximated using full upstream weighting, so that the integrated advective term per unit volume and time is

$$\begin{aligned} &\left(\frac{\lceil F_{xe}, 0 \rceil + \lceil -F_{xw}, 0 \rceil}{\Delta x} + \frac{\lceil F_{zb}, 0 \rceil + \lceil -F_{z\tau}, 0 \rceil}{\Delta z} \right) T_P - \\ &\frac{\lceil -F_{xe}, 0 \rceil}{\Delta x} T_E - \frac{\lceil F_{xw}, 0 \rceil}{\Delta x} T_W - \frac{\lceil F_{z\tau}, 0 \rceil}{\Delta z} T_T - \frac{\lceil -F_{zb}, 0 \rceil}{\Delta z} T_B \end{aligned} \tag{A1.28}$$

where inverted L-shaped brackets indicate the maximum function. The approximated integrated diffusion term per volume and time is

$$\begin{aligned} &\frac{\lambda_e}{\delta x_{PE} \Delta x} T_E + \frac{\lambda_w}{\delta x_{PW} \Delta x} T_W + \frac{\lambda_b}{\delta z_{PB} \Delta z} T_B + \frac{\lambda_\tau}{\delta_{PT} \Delta z} T_T - \\ &\left(\frac{\lambda_e}{\delta x_{PE} \Delta x} + \frac{\lambda_w}{\delta x_{PW} \Delta x} + \frac{\lambda_b}{\delta z_{PB} \Delta z} + \frac{\lambda_\tau}{\delta z_{PT} \Delta z} \right) T_P \end{aligned} \tag{A1.29}$$

Finally, the integrated source term per unit volume and time is approximately

$$\overline{Q}_{T1} + \overline{h} \left(\frac{M_{xe} - M_{xw}}{\Delta x} + \frac{M_{zb} - M_{z\tau}}{\Delta z} \right) \tag{A1.30}$$

where the bar represents averaging of the same kind as for the averaged part of the source term in the pressure equation, and

$$M_{x,z} \equiv \rho_v v_{vx,z} + \rho_l v_{lx,z} \tag{A1.31}$$

are the total mass fluxes in the x and z directions. Combining the above expressions results in the discretized temperature equation

$$n_P T_P = n_W T_W + n_E T_E + n_T T_T + n_B T_B + b \tag{A1.32}$$

where

$$n_W \equiv \frac{\lambda_w}{\delta x_{PW} \Delta x} + \frac{\lceil F_{xw}, 0 \rceil}{\Delta x} \tag{A1.33}$$

$$n_E \equiv \frac{\lambda_e}{\delta x_{PE} \Delta x} + \frac{\lceil -F_{xe}, 0 \rceil}{\Delta x} \tag{A1.34}$$

$$n_T \equiv \frac{\lambda_\tau}{\delta z_{PT} \Delta z} + \frac{\lceil F_{z\tau}, 0 \rceil}{\Delta z} \tag{A1.35}$$

$$n_B \equiv \frac{\lambda_b}{\delta z_{PB} \Delta z} + \frac{\lceil -F_{zb}, 0 \rceil}{\Delta z} \tag{A1.36}$$

$$n_P \equiv \frac{\lambda_w}{\delta x_{PW} \Delta x} + \frac{\lambda_e}{\delta x_{PE} \Delta x} + \frac{\lambda_\tau}{\delta z_{PT} \Delta z} + \frac{\lambda_b}{\delta z_{PB} \Delta z} + \frac{\lceil F_{xe}, 0 \rceil + \lceil -F_{xw}, 0 \rceil}{\Delta x} + \frac{\lceil F_{zb}, 0 \rceil + \lceil -F_{z\tau}, 0 \rceil}{\Delta z} + \frac{(1-\phi)\rho_r c_r}{\Delta t} \tag{A1.37}$$

and

$$b \equiv \overline{Q}_{T1} + \frac{(1-\phi)\rho_r c_r T_0}{\Delta t} . \tag{A1.38}$$

A1.3 The Salinity Equation

The salinity equation is

$$\frac{\partial(\phi \rho X)}{\partial t} + \nabla \cdot (\rho_v \vec{v}_v X_v + \rho_l \vec{v}_l X_l) = \nabla \cdot (\phi \rho_l D \nabla X_l + \phi \rho_v D X_v) . \tag{A1.39}$$

Because the bulk salinity occurs only in the unsteady term, the other terms in the equation would have to be treated formally as source terms if the salinity equation were to be discretized in the same manner as the pressure and temperature equations. Because the presence of so many source terms eliminates the advantages of solving the salinity equation in a form such as (A1.17) or (A1.32), equation (A1.39) is solved indirectly, by calculating the amounts of salt and mass entering a control volume during a time interval, adjusting the total salt and mass content in the control volume to reflect these changes, and dividing the total salt by the total mass to obtain the bulk salinity at the node in that volume. The diffusive salt fluxes are evaluated using Fick's law of chemical diffusion for salt:

$$\vec{q}_{l,v} = \phi \rho_{l,v} D \nabla X_{l,v} \tag{A1.40}$$

The approximations to (A1.40) on the control volume faces are as follows:

$$q_{tl,v} = \phi \rho_{tl,v} D \frac{(X_{Pl,v} - X_{Tl,v})}{\delta z_{PT}} \tag{A1.41}$$

$$q_{bl,v} = \phi \rho_{bl,v} D \frac{(X_{Bl,v} - X_{Pl,v})}{\delta z_{PB}} \tag{A1.42}$$

$$q_{wl,v} = \phi \rho_{wl,v} D \frac{(X_{Pl,v} - X_{Wl,v})}{\delta x_{PW}} \tag{A1.43}$$

$$q_{el,v} = \phi \rho_{el,v} D \frac{(X_{El,v} - X_{Pl,v})}{\delta x_{PE}} \tag{A1.44}$$

The advective salt and mass fluxes are given by

$$\vec{f}_{l,v} = \rho_{l,v} X_{l,v} \vec{v}_{l,v} \tag{A1.45}$$

and

$$\vec{g}_{l,v} = \rho_{l,v}\vec{v}_{l,v}\,. \tag{A1.46}$$

The advective fluxes on the control volume faces are given by the stored interface values of the liquid and vapor densities, salinities, and velocities.

APPENDIX 2: INTERPOLATION METHODS

To implement the thermodynamic equations of state discussed in section 4.3, it is necessary to linearly interpolate between values stored in lookup tables. The sections below describe how the interpolation is carried out for values on the upper boundary of the two-phase region as well as for bulk quantities corresponding to points that do not necessarily lie on any phase equilibria surface. Interpolating on the upper boundary of the two-phase region is complicated by the fact that the lookup tables containing values of thermodynamic variables on that surface are non-uniform with respect to pressure; the reason for this non-uniformity is discussed in the following section.

A2.1 Interpolating Quantities on the Upper Boundary of the Two-Phase Region

Let $\chi(T,P)$ be the value of the liquid or vapor salinity or density on the upper boundary of the two-phase region obtained from interpolation between table values. The tables are those referred to in section 4.3 and consist of three matrices – a matrix of temperatures, a matrix of pressures, and a matrix containing values of χ corresponding to each tabulated (T,P) pair. On each row of the temperature matrix, the temperature is constant and the corresponding values in the pressure matrix vary between the critical and 3-phase pressures. The reader may wish to follow Figure 44 to aid in visualizing the steps that follow. Assume that T is between table temperatures T_1 and T_2 inclusive, and define

$$f_P \equiv \frac{P - P_3(T)}{P_C(T) - P_3(T)} \tag{A2.1}$$

where P_3 is the 3-phase pressure and P_C is the critical pressure, both at temperature T. Because P is between P_3 and P_C inclusive, f_P is the fractional distance to the critical

pressure from the 3-phase pressure. This fraction is used to project the pressure at T onto pressures at T_1 and T_2 that are equivalent to P in the sense that they are at the same relative distance between P_C and P_3. This projection is necessary because the table spacing in (P,T) space is non-uniform with respect to pressure; this non-uniform spacing stems from the fact that the pressures P_C and P_3 bounding the upper boundary of the two-phase region above and below are temperature dependent. If the tables had been made uniform in pressure, then their resolution would have varied in phase space and would have decreased near the critical and 3-phase pressures; hence, non-uniform pressure spacing was adopted in the construction of the lookup tables. The projected pressures P_1 and P_2 are given by

$$P_1 = (1 - f_P)P_3(T_1) + f_P P_C(T_1) \tag{A2.2}$$

$$P_2 = (1 - f_P)P_3(T_2) + f_P P_C(T_2)\,. \tag{A2.3}$$

If P_{11} and P_{12} are table pressures on the row corresponding to T_1, and if P_1 lies between these pressures inclusively, then table values of χ on that row are given by

$$\chi_{11} = \chi(T_1, P_{11}) \tag{A2.4}$$

$$\chi_{12} = \chi(T_1, P_{12}) \tag{A2.5}$$

Similarly, if P_{21} and P_{22} are table pressures on the row corresponding to T_2, and if P_2 lies between these pressures inclusively, then table values of χ on the row of T_2 are given by

$$\chi_{21} = \chi(T_2, P_{21}) \tag{A2.6}$$

$$\chi_{22} = \chi(T_2, P_{22}) \tag{A2.7}$$

Therefore, once P_{11}, P_{12}, P_{21}, and P_{22} are located in the pressure table via an appropriate search algorithm (such as the bisection method), interpolated values of χ at temperatures T_1 and T_2 are given by

$$\chi_{T1} = \left(\frac{\chi_{12} - \chi_{11}}{P_{12} - P_{11}} \right) (P_1 - P_{11}) + \chi_{11} \tag{A2.8}$$

$$\chi_{T2} = \left(\frac{\chi_{22} - \chi_{21}}{P_{22} - P_{21}} \right) (P_2 - P_{21}) + \chi_{21} \tag{A2.9}$$

Finally, $\chi(T,P)$ can be obtained by interpolating linearly between χ_{T1} and χ_{T2} with respect to temperature:

$$\chi(T,P) = (1 - f_T)\chi_{T1} + f_T \chi_{T2} \tag{A2.10}$$

where

$$f_T \equiv \frac{T - T_1}{T_2 - T_1} \tag{A2.11}$$

is the fractional distance to T_2 from T_1. Figure 49 shows a magnified portion of Figure 17 with example locations of the projected pressures P_1 and P_2, with the values corresponding to table entries in boxes.

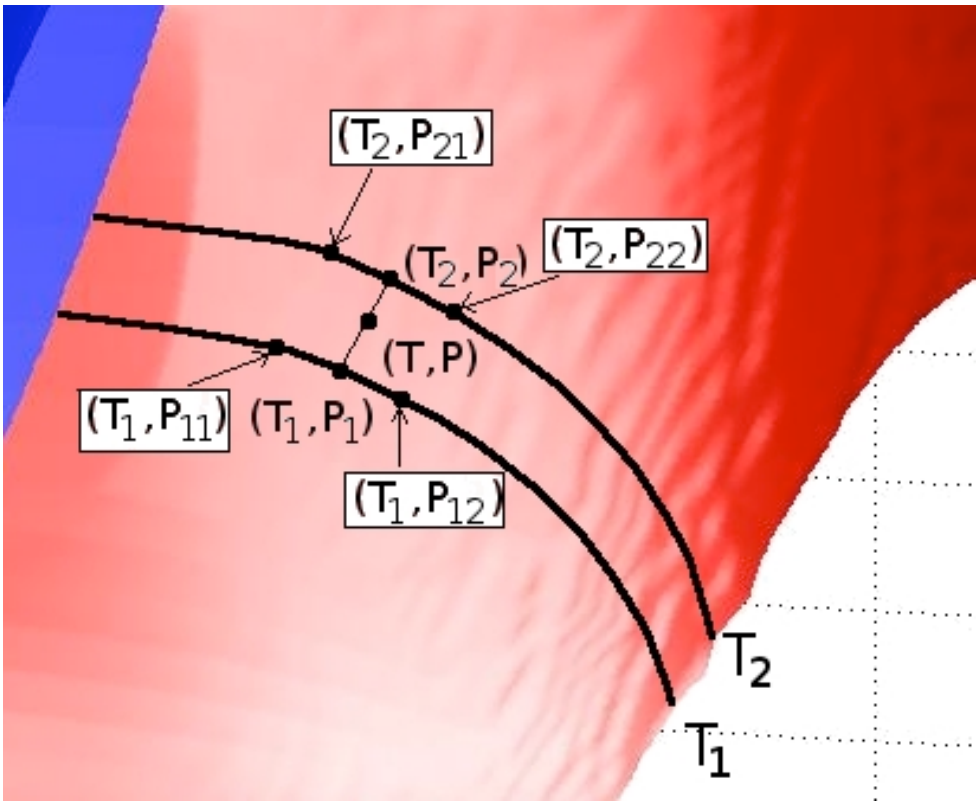

Figure 49 Magnified portion of the upper boundary of the two-phase region in terms of density, showing locations of the projected pressures and values for which table entries exist in boxes. The distance between T_1 and T_2 and between table pressures has been exaggerated for clarity.

A2.2 Interpolating Bulk Quantities in 3-D Phase Space

Let $\zeta(T,P,X)$ be the bulk density or enthalpy calculated from interpolation via matrices containing selected values of T, P, X, and ζ. In the two-phase region, bulk properties are functions of the liquid and vapor densities and salinities on the surface bounding the two-phase region from above; these values can be obtained by using the formalism of section A2.1. Hence, the interpolation procedure discussed below need only be implemented for (T,P,X) triples located outside of the two-phase region. The interpolation problem can be divided into four cases: 1) all three input values T, P, and X are located in the matrices already, so that ζ can be calculated simply by finding the

corresponding entry in the ζ table; 2) one of the inputs is not located in a table; 3) two of the inputs are not located in tables; 4) none of the input values are located in the tables. One can solve the interpolation problem by recursively reducing cases 4), 3), and 2) to case 1). Suppose that the input values are such that case 2) holds. The problem is symmetric with respect to which of T, P, or X is not in its corresponding table, so it suffices to consider the case where, say, T is not located in the temperature table. Using a search algorithm to find table values T_1 and T_2 such that $T_1 < T < T_2$, ζ at T_1 and T_2 can be evaluated as

$$\zeta_{T1} = \zeta(T_1, P, X) \tag{A2.12}$$

$$\zeta_{T2} = \zeta(T_2, P, X)\,. \tag{A2.13}$$

Then by defining

$$f_T \equiv \frac{T - T_1}{T_2 - T_1}\,, \tag{A2.14}$$

ζ can be evaluated via

$$\zeta(T, P, X) = (1 - f_T)\zeta_{T1} + f_T \zeta_{T2}\,. \tag{A2.15}$$

Equations (A2.12)-(A2.15) constitute a solution for the interpolation problem in case 2). Suppose that the input values are such that case 3) holds, and that (for instance) inputs T and P are not located in their respective tables. Then if table values T_1 and T_2 are located such that $T_1 < T < T_2$, equations (A2.12) and (A2.13) can be applied if there is a solution to the case 2) problem because, by assumption, in these equations only one input, P, is not located in its corresponding table. A solution to the problem for case 2) has been provided; so this solution can be applied to calculate (A2.12) and (A2.13), from which ζ can then be calculated using (A2.14) and (A2.15). In this way, case 3) is reducible to case

2), which is itself reducible to case 1). If case 4) obtains, then if table temperatures T_1 and T_2 such that $T_1 < T < T_2$ are located, calculating ζ via equations (A2.12) and (A2.13) requires a solution to the problem in case 3), because both P and X in these equations are not in their respective tables. But a solution to the case 3) problem has already been provided, so that case 4) is solved; therefore, all four cases have been accounted for and the interpolation problem is solved completely.

APPENDIX 3: GUIDE TO INSTALLING AND USING FISHES

The following sections are intended to constitute a practical guide to installing and using FISHES. Readers interested in the underlying theory should consult Chapter 4 of this thesis as well as the first two appendices.

A3.1 Installation

FISHES is written in FORTRAN 90, and the programs mentioned in this guide for analyzing the output of FISHES require Matlab. The code is compatible with a free FORTRAN 90/95 compiler, g95, which can be gotten from **http://www.g95.org**; it has also been successfully compiled and run using the Intel© FORTRAN compiler, ifort. It is recommended that one of these compilers be used, because different FORTRAN compilers have minor differences that can lead to a program compiling on one of them but not another. There are g95 binaries at the above-mentioned website for linux, solaris, windows, etc, and one can even compile the compiler itself from source code if one wishes – see the website for details. In linux, g95 uses the GNU C compiler gcc, and if there are any problems getting g95 to work, it is most likely because one is lacking the correct version of gcc. Regarding matlab, it is recommended that Matlab 7 or later be used.

Once Matlab and the FORTRAN compiler have been installed, it is time to install FISHES and the auxiliary programs that come with it. All the programs are compressed into the file FISHES.zip. To install the files, simply unzip this file in the directory of choice. After unzipping, there should be a main folder labeled **FISHES**, with a folder inside it labeled **run**. Inside the **run** folder, there should be four more folders: **Analysis**,

surfsamp, **InHelper**, and **PrevResults** (for storing input and output files that the user wishes to save). If all of these folders are present then the FISHES files have been installed correctly. It may be necessary to change the user permissions on the files and directories to allow the user to copy, edit, or read files (for unix/linux, the command chmod 711 <directory or filename> will suffice). Before running FISHES (or any of the auxiliary programs that come with it) for the first time, it is necessary to compile it for the particular machine on which it will run – that is why g95 or ifort is needed. For unix/linux users (I will assume that the users are employing linux or unix hereafter), there is a script in the FISHES directory called FishComp, and it will compile FISHES with the proper parameters, rename the compiled file from "a.out" to "fishes", and move the result to the run directory, which is where FISHES must execute, because all the input files and data files for the equations of state are located there. Edit the script and uncomment the lines appropriate for the compiler you plan to use. The script can be executed by typing ./FishComp from the FISHES directory. After the file "fishes" has been created in the run directory, one may need to go there and type chmod 711 fishes, to apply the right file permissions. Subsequently, to run FISHES itself, one can simply type ./fishes from the run directory.

A3.2 The Input Files

When FISHES runs, it reads the information in the files InFile0 and InFile1 to determine the problem geometry, the initial and boundary conditions, and other simulation controlling variables like the time step, iteration tolerances, etc. These user-defined variables will now be described, and they will each be printed in bold to facilitate ease of reference.

A3.2.1 InFile0

A simple example of an InFile0 is in the FISHES/run/ directory (there is also a backup of this file, InFile0.bak, in case the user would like to review this material later after having replaced the original example files). This file can be read with one's favorite text editor (the author's choice is vim, with text highlighting for FORTRAN 90 – a copy of the author's .vimrc file is included in the run directory, and is called vimrc). Regarding units in these files, SI units are used exclusively, except that salinity is in wt% NaCl and not wt. fraction NaCl (although internally FISHES converts the input salinities from wt% to wt. fractions).

The first variables in the file are NumNodesX, NumNodesY, and NumNodesZ – these are the number of nodes in the X (west-east), Y (north-south), and Z (up-down) directions. FISHES is currently only designed to handle up to two dimensions, so that Y should always be set to 1. In this example, there are 12 nodes total, with 3 nodes from west to east and 4 nodes from top to bottom. The variable SuppressScreenMessages should be set to Y if one wishes to run FISHES as a background process and does not want FISHES to send output to the screen while running; otherwise, this variable should be set to N.

The next line starts with the variable TimeStepIncr. This variable is for situations such that the user wants the time step to increase with time as the code runs – sometimes many changes happen quickly at once when a simulation starts, and the time step should be set comparatively small during these times, while later it may be possible to obtain meaningful results with a higher time step. For example, setting TimeStepIncr to 2 will double the time step size after each time marching step completes. Setting TimeStepIncr

to 1 keeps the time step the same (i.e., multiplies it by 1 after each time marching step), and this value is the standard one. Dispersivity and CorrelationLength are there for modeling mechanical salt dispersion, but currently the code uses numerical dispersion to simulate mechanical dispersion, so that these variables should be set to 0. These variables are there in case the author decides to model dispersion more rigorously in the future.

MassFluxGradual should be set to N unless one wants to have the mass flux at the bottom of the system increase gradually with time. If this variable is set to Y, then the next three variables must also be specified, namely, the starting mass flux, the ending mass flux (both in kg/m^2 s), and the interval of time over which this increase should take place (in seconds).

TempRelax, PresRelax, and SaliRelax are for if one wants to use under-relaxation on the temperature, pressure, or salinity during simulations. Under-relaxation slows the rate at which variables evolve with time by requiring the new values to be closer to the old values. Setting TempRelax to 0, for instance, would keep the temperature from changing with time at all, while setting it to 1 would cause the temperature to evolve normally. Numbers between 0 and 1 will have intermediate effects. An important thing to keep in mind is that, because under-relaxation causes variables to evolve more slowly in time than they otherwise would, it will be necessary to increase the TimeCalibration variable above 1 in there is a significant degree of under-relaxation. TimeCalibration should always be set to a whole integer value, and the number to which it is set is the number of extra times FISHES will solve the temperature, pressure, and salinity equations before letting simulation time pass. If one sets TempRelax, PressRelax, and

SaliRelax all to 10^{-1}, then setting TimeCalibration to about 10 will produce results that evolve at roughly the same overall rate that they would without under-relaxation. To be especially careful, one can calibrate against a known case for a similar problem setup to determine the best value for TimeCalibration. The default values are appropriate for most cases. The default under-relaxation for salinity is set to 10^{-1}, and should usually be set an order of magnitude lower than the under-relaxations for the pressure and temperature. The need for this under-relaxation is due to the salinity equation not being solved in the same manner as the temperature and pressure equations, as discussed in section A1.3.

The next variables, TempToler, PresToler, and SaliToler, govern relative iteration tolerances. If TempToler, for example, is set to 0.2 then the code will execute convergence iterations at each time marching step until the new values of temperature are within 20% of the old values of temperature. If the results do not converge within 1000 iterations, the code will halt and display a message to that effect. One can try to improve the chances of reaching convergence by lowering the time step or using under-relaxation. Until one is familiar with how iterations and under-relaxation work (by working with the code through various examples, or from previous experience), it is best to simply lower the time step if more accuracy is desired for a simulation. Iterations and other methods are primarily for when the time step becomes impractically small in order to achieve meaningful results otherwise.

RockDens, CpRock, RockThermCond, and Grav are the variables that store the rock density, rock specific heat at constant pressure, rock thermal conductivity, and gravitational acceleration, respectively. HaliteDens, CpHalite, FluidThermCond, and SaltChemDiff store the halite (solid salt) density, halite specific heat, fluid thermal

conductivity, and salt chemical diffusivity, respectively. CpHalite is not currently used for anything in the code – it is there for if the author decides to include the formation of halite in a more rigorous way in the future.

XNodeWidths, YNodeWidths, and ZNodeWidths store the node widths in the X, Y, and Z directions. The 'C' stands for "Constant" and means that the number below it will be the value for every node in the corresponding direction. For instance, in this InFile0, all the nodes in the X direction are set to a width of 1 meter, while all those in the Z direction are set to widths of 2 meters. Alternatively, 'F' stands for "Free" and when there is an F, all the numbers listed below are read into individual nodes. For example, suppose that the X widths line were as follows:

Node widths in the x direction(m)

F

0.1

1.0

1.0

In this case, the western-most nodes would have west-east widths of 0.1 meters, while the rest would have west-east widths of 1.0 meter.

Porosity and Permeability, Temperature, Pressure, and Salinity all store the initial values of the variables after which they are named (Salinity refers to the bulk salinity). Again, a 'C' means that all the nodes will be set to the constant value of the number immediately below C. For instance, all the nodes have been set to have a porosity of 0.1 (or 10%). The pressures, on the other hand, are set using the F descriptor, and the pressure values are listed afterward corresponding to the nodes in which they will be

stored. The temperatures are set to vary linearly from 100°C at the top of the system to 200°C at the bottom.

The last variables in InFile0 allow the user to specify different print frequencies and time step sizes for different intervals of simulation time. The number under "Number of time periods below to execute before stopping" refers to the number of such predefined intervals the user desires to employ. In this example, there are 2 such periods. The variables TotalTime, PrintFreq, and Delta_t refer to the simulation time interval, print frequency, and time step size, respectively. In this example, the simulation will run for 3.2E8 s (~10 yrs), printing output every 3.2E7 s (~1 yr), with a time step size of 1.E6 s. After 3.2E8 s of simulation time has passed, the code will run for another 6.4E8 s (~20 yrs), with the same print frequency as before, but now with a larger time step of 1.E7 s. Had the number of time periods to execute been set to 1 instead of 2, the code would stop simulating after only 3.2E8 s, the interval specified in the first pre-defined interval.

A3.2.2 InFile1

InFile1 contains information specifying the types of boundary conditions and the boundary values for solving the temperature, pressure, and bulk salinity equations. FISHES recognizes four types of nodes: constant boundary, flux boundary, upwind boundary, and interior nodes. A constant boundary node is a node that is both on the boundary of the system and that is to be held at a fixed value for the entire simulation, and such node types are designated with a C. A flux boundary node is a node that is both on the boundary and that specifies a constant flux for the entire simulation. It is signified by the letter F. Upwind boundary nodes are nodes on the boundary of the system whose values are determined from their initial values plus the upwind condition. This condition

is symbolized with a U, and will be explained more fully below. Finally, an interior node, designated by I, is simply any node that is not on a boundary.

PresNodeTypes is the variable storing the node types with respect to pressure. In this example, the pressures at the top of the system are held constant, while all the other boundary nodes are set at constant mass fluxes (note that the mass fluxes have units of kg/m^2s). The interior nodes are marked I. TempNodeTypes stores the node types with respect to temperature. In this example, the nodes at the top of the system have all been set to the upwind boundary condition, while the side boundary nodes are set to constant heat fluxes (J/m^2s), and the bottom nodes are set to constant temperatures. SaliNodeTypes stores the node types with respect to salinity, and these are set similarly to those for the temperature, except that the bottom nodes are set at constant salt mass fluxes instead of constant salinity values.

Now that the node types have been set, the specific numerical values for these node types must be recorded. PresBoundVals stores the pressure boundary values. Interior nodes are marked 0 simply to reflect again that they are not on the boundary (so these nodes are not set to initial pressures of 0 – the initial pressures for the internal nodes were specified in InFile0 already). The top pressures in this example are held fixed at 260.D5 Pa (260 bars), while the sides and bottom of the system are set to zero mass flux. TempBoundVals stores the temperature boundary values. The temperatures at the top of the system have been set to initial values of 100°C (consistent with the initial values set in InFile0); however, if fluid flows from inside the system out of the top, the temperature at the top node with change to the temperature of the node just below it. For instance, if the node immediately below the upstream condition node were, say, 105°C, then fluid

flowing upward out of the system would cause the temperature in the top node to change from 100°C to 105°C. The upstream condition is meant to represent the fact that changes upstream in a moving fluid influence what happens downstream. If fluid flows from the top of the system downward, then the top node will shift back to its initial value of 100°C. The bottom temperatures have been set to a constant 200°C, while the sides of the system are thermally insulated (heat fluxes = 0). SaliBoundVals stores the salinity boundary values. The top nodes are set at initial values of 3.2 wt% NaCl, with the upstream condition governing later values. The sides and the bottom of the system are set at zero salt flux.

A3.3 The Output Files

There are four output files to which FISHES writes as it runs, numbered from 0 to 3. In them are stored the initial problem setup information, the bulk fluid properties, the fluid velocities, and the individual phase properties, respectively. A detailed description of each follows, and the example OutFiles provided in the run directory are those that result from running FISHES with the example InFiles.

A3.3.1 OutFile0

This output file is a summary of all the user-defined variables that have been read into memory for the simulation. If one desires to check that the input files were read in properly with the appropriate values, then this file is the one to check. Everything in this file is labeled fairly obviously; however, below some variables, like the porosity for instance, the phrase "Slice: 1" will be seen. This phrase is just to indicate that the Y dimension is set to 1 – if the code were set up to handle three dimensions, then there would be more than one "slice" of X-Z values for each variable.

A3.3.2 OutFile1

This file stores the phase indices, liquid volume saturation, bulk densities, pressures, temperatures, bulk salinities, and bulk enthalpies generated during the simulation. Again, one can ignore the "Slice: 1" comments. Note that the phase indices are labeled numerically as

-2 = liquid + halite

-1 = pure liquid

0 = two-phase (liquid + vapor) mixture

1 = pure vapor

2 = vapor + halite

The code uses these numbers internally to identify which phase is present at each node.

A3.3.3 OutFile2

In addition to the velocities being vectors, they are stored at the interfaces between nodes, which makes reading the velocity data file slightly more complicated than reading the others. Velocities are listed in OutFile2 for the liquid and vapor phases separately, and for the X and Z directions separately. In our example setup, there are three nodes in the X direction, and so there are two interfaces in the X direction between nodes. In OutFile2, the phrase "X direction interface slice: 1" indicates that what follows is the velocity at the first interface in the X direction. Similarly, "X direction interface slice: 2" means that what follows is the velocity at the second interface in the X direction. Because there are four nodes in the Z direction, there are three interfaces between nodes in this direction. Hence, there are three slices each for each velocity component in that direction, and for each phase.

A3.3.4 OutFile3

OutFile3 is arranged like OutFile1, except that it stores the individual vapor and liquid salinities, enthalpies, and densities instead of the corresponding bulk properties.

A3.4 Helpful Auxiliary Programs

There are five auxiliary programs that will make creating the input files and reading / plotting the results from the output files much easier than otherwise, especially for problem setups that require a large number of nodes. They are described below.

A3.4.1 InHelp

This program is located in the InHelper folder under the run directory. Before one can run InHelp, the first time it must be compiled. To compiled it using g95, for instance, type g95 *.f95 from the InHelper directory, and then type mv a.out InHelp. Finally one may need to type chmod 711 InHelp to apply the proper permissions to this file. One can then run it in unix/linux by typing ./InHelp from that directory. Upon running this program, a menu will appear followed by a prompt for the menu selection. The example InFile0 and InFile1 are already in this directory, and these are the files InHelp reads when it is run. If the user changes, for example, the permeabilities, and then asks InHelp to save, the result will be files just like the example InFile0 and InFile1 except with altered permeability information. When the program writes output, it writes the output to the files InFile0.new and InFile1.new so that if a mistake has been made the original InFile0 and InFile1 will not be affected. By experimenting with the options in the menu and viewing the output, it should become clear how this program works. Here is an example. Suppose the user selects option three, to modify the permeabilities. A new menu will then appear, with the options “1 select starting and ending rows/columns” and “2 return to

main menu". Selecting one leads to the prompt "starting row:", and after specifying the starting row, one is asked to specify the ending row, the starting column, and the ending column. Essentially, a square of nodes is being specified, which will then be filled in with values determined by the user. Suppose for starting row, ending row, starting column, and ending column one has entered 1, 3, 2, 3, respectively. Then the region of space selected will look like the following (where o stands for a node, and x stands for a selected node):

o x x

o x x

o x x

o o o

After selecting the nodes that will have altered permeabilities, the user is then given the choices "constant (C)", "linear left to right (L)", or "linear top to bottom (T)". Choosing C will set all the selected node permeabilities to one constant value. Choosing L will cause the permeabilities to vary linearly with distance from west to east, and choosing T will cause them to vary linearly with distance from the top toward the bottom of the system. For InHelp to function properly, it is important that every field in the initial input files be set to *some value*, so if the geometry of the system or number of nodes is changed from that of the original input files using InHelp, the user will need to go through every entry on the menu to insure that all parameters are defined to prevent the next iteration of InHelp from crashing when it acts upon its own output from the previous run.

A3.4.2 analyze

After FISHES has been run, or even while it is still running (as long as there has been *some* output to the output files), one can run a script in the run directory called analyze by typing ./analyze. This script will copy all the input and output files into the Analysis directory, and run a FORTRAN program called MatGen there, which will convert the FISHES output into matrices that can be read by Matlab (make sure to compile MatGen and rename the a.out file to MatGen before running analyze the first time). The resulting files will have the extension .dat and be named according to which values are stored in them. For example, the temperatures from OutFile1 will be stored in a data file called Tempr.dat.

A3.4.3 Plot0

Once the FISHES output files have been converted to files readable by Matlab, there is a plot program in the Analysis directory called Plot0.m. This program is a Matlab program and hence must be run from Matlab; it will plot all the output from FISHES so far, determining automatically whether the output is for 1D or 2D results, and plotting the results in the appropriate format. It can be executed by typing Plot0(0) from the Matlab prompt. For one dimensional plots, one can overlay output from several different times by using Plot(1) for the first plot, executing analyze again, and using Plot(0) thereafter.

A3.4.4 surfsamp

Typing ./surfsamp from the run directory will copy the input and output files into the surfsamp directory. From this directory, running a FORTRAN program called SurfSample will create files, readable by Matlab, with the surface salinities and

temperatures from a given column of nodes together with their output times. After running this program, typing SurfSample from Matlab will produce plots of the surface vent salinities and temperatures vs. output times. A horizontal line on the salinity plot refers to equivalent normal seawater salinity (3.2 wt% NaCl).

A3.4.5 pickup

Sometimes it is necessary to take the last output from one simulation and use it as the starting input for the next simulation. The FORTRAN program pickup in the run directory will do this task automatically. It simply reads the last output from the output files and re-writes InFile0 with these values as the initial values. If the user has any questions about how to use this program or any of the others mentioned in this user file, he/she is encouraged to contact the author via email.

REFERENCES

Ackerer, P., A. Younes, and R. Mose (1999) Modeling variable density flow and solute transport in porous medium: 1. Numerical model and verification, *Transport in Porous Media*, *35*, 345-473.

Anderko, A., and K.S. Pitzer (1993), Equation-of-state representation of phase equilibria and volumetric properties of the system NaCl-H_2O above 573 K, *Geochimica et Cosmochimica Acta*, *57*, 1657-1680.

Archer, D.G. (1992), Thermodynamic properties of the NaCl + H_2O system II. thermodynamic properties of NaCl(aq), NaCl•$2H_2O$(cr), and phase equilibria, *Journal of Physical and Chemical Reference Data*, *21*, 793-820.

Bahloul, A., N.Boutana, and P. Vasseur (2003), Double-diffusive and Soret-induced convection in a shallow horizontal porous layer, *Journal of Fluid Mechanics*, *491*, 325-352.

Bahloul, A., P. Vasseur, and L. Robillard (2007), Convection of a binary fluid saturating a shallow porous cavity subjected to cross heat fluxes, *Journal of Fluid Mechanics*, *574*, 317-342.

Bai, W., W. Xu, and R.P. Lowell (2003), The dynamics of submarine geothermal heat pipes, *Geophysical Research Letters*, *30*(3), 1108, doi: 10.1029/2002GL016176.

Baross, J.A., and S.E. Hoffman (1985), Submarine hydrothermal vents and associated gradient environments as sites for the origin and evolution of life, *Origins of Life*, *15*, 327-345.

Berndt, M.E., and W.E. Seyfried Jr (1990), Boron, bromine, and other trace elements as clues to the fate of chlorine in mid-ocean ridge vent fluids, *Geochimica et Cosmochimica Acta*, *54*, 2235-2245.

Bischoff, J.L., and R.J. Rosenbauer (1984), The critical point and two-phase boundary of seawater, 200°-500°, *Earth and Planetary Science Letters*, *68*, 172-180.

Bischoff, J.L., and R.J. Rosenbauer (1988), Liquid-vapor relations in the critical region of the system NaCl-H_2O 380°C to 415°C: a refined determination of the critical point and two-phase boundary of seawater, *Geochimica et Cosmochimica Acta*, *52*, 2121-2126.

Bischoff, J.L., and K.S. Pitzer (1989), Liquid-vapor relations for the system NaCl-H2O: summary of the P-T-x surface from 300° to 500° C, *American Journal of Science*, *289*, 217-248.

Bischoff, J.L. (1991), Densities of liquids and vapors in boiling NaCl-H_2O solutions: a PVTX summary from 300° to 500° C, *American Journal of Science*, *291*, 309-338.

Brand, H., and V. Steinberg (1983), Convective instabilities in binary mixtures in a porous medium, *Physica*, *119A*, 327-338.

Brand, H., and V. Steinberg (1983), Nonlinear effects in the convective instability of a binary mixture in a porous medium near threshold, *Physics Letters*, *93A*(7), 333-336.

Butterfield, D.A., and G.J. Massoth (1994), Geochemistry of North Cleft segment vent fluids: temporal changes in chlorinity and their possible relation to recent volcanism, *Journal of Geophysical Research*, *99*, 4951-4968.

Butterfield, D.A., I.R. Jonasson, G.J. Massoth, R.A. Feely, K.K. Roe, R.E. Embley, J.F. Holden, R.E. McDuff, M.D. Lilley, and J.R. Delaney (1997), Seafloor eruptions and evolution of hydrothermal fluid chemistry, *Philosophical Transactions of the Royal Society of London*, *355*, 369-386.

Campbell, A.C., T.S. Bowers, C.I. Measures, K.K. Falkner, M. Khadem, and J.M. Edmond (1988), A time series of vent fluid compositions from 21°N, East Pacific Rise (1979, 1981, 1985), and the Guaymas Basin, Gulf of California (1982, 1985), *Journal of Geophysical Research*, *93*, 4537-4549.

Carman, P.C. (1956), *The Flow of Gases Through Porous Media*, Academic Press, New York.

Carslaw, H.S., and J.C. Jaeger (1959), *Conduction of Heat in Solids*, Oxford University Press, Oxford.

Cheng, P., and I. Pop (1984), Transient free convection about a vertical flat plate embedded in a porous medium, *International Journal of Engineering Science*, *22*, 253-264.

Cheng, P., and A.K. Verma (1981), The effect of sub-cooled liquid on film boiling about a vertical heated surface in a porous medium, *International Journal of Heat and Mass Transfer*, *24*, 1151-1160.

Cussler, E.L. (1997), *Diffusion: mass transfer in fluid systems*, 580 pp., Cambridge University Press, New York.

Delaney, J.R. (1982), Rapid intrusion of magma into wet rock: groundwater flow due to pore pressure increases, *Journal of Geophysical Research*, *87*, 7739-7756.

Delaney, J.R., V. Robigou, R.E. McDuff, and M.K. Tivey (1992), Geology of a vigorous hydrothermal system on the Endeavour segment, Juan de Fuca Ridge, *Journal of Geophysical Research*, *97*, 19633-19682.

Driesner, T., and C.A. Heinrich (2005) The system NaCl-H_2O. I. Correlation formulae for phase relations in temperature-pressure-composition space from 0 to 1000°C, 0 to 5000 bar, and 0 to 1 X_{NaCl}, *Geochimica Cosmochimica Acta*, accepted manuscript.

Driesner, T. (2005) The system NaCl-H_2O. II. Molar volume, enthalpy, and isobaric heat capacity from 0 to 1000°C, 0 to 5000 bar, and 0 to 1 X_{NaCl}, *Geochimica Cosmochimica Acta*, in revision.

Edmond, J.M., C. Measures, R.E. McDuff, L.H. Chan, R. Collier, B. Grant, L.I. Gordon, and J.B. Corliss (1979), Ridge crest hydrothermal activity and the balances of the major and minor elements in the ocean: the Galapagos data, *Earth and Planetary Science Letters*, *46*, 1-18.

Edmond, J.M., A.C. Campbell, M.R. Palmer, G.P. Klinkhammer, C.R. German, H.N. Edmonds, H. Elderfield, G. Thompson, and P.A. Rona (1995), Time series studies of vent fluids from the TAG and MARK sites (1986, 1990) Mid-Atlantic Ridge: a new solution chemistry model and a mechanism for Cu/Zn zonation in massive sulphide orebodies, in Hydrothermal Vents and Processes, *Geological Society of London Special Publication 87*, ed. Parson, L.M., C.L. Walker, and D.R. Dixon, Geological Society of London, London, pp. 77-86.

Elder, J.W. (1967), Transient convection in a porous medium, *Journal of fluid mechanics*, *27*, 609-623.

Elderfield, H., and A. Schultz (1996), Mid-ocean ridge hydrothermal fluxes and the chemical composition of the ocean, *Annual Review of Earth and Planetary Science*, *24*, 191-224.

Faust, C.R., and J.W. Mercer (1979), Geothermal reservoir simulation 1. Mathematical models for liquid- and vapor-dominated hydrothermal systems, *Water Resources Research*, *15*(1), 23-30.

Faust, C.R., and J.W. Mercer (1979), Geothermal reservoir simulation 2. Numerical solution techniques for liquid- and vapor-dominated hydrothermal systems, *Water Resources Research*, *15*(1), 31-46.

Faust, C.R. and J.W. Mercer (1979), Geothermal reservoir simulation 3. Application of liquid- and vapor-dominated hydrothermal modeling techniques to Wairakei, New Zealand, Water Resources Research, 15(3), 653-671.

Fontaine, J.F. and S.D. Wilcock (2006), Dynamics and storage of brine in mid-ocean ridge hydrothermal systems, *Journal of Geophysical Research*, *111*(B06102), doi: 10.1029/2005JB003866.

Fournier, R.O. (1987), Conceptual models of brine evolution in magmatic hydrothermal systems, *US Geological Survey Professional Papers*, *1350*, 1487-1506.

Foustoukos, D.I. and W.E. Seyfried Jr. (2007), Trace element partitioning between vapor, brine and halite under extreme phase separation conditions, *Geochimica et Cosmochimica Acta*, *71*, 2056-2071.

Foustoukos, D.I. and W.E. Seyfried Jr. (2007), Fluid phase separation processes in submarine hydrothermal systems, *Reviews in Mineralogy & Geochemistry*, *65*, 213-239.

Foustoukos, D.I. and W.E. Seyfried Jr. (2007), Quartz solubility in the two-phase and critical region of the NaCl-KCl-H_2O system: implications for submarine hydrothermal vent systems at 9°50'N East Pacific Rise, *Geochimica et Cosmochimica Acta*, *71*, 186-201.

Geiger, S., S. Roberts, S.K. Matthai, C. Zoppou, and A. Burri (2004), Combining finite element and finite volume methods for efficient multiphase flow simulations in highly heterogeneous and structurally complex geologic media, *Geofluids*, *4*, 284-289.

Geiger, S., T. Driesner, and C.A. Heinrich (2005), On the dynamics of NaCl-H2O fluid convection in the Earth's crust, *Journal of Geophysical Research*, *110*(B07101), doi: 10.1029/2004JB003362.

Geiger, S., T. Driesner, C.A. Heinrich, and S.K. Matthai (2006), Multiphase thermohaline convection in the Earth's crust: I. A new finite element-finite volume solution technique combined with a new equation of state for NaCl-H_2O, *Transport in Porous Media*, *63*, 399-434.

Geiger, S., T. Driesner, C.A. Heinrich, and S.K. Matthai (2006), Multiphase thermohaline convection in the Earth's crust: II. Benchmarking and application of a finite element-finite volume solution technique with a NaCl-H2O equation of state, *Transport in Porous Media*, *63*, 435-461.

Hayba, D.O., and S.E. Ingebritsen (1994), The computer model HYDROTHERM, a three-dimensional finite-difference model to simulate ground-water flow and heat transport in the temperature range of 0 to 1,200°C, *U.S. Geological Survey Water Resources Investigative Report*, 94-4045, 85 pp.

Hayba, D.O., and S.E. Ingebritsen (1997), Multiphase groundwater flow near cooling plutons, *Journal of Geophysical Research*, *102*(B6), 12235-12252.

Haymon, R.M., D.J. Fornari, K.L. Von Damm, M.D. Lilley, and M.R. Perfit (1993), Volcanic eruption of the mid-ocean ridge along the East Pacific Rise crest at 9°45'-52'N: direct submersible observations of seafloor phenomena associated with an eruption event in April, 1991, *Earth and Planetary Science Letters*, *119*, 85-101.

Helgeson, H. (1968), Geologic and thermodynamic characteristics of the Salton Sea geothermal system, *American Journal of Science*, *266*, 129-166.

Imai E., H. Honda, K. Hatori, A. Brack, and K. Matsuno (1999), Elongation of oligopeptides in a simulated submarine hydrothermal system, *Science*, *283*, 831-833.

Ingebritsen, S.E., and M.L. Sorey (1985), A quantitative analysis of the Lassen hydrothermal system, north-central California, *Water Resources Research*, *21*, 853-868.

Ingebritsen, S.E., and S. Rojstaczer (1996), Geyser periodicity and the response of geysers to small strains in the Earth, *Journal of Geophysical Research*, *101*, 21891-21907.

Jannasch, H.W., and C.O. Wirsen (1979), Chemosynthetic primary production at East Pacific seafloor spreading centers, *BioScience*, *29*, 592-598.

Jannasch, H.W. (1983), Microbial processes at deep-sea hydrothermal vents, *Hydrothermal processes at sea floor spreading centers*, ed. Rona, P.A., K. Bostram, L. Laubier, and K.L. Smith, p. 677-709, New York.

Kalla, L., M. Mamou, P. Vasseur, and L. Robillard (2001), Multiple solutions for double-diffusive convection in a shallow porous cavity with vertical fluxes of heat and mass, *International Journal of Heat and Mass Transfer*, *44*, 4493-4504.

Kissling, W., M. McGuinness, A. McNabb, G. Weir, S. White, and R. Young (1992), Analysis of one-dimensional horizontal two-phase flow in geothermal reservoirs, *Transport in Porous Media*, *7*, 223-253, 1992.

Kissling, W., M. McGuinness, G. Weir, S. White, and R. Young (1992), Vertical two-phase flow in porous media, *Transport in Porous Media*, *8*, 99-131.

Kissling, W. (2005), Transport of three-phase hyper-saline brines in porous media: theory and code implementation, Transport in *Porous Media*, *61*, 25-44.

Kissling, W. (2005), Transport of three-phase hyper-saline brines in porous media: examples, *Transport in Porous Media*, *60*, 141-157.

Lewis, K.C., and R.P. Lowell (2004), Mathematical modeling of phase separation of seawater near an igneous dike, *Geofluids*, *4*, 197-209.

Lilley, M.D., D.A. Butterfield, J.E. Lupton, and E.J. Olson (2003), Magmatic events can produce rapid changes in hydrothermal vent chemistry, *Nature*, *422*, 878-881.

Lombardo, S., G. Mulone, and B. Straughan (2001), Non-linear stability in the Benard problem for a double-diffusive mixture in a porous medium, *Mathematical Methods in the Applied Sciences*, *24*, 1229-1246.

Lowell, R.P., and W. Xu (2000), Sub-critical two-phase seawater convection near a dike, *Earth and Planetary Science Letters*, *174*, 385-396.

Lowell, R.P., Y. Yao, and L.N. Germanovich (2003), On the relationship between focused and diffuse flow in seafloor hydrothermal systems, *Journal of Geophysical Research*, *108*(B9), 2424, doi:10.1029/ 2002JB002371.

Lowell, R.P., and L.N. Germanovich (2004), Hydrothermal processes at mid-ocean ridges: results from scale analysis and single-pass models, from *Mid-Ocean Ridges: Hydrothermal Interactions Between the Lithosphere and Oceans*, AGU Geophysical Monograph Series 148, ed. by German, C.R., J. Lin, and L.M. Parson, pp. 219-244, American Geophysical Union, Washington, D.C.

Lowell, R.P., S. Gosnell, and Y. Yang (2007), Numerical simulations of single-pass hydrothermal convection at mid-ocean ridges: effects of the extrusive layer and temperature-dependent permeability, *Geophysics, Geochemistry, Geosystems*, *8*(10), Q10011, doi: 10.1029/2007GC001653.

Mahidjiba, A., M. Mamou, and P. Vasseur (2000), Onset of double-diffusive convection in a rectangular porous cavity subject to mixed boundary conditions, *International Journal of Heat and Mass Transfer*, *43*, 1505-1522.

McGuinness, M.J. (1990), Heat pipe stability in geothermal reservoirs, *Transactions of the Geothermal Resource Council*, *14*, 1301-1307.

McGuinness, M.J., M. Blakeley, K. Pruess, and M.J. O'Sullivan (1993), Geothermal heat pipe stability: solution selection by upstreaming and boundary conditions, *Transport in Porous Media*, *11*, 71-100.

McGuinness, M.J., S. White, R. Young, H. Ishizaki, K. Ikeuchi, and Y. Yoshida (1995), A model of the Kakkonda geothermal reservoir, Geothermics, 24, 1-48.

McGuinness, M.J. (1996), Steady-solution selection and existence in geothermal heat pipes – I. The convective case, *International Journal of Heat and Mass Transfer*, *39*, 259-274.

McGuinness, M.J. (1997), Steady-solution selection and existence in geothermal heat pipes – II. The conductive case, *International Journal of Heat and Mass Transfer*, *40*, 311-321.

Mercado, S. (1969), Chemical changes in geothermal well M-20, Cerro Prieto, Mexico, *Geological Society of America Bulletin*, *80*, 2623-2629.

Miller, S.L., and A. Lazcano (1995), The origin of life – did it occur at high temperatures?, *Journal of Molecular Evolution*, *41*, 689-692.

Nield, D.A. (1968), Onset of thermohaline convection in a porous medium, *Water Resources Research*, *4(3)*, 553-560.

Nield, D.A., and A. Bejan (2006), *Convection in porous media*, 640 pp, Springer-Verlag, New York.

Palliser, C., and R. Mckibbin (1998), A model for deep geothermal brines, I: T-p-X state-space description, *Transport in Porous Media*, *33*, 65-80.

Palliser, C., and R. Mckibbin (1998), A model for deep geothermal brines, II: thermodynamic properties – density, *Transport in Porous Media*, *33*, 129-154.

Palliser, C., and R. Mckibbin (1998), A model for deep geothermal brines, III: thermodynamic properties – enthalpy and viscosity, *Transport in Porous Media*, *33*, 155-171.

Parmentier, E.M. (1978), Two phase natural convection adjacent to a vertical heated surface in a permeable medium, *International Journal of Heat and Mass Transfer*, *22*, 849-855.

Patankar, S.V. (1980), *Numerical Heat Transfer and Fluid Flow (series in computational methods in mechanics and thermal sciences)*, Taylor & Francis Publishers.

Patil, P.R., and N. Rudraiah (1980) Linear convective stability and thermal diffusion of a horizontal quiescent layer of a two component fluid in a porous medium, International Journal of Engineering Science, 18(8), 1055-1059.

Pollack, H.N., S.J. Hurter, and J.R. Johnson (1993), Heat flow from the Earth's interior: analysis of the global data set, *Reviews in Geophysics*, *31*, 267-280.

Pruess, K. (1985), A quantitative model of vapor dominated geothermal reservoirs as heat pipes in fractured porous rocks, *Transactions of the Geothermal Resource Council*, *9*, 353-361.

Pruess, K. (1987), TOUGH user's guide. Nuclear Regulatory Commission Report, NUREG/CR-4645; also *Report LBL-20700*, Lawrence Berkeley National Laboratory, Berkeley California.

Pruess, K. (1991), TOUGH2 – a general purpose numerical simulator for multiphase fluid and heat flow, *Report LBL-29400*, Lawrence Berkeley National Laboratory, Berkeley, California.

Pruess, K. (2004), The TOUGH codes- a family of simulation tools for multiphase flow and transport processes in permeable media, *Vadose Zone Journal*, *3*, 738-746.

Pruess, K., C. Oldenburg, and G. Moridis (1999), TOUGH2 user's guide. Version 2.0. *Report LBNL-43134*, Lawrence Berkeley National Laboratory, Berkeley, California.

Pruess, K., and A. Battistelli (2002), TMVOC, a numerical simulator for three-phase non-isothermal flows of multicomponent hydrocarbon mixtures in saturated-unsaturated heterogeneous media, *Report LBNL-49375,* Lawrence Berkeley National Laboratory, Berkeley, California.

Roedder, E. (1979), Fluid inclusions as samples of ore fluids, In: *Geochemistry of Hydrothermal Ore Deposits*, 2nd edn., ed. Barnes, H.L., pp.684-737, John Wiley, New York.

Rona, P.A., and D.A. Trivett (1992), Discrete and diffuse heat transfer at ASHES vent field, Axial Volcano, Juan de Fuca Ridge, *Earth and Planetary Science Letters*, *109*, 57-71.

Schoofs, S., R.A. Trompert, U. Hansen (2000), The formation and evolution of layered structures in porous media: effects of porosity and mechanical dispersion, *Physics of the Earth and Planetary Interiors*, *118*, 205-225.

Schultz, A., J.M. Delaney, and R.E. McDuff (1992), On the partitioning of heat flux between diffuse and point source venting, *Journal of Geophysical Research*, *97*, 12229-12314.

Sclater, J.G., C. Jaupert, and D. Galson (1980), The heat flow through oceanic and continental crust and the heat loss of the Earth, *Reviews in Geophysics*, *18*, 269-311.

Seewald, J., A. Cruse, and P. Saccocia (2003), Aqueous volatiles in hydrothermal fluids from the Main Endeavour Field, northern Juan de Fuca Ridge: temporal variability following earthquake activity, *Earth and Planetary Science Letters*, *216*, 575-590.

Seyfried, W.E. Jr, M.E. Berndt, and D.R. Janecky (1986), Chloride depletions and enrichments in hydrothermal fluids: constraints from experimental basalt alteration studies, *Geochimica et Cosmochimica Acta*, *50*, 469-475.

Seyfried, W.E. Jr, J.S. Seewald, M.E. Berndt, K. Ding K, and D.I. Foustoukos (2003), Chemistry of hydrothermal vent fluids from the Main Endeavour Field, northern Juan de Fuca Ridge: geochemical controls in the aftermath of June 1999 seismic events, *Journal of Geophysical Research*, *108*(B9), 2429, doi: 10.1029/2002JB001957.

Sezai, I. and A.A. Mohamad (1999), Three-dimensional double-diffusive convection in a porous cubic enclosure due to opposing gradients of temperature and concentration, *Journal of Fluid Mechanics*, *400*, 333-353.

Shank, T.M., D.J. Fornari, K.L. Von Damm, M.D. Lilly, R.M. Haymon, and R.A. Lutz (1998), Temporal and special patterns of biological community development at nascent deep-sea hydrothermal vents along the East Pacific Rise, *Deep Sea Research II*, *45*, 465-515.

Simpson, M.J., and T.P. Clement (2003), Theoretical analysis of the worthiness of Henry and Elder problems as benchmarks of density-dependent groundwater flow models, *Advances in Water Resources*, *26*, 17-31.

Sinha, M.C., and R.L. Evans (2004), Geophysical constraints upon the thermal regime of the ocean crust, from Mid-ocean ridges: hydrothermal interactions between the lithosphere and oceans, *AGU Geophysical Monograph Series 148*, 19-62.

Stein, C.A., and S. Stein (1994), Constraints on hydrothermal heat flux through the oceanic lithosphere from global heat flow, *Journal of Geophysical Research*, *99*, 3081-3095.

Straus, J., and G. Schubert (1981), One-dimensional model of vapor-dominated geothermal systems, *Journal of Geophysical Research*, *86*, 9433-9438.

Tanger, J.C., and K.S. Pitzer (1989), Thermodynamics of NaCl-H_2O: a new equation of state for the near-critical region and comparisons with other equations for adjoining regions, *Geochimica et Cosmochimica Acta*, *53*, 973-987.

Thompson, G. (1983), Basalt-seawater interaction in hydrothermal processes at seafloor spreading centers, ed. Rona, P.A., K. Bostrom, L. Laubier, and K.L. Smith, 225-278, *NATO Conf. Ser. IV*, *Mar. Sci.*, *12*.

Tivey, M.A., and H.P. Johnson (2002), Crustal magnetization reveals subsurface structure of Juan de Fuca Ridge hydrothermal vent fields, *Geology*, *30*, 979-982.

Van Ark, E.M., R.S. Detrick, J.P. Canales, S.M. Carbotte, A.J. Harding, G.M. Kent, M.R. Nedimovic, W.S.D. Wilcock, J.B. Diebold, and J.M. Babcock (2007), Seismic structure of the Endeavour Segment, Juan de Fuca Ridge: correlations with seismicity and hydrothermal activity, *Journal of Geophysical Research*, *112*(B02401), doi: 10.1029/2005JB004210.

Van Dover, C.L. (2000), *The ecology of deep-sea hydrothermal vents*, Princeton University Press, 424pp.

Von Damm, K.L., S.E. Oosting, R. Kozlowski, L.G. Buttermore, D.C. Colodner, H.N. Edmonds, J.M. Edmond, and J.M. Grebmeier (1995), Evolution of the East Pacific Rise hydrothermal vent fluids following a volcanic eruption, *Nature*, *375*, 47-50.

Von Damm, K.L., L.G. Buttermore, S.E. Oosting, A.M. Bray, D.J. Fornari, M.D. Lilley, and W.C. Shanks Jr (1997), Direct observation of the evolution of a seafloor 'black smoker' from vapor to brine, *Earth and Planetary Science Letters*, *149*, 101-111.

Von Damm, K.L., C.M. Parker, R.M. Gallant, and J.P. Loveless (2002), Chemical evolution of hydrothermal fluids from EPR 21°N: 23 years later in a phase separating world, *EOS Trans. AGU*, *83*(47), Fall Meet. Suppl., Abstract V61B-1365.

Von Damm, K.L. (1995), Controls on the chemistry and temporal variability of seafloor hydrothermal fluids, from Seafloor Hydrothermal Systems, from *Seafloor Hydrothermal Systems: Physical, Chemical, Biological, and Geological Interactions*, AGU Geophysical Monograph Series 91, ed. by Humphris, S.E., R.A. Zierenberg, L.S. Mullineaux, and R.E. Thompson, pp. 222-247, American Geophysical Union, Washington, D.C.

Von Damm, K.L. (2004), Evolution of the hydrothermal system at east pacific rise 9°50'N: geochemical evidence for changes in the upper oceanic crust, from *Mid-Ocean Ridges: Hydrothermal Interactions Between the Lithosphere and Oceans*, AGU Geophysical Monograph Series 148, ed. by German, C.R., J. Lin, and L.M. Parson, pp. 285-304, American Geophysical Union, Washington, D.C.

Von Damm, K.L., and M.D. Lilley (2004), Diffuse flow hydrothermal fluids from 950'N East Pacific Rise: origin, evolution and biogeochemical controls, in The Subsurface Biosphere at Mid-Ocean Ridges, ed. Wilcock, W.S.D., E.F. DeLong, D.S. Kelley, J.A. Baross, and S.C. Cary, *AGU Geophysical Monograph Series 144*.

Williams, D.L., and R.P. Von Herzen (1974), Heat loss from the Earth: new estimate, *Geology*, *2*, 327.

Wolery, T.J., and N.H. Sleep (1976), Hydrothermal circulation and geochemical flux at mid-ocean ridges, *Journal of Geology*, *84*, 249-275.

Xu, T., and K. Pruess (2001), Modeling multiphase non-isothermal and reactive geochemical transport in variably saturated fractured rocks: 1. Methodology, *American Journal of Science*, *301*, 16-33.

Xu, W. (1996), Towards numerical modeling of two-phase flow in seafloor hydrothermal systems, Ph.D. thesis, Georgia Institute of Technology, Atlanta, GA.

Xu, W., and R.P. Lowell (1998), Oscillatory instability of one-dimensional two-phase hydrothermal flow in heterogeneous porous media, *Journal of Geophysical Research*, *103*, 20859-20868.

Xu, W., and R.P. Lowell (1998), An alternative model of the Lassen hydrothermal system, Lassen volcanic national park, California, Journal of Geophysical Research, 103, 20869-20882.

Young, R. (1996), Phase transitions in one-dimensional steady state hydrothermal flows, *Journal of Geophysical Research*, *101*, 18011-18022.